Electron Interferometry and Magnon Transport in Graphene Quantum Hall Systems

Citation

Wei, Di S. 2019. Electron Interferometry and Magnon Transport in Graphene Quantum Hall Systems. Doctoral dissertation, Harvard University, Graduate School of Arts & Sciences.

Electron Interferometry and Magnon Transport in Graphene Quantum Hall Systems

A dissertation presented
by

Di Sonia Wei

to
The School of Engineering and Applied Sciences
in partial fulfillment of the requirements
for the degree of
Doctor of Philosophy
in the subject of

Applied Physics

Harvard University
Cambridge, Massachusetts
April 2019

Dissertation advisor | Author

Professor Amir Yacoby | **Di Sonia Wei**

Electron Interferometry and Magnon Transport in Graphene Quantum Hall Systems

Abstract

The discovery of graphene, an atomically thin layer of carbon, has given the condensed matter community an opportunity to investigate two dimensional (2D) physics with a fresh set of experimental knobs. The quantum Hall (QH) effect is a particularly rich system in which recent experiments in graphene have already revealed novel magnetic ground states, superlattice-induced QH effects, and new fractional QH phases. Experimentalists and theorists alike have been able to re-examine open problems in the field, as well as discover new challenges and physical phenomena. One of the key features of the QHE is the behavior of the electrons at the boundaries of the sample, where one-dimensional edge states exist. This thesis will describe novel manipulations of these edge states, using them to probe the electronic and magnetic properties of graphene quantum Hall states.

The first experiment described here will show how we can use QH edge states as solid-state analogues of monochromatic beams of light to study electron interference. Electron interferometry is regarded as one of the most promising routes for studying fractional and non-Abelian statistics and quantum entanglement via two-particle interference. However, creating an edge-channel interferometer in which electron-electron interactions play an important role requires a clean system and long phase coherence lengths. We have achieved this with a simpler Mach-Zehnder design than used in previous 2D systems and are able to realize visibilities of up to 98% using spin and valley polarized edge channels. Surprisingly, our interferometer is robust to dephasing effects at energies an order of magnitude larger than observed in pioneering experiments in semiconductor quantum wells. Our results shed light on the nature of edge-channel equilibration and open up new possibilities for studying exotic electron statistics and quantum phenomena.

The second experiment will describe how we use out-of-equilibrium occupation of QH edge channels in graphene to excite and detect spin waves (magnons) in magnetically ordered QH states. Magnons are the elementary spin excitations of magnetic materials and are essential to understanding the intrinsic ordering and thermodynamic properties of magnetic systems. They are able to transmit information without displacing charge, and as such, they are free from the heat production associated with electrical currents, making them promising candidate signal carriers for future information processing. When realized in graphene, spin waves are expected to be particularly long lived due to the weak spin-orbit interaction. However, their charge-neutral nature has made them challenging to detect and study. Our novel method of magnon generation and detection has allowed us to show long distance spin wave propagation through different ferromagnetic phases in the N=0 Landau level, as well as across the insulating canted antiferromagnetic phase. Our results providing insight into the order parameters of magnetic phases in the QH regime and enable experimental investigation of the fundamental magnetic properties of two-dimensional electron systems.

Contents

List of Figures

Citations to Previously Published Work

Some of the figures and a portion of the text have appeared in the following papers:

Di S. Wei, T. van der Sar, S.H. Lee, K. Watanabe, T. Taniguchi, B. I. Halperin, and A. Yacoby, "Electrical generation and detection of spin waves in a quantum Hall ferromagnet", *Science* **362**, 229-233 (2018).

Di S. Wei, T. van der Sar, Javier D. Sanchez-Yamagishi, K. Watanabe, T. Taniguchi, Pablo Jarillo-Herrero, B. I. Halperin, and A. Yacoby, "Mach-Zehnder interferometry using spin- and valley-polarized quantum Hall edge states in graphene", *Science Advances* **3**, e1700600 (2017).

Acknowledgments

I have had a number of lucky breaks in graduate school, mostly involving meeting and collaborating with the many people listed below without whom this work would not have been possible.

First and foremost, I thank my advisor, Amir Yacoby, whose great gusto for tackling challenging physics and experimental problems has been an inspiration to me throughout my years in his group. His creativity inspired the projects I worked on; his eternal optimism pushed me to keep going when the road became difficult; and his deep scientific intuition helped me to make sense of oftentimes confusing discoveries. He was also a wonderfully supportive mentor who welcomed us into his home for group potlucks and retreats, and tried to introduce us to the supposed joys of winter hiking. His happy, engaging demeanor created an equally happy and engaging lab that I am extremely grateful to have been a part of.

I thank Bert Halperin who provided an immense amount of theoretical insight to all of the projects described in this thesis. I thank him for a number of discussions where his incisive questioning and insightful suggestions greatly improved our experimental work.

I am also very grateful to Philip Kim who was very generous with both his time and ideas throughout my Ph.D. He is both an extremely knowledgeable and generous person, and I especially appreciate that he is such an easy person to talk with.

I was fortunate to have met some incredible people in the Yacoby lab. Ben Feldman and Angela Kou co-mentored me in the early days of my Ph.D., and I could not have asked for more brilliant and dedicated mentors. Ben was a patient and thorough teacher, and was the first person to make me feel welcome in the lab. Angela pushed me to be the best scientist I could be with careful derivations and a very effective use of the Socratic method. I am indebted to Mikey Shulman who frequently checked to make sure that I was not concussed and always made our office a fun, booby-trapped place to be. Marc Warner forced me to not be such a pathetic nerd and try new hobbies like smoking cigars and lighting tables on fire, but he was still a true friend to me even when my inner pathetic nerd emerged. Toeno van der Sar was a terrific postdoc to work with and played a pivotal role in all of the experiments listed in this thesis. I thank him for his exuberance and constant encouragement during all of our experimental ups and downs. Francesco Casola was both brilliant and good-natured–even when we both thought (for about 10 minutes) that I had flushed his diamond down the sink. John Nichol's sense of humor helped me get through a period of what seemed like interminable fridge problems, and his kindness made our office a warm and happy place to be. Pat Gumann's intense passion for experimental physics is an inspiring spectacle to witness, and I will always be grateful that he drove all the way from Yorktown to help me re-wire the new SPM attocubes. Andrei Levin generously taught me how to use the SPM in my last year of grad school, and made the experience all the more enjoyable with a continuous barrage of SPM jokes.

In this last year I have had the pleasure of working closely with Seung Hwan Lee, who has who has proven to be an amazing problem solver and a deeply insightful scientist who asks great questions. I also had the good fortune of working on the SPM with Andrew Pierce who is the best type of scientist to work with – relentlessly talented, hard-working, and completely off his rocker. I'd also like to thank many current and past members of the lab who made my time here so enjoyable, including:

Lucas Thiel, Fokko de Vries, Matthias Künne, Susanne Muller, Chunhui Du, Hechen Ren, Yinyu Liu, Trevor Rhone, Assaf Hamo, Loren Alegria, Uri Vool, Qi Yang, Tony Zhou, Shannon Harvey, Michael Kosowsky, Lucas Orona, Charlotte Bøttcher, Ziwei Qiu, Ruolan Xue, Andrew Saydjari, Joris Carmiggelt, and Lisa Gachter.

It was also a great pleasure to learn from and collaborate with various members of the Kim lab at Harvard, whose members generously gave me access to their equipment and expertise. I want to thank in particular Gil-ho Lee, Xiaomeng Liu, Ke Wang, Austin Cheng, Luis Jauregui, Andy Joe, Frank Zhao, Young Jae Shin, Hyobin Yoo, Jonah Waissman, Jing Shi, Laurel Anderson, Nicola Poccia, Yuval Ronen, Onder Gul, Katie Huang, Rebecca Engelke, Thomas Werkmeister, and Zeyu Hao.

Additionally, I had many helpful discussions with Shiang Fang from the Kaxiras lab, Shanying Cui from the Hu lab, and Bo Dwyer and Trond Anderson in the Lukin lab. I also benefited from the tremendous skills of Hannah Belcher in all administrative issues, Jim MacArthur in all things electronic, and Stan Cotreau in all machining matters. The CNS staff made my fabrication projects possible, and in particular I thank Ed Macomber, Jason Tresback, Yuan Lu, and Steve Paolini. I thank the talented Concannon brothers for helping us build all the odds-and-ends in our various setups, and for being lovely people to chat with. I thank Giorgio Frossati for giving me so much advice over the phone and helping me make our little fridge the best that it could be.

I am also grateful to all the people at MIT where I spent a large chunk of time in my first two years in graduate school. I thank Pablo Jarillo-Herrero and Ray Ashoori who graciously allowed me to work in their labs and learn from their students. I thank Javier Sanchez-Yamagishi who became an invaluable scientific mentor to me as well as a terrific friend and charades partner. I thank Valla Fatemi whose intellectual curiosity and buoyant spirit has helped me to become a better person and scientist. I thank Joel Wang who is an amazing chef and one of the smartest, most kind-hearted people I know. I also thank Andrea Young, Ben Hunt, Yafang Yang, Jason Luo, and Dani Rodan-Legrain for making MIT feel like a second (lab) home.

Outside of the physics community, I became friends with the most loyal, hilarious, and wonderful group of people that I have ever had the chance to meet. Thank you to Bobby, Ari, Jenny, Eddie, and Toby for helping me put away prodigious numbers of dumplings and for making Cambridge feel like (real) home.

I would also like to thank my parents who went through unimaginable hardship and sacrifice to give me such a privileged and happy life. My dad spent the limited free time he had when I was a kid to teach my sister and me math and has always been our greatest champion. I thank my mom for her endless support and for sparking in me a love of learning. I also thank my sister Peng who has been my greatest confidante, my fiercest protector, my most dependable co-conspirator, and my best friend for the majority of my life. Thank you also to my big bro Ramy who spent a solid chunk of time reading one of my papers so that he could tell interferometry-related one-liners.

I must of course also thank my good dogs Beans and Izzy. Who really rescued who? It was definitely ME who rescued YOU, you little turds. Thank you for doing your best to help me write me thesis even though you are not very good proofreaders and don't know any physics.

Finally, I thank Spencer Tomarken whose contributions to my life have been so wide-ranging and countless that I can only attempt to scratch the surface of my appreciation here. He is a brilliant partner who would spend hours learning random things outside his own field just so I could have someone to discuss a paper with. He is my favorite person to learn things from, and has always helped and supported me no matter how busy or stressful his own work was. We have wandered near and far together, from Fresh Pond to Milwaukee to Madagascar – and when we are apart his voice still pipes up in my brain, encouraging me to be kinder and braver. There is no one who makes me laugh harder, or cares for me more, despite knowing the inner depths of my truly deranged soul. The luckiest break in my life so far has been to find this wonderful person.

Chapter 1

Introduction

A simple yet illuminating way to investigate a material is to apply a voltage across it and measure the current passing through. This probes how difficult it is for electrons to navigate their way across, telling us if the material is insulating, conducting, or somewhere in between. The more interesting the material is, the more games one can play with the electrons inside. In two-dimensional materials it turns out that there are an extraordinary number of games to play. For example, one can use a metal gate nearby to pack in a huge density of electrons, numbered in the hundreds of billions. Or, a magnetic field can be used to push electrons from one side to the other, resulting in a voltage perpendicular to the flow of current. This latter example was used to show that electrons were physically moving in an electric current back in 1879 [1]. The goals of games like these are to try and extract new and interesting information.

The quantum Hall effect, discovered in 1980 by Klaus von Klitzing et al. [2] is an example of how dramatically the flow of electrons can change in a material. At low, liquid helium temperatures, von Klitzing found that the Hall resistance of a 2D electron system evolved into well-defined plateaus upon application of large magnetic fields. This strange current flow was eventually found to be the result of pushing the mobile electrons away from the middle of the device to create an insulator everywhere except extremely conducting strips at the edges, with a conductance quantized to a few parts per billion in integer units of e^2/h. This discovery created an entirely new subfield of condensed matter physics devoted to studying this unique phenomenon that was named the quantum Hall effect (QHE). The explosive amount of research into the QHE was made possible by the concurrent rapid developments made in the careful growth of semiconductor/insulator interfaces hosting 2-dimensional electron gases (2DEGs). Cleaner devices made by extremely precise molecular beam epitaxy growth allowed for the discovery of a myriad of new phenomena in the field, including those caused by correlated electron physics such as ferromagnetism [3], and the fractional quantum Hall effect [4].

A little over two decades later in 2004, Andre Geim and Kostya Novoselov made the Nobel prize winning discovery that they could also obtain 2D electron systems by not-that-precise peeling off layers of graphite using Scotch tape [5]. By sticking their peeled-off graphite onto a silicon dioxide substrate (SiO_2) and then hunting around for the thinnest pieces under an optical microscope, they found single, atomically thin layers of graphite called graphene. Straight away experimentalists showed that many of the same phenomena present in 2DEGs existed in graphene as well, including the quantum Hall effect [6, 7]. Of course, an important question that many people asked about this naturally occuring 2D system was: what kind of new physics will this new material reveal? Luckily enough for a new generation of researchers not fortunate enough to participate in the height of the first quantum Hall boom, there have been a number twists in graphene physics that have allowed us to explore new and interesting avenues.

1.1 Organization of this thesis

In this thesis I will explain two main experiments that were both performed in a graphene quantum Hall system. The first is a study of electrons that behave like photons and are used to demonstrate a special type of interferometry. The second study is about using electrons to give us information about magnetic excitations in magnetic quantum Hall system.

In Chapter 2 I will introduce the quantum Hall effect in semiconductor systems, where it was initially discovered. I begin the chapter with the classical Hall effect and then progress to a description of Landau levels and edge states in a 2D system. Then, I will describe the manifestation of the quantum Hall effect in graphene, beginning with the importance of its crystal structure and electronic bands, and ending with Landau quantization in graphene. I will then describe how electron-electron interactions create magnetic ground states known as quantum Hall ferromagnets. Finally, I will introduce edge state equilibration, a type of transport measurement that is essential to understanding the experiments presented here.

Chapter 3 describes electron interferometry experiments conducted with quantum Hall edge channels. I begin with a brief introduction to interferometry in general, and then provide a background of previous electron interferometry experiments performed in both GaAs systems and graphene. Then, I will describe the experimental details of creating a Mach-Zehnder interferometer along a PN junction in a graphene device.

Chapter 4 describes the second experiment in which we use the scattering between oppositely spin-polarized edges to generate spin waves (magnons). I will begin with a general introduction to magnons and then progress to describing work done previously to characterize quantum Hall ferromagnets. I will then describe experiments demonstrating that by gating different parts of the graphene into different filling factors we can engineer a system where two oppositely spin-polarized edges scatter into each other next to an insulating magnetic bulk – thereby generating magnons in the system.

Chapter 2

Background: Quantum Hall effect

2.1 The quantum Hall effect in two-dimensional electron systems

2.1.1 Landau quantization

Quantum mechanics indicates that electrons confined to move in a 2D system will behave differently than those that are able to move in all three dimensions. However, it was difficult to test this out on atomically thin 2D crystals, because initially they proved quite difficult to isolate. It was even thought that a single layer, one-atom thick, might be too thermodynamically unstable to even exist [8]. This motivated experimental physicists to create artificial 2D systems where electrons were quantum mechanically confined to travel throughout a plane at the interface of either a semiconductor and an insulator, or two semiconducting materials [9].

The quantum Hall effect was one of the most striking and important discoveries of new physics in 2D materials. When placed in a magnetic field, at low temperatures, a 2D electron system (2DES) exhibits a very strange alteration of the Hall voltage. The Hall voltage V_{xy} is a measurement of the transverse voltage in a rectangular Hall bar, when current (I) is flowing in the longitudinal direction, as shown in Fig. 2.1 A.

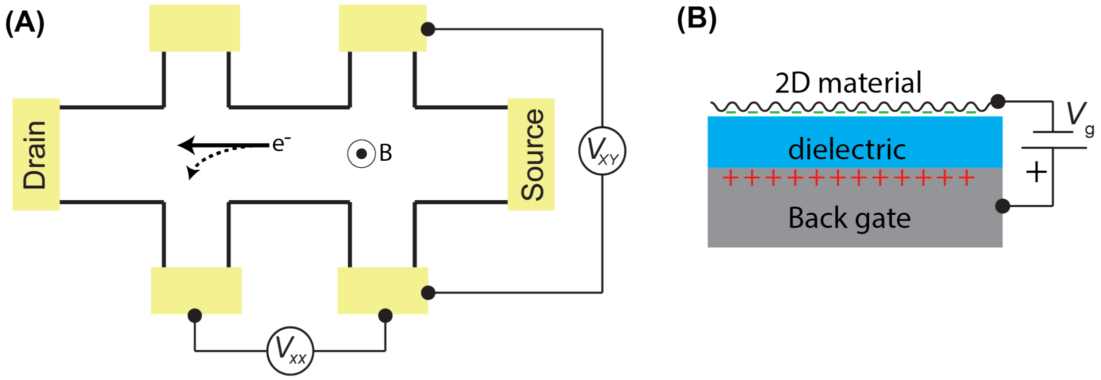

Figure 2.1: **Schematic of a Hall bar where a voltage bias is applied at the right most lead and current is measured on the left most lead.** **(A)** The magnetic field B is applied perpendicularly to the flow of current. V_{xx} is measured along the current flow direction and V_{xy} is measured in the transverse direction. **(B)** The carrier density of a 2D material can be tuned with a nearby metal gate using the electric field effect.

When a magnetic field is applied perpendicularly to the plane of the Hall bar, the electrons are pushed to the side of the Hall bar via a classical effect called the Lorentz force. This builds up electrons on one side of the device, resulting in a transverse voltage [1], or Hall voltage (V_{xy}) equal to:

$$V_{xy} = \frac{B}{ne} I \tag{2.1}$$

where n is the electron density, e is the charge of an electron, and I is the current flowing through the device. We can see that V_{xy} can be tuned with either the magnetic field or the electron density (and thereby the Fermi Energy). The carrier density can be changed with a nearby metal gate, separated from the 2DES by an insulating dielectric (Fig. 2.1B). A positive voltage on the gate generates an electric field between the metal and the 2DES, causing electrons to get pulled into the 2DES from the reservoirs in the contacts. We treat the system like a parallel plate capacitor and calculate the carrier density as a function of the gate voltage to be:

$$n = \frac{\epsilon_0 \epsilon}{ed} V_g \tag{2.2}$$

where ϵ_0 is the permittivity of free space, ϵ is the permittivity of the dielectric, d is the distance of the gate to the 2DES, and V_g is the gate voltage. The ability to easily tune the carrier density using only a nearby metallic gate is another special property of 2DES, since the electric field is screened in bulk conductors.

In 1980 von Klitzing found that at low, liquid helium temperatures (1.5 K) and at a high magnetic field (18 T), this classical dependence gave way to plateaus in V_{xy} as a function of the electron density (See Fig. 2.2) [2]. The precise quantization of the resistance of these plateaus at multiples of h/e^2, along with corresponding drops in V_{xx} to 0, are the experimental signatures of the quantum Hall effect. Remarkably, this effect is independent of the device geometry or host material, as long as it is a 2D electron system. Below, we derive this result by solving the Schrodinger equation for a 2D system in a magnetic field.

Consider a 2D system confined to the X-Y plane with non-interacting electrons

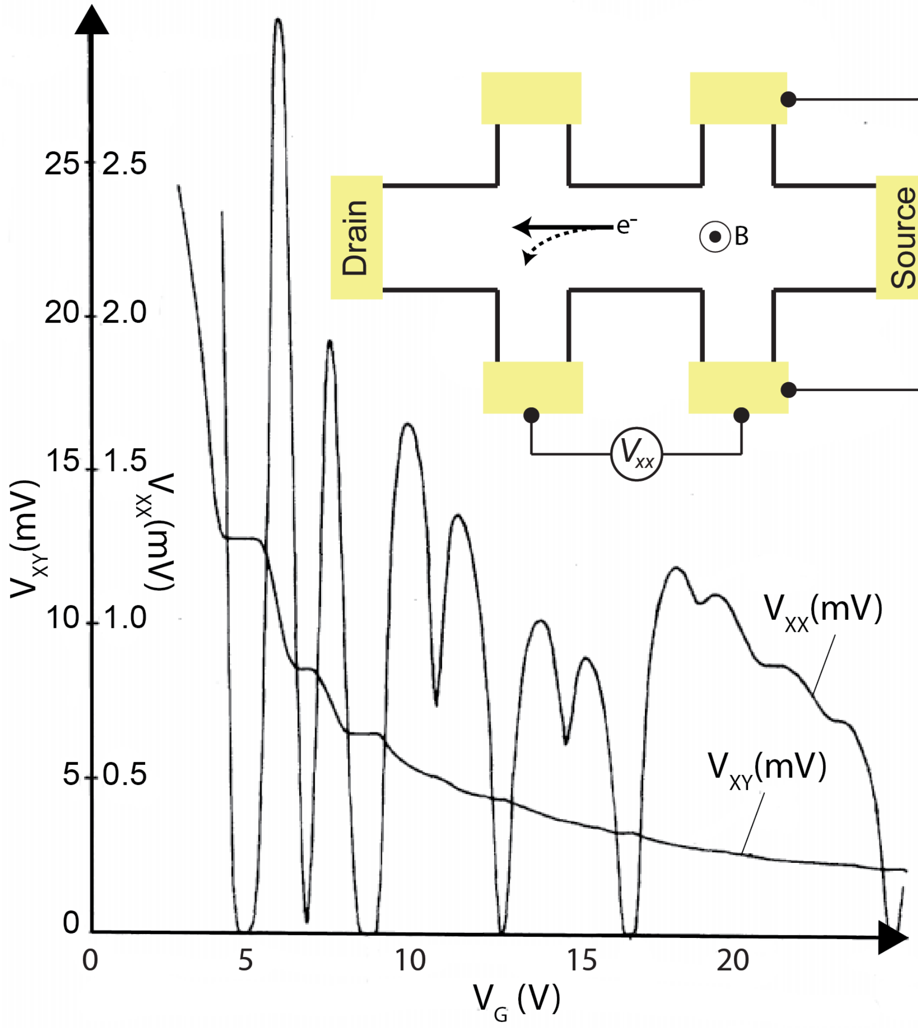

Figure 2.2: **Hall and longitudinal voltage as a function of gate voltage taken at 1.5K in 18T, adapted from [2].** The source drain current is 1 uA. The inset is a representation of a Hall bar used for this measurement. We see plateaus in V_{xy} and corresponding sharp drops in V_{xx} as the gate voltage is changed, which changes the carrier density in the system

of charge e. We apply a magnetic field in the Z-direction: $\vec{B} = (0, 0, B)$. To account for this magnetic field, we add a vector potential $\vec{A}$ to the (lattice) momentum ($\vec{p}$), giving us the Hamiltonian of this system:

$$\hat{H} = \frac{1}{2m}\big(\vec{p} - e\vec{A}\big)^2 \tag{2.3}$$

where m is the band mass instead of the free electron mass. We have the freedom to choose any $\vec{A}$ such that $\vec{B} = \nabla$ x $\vec{A}$, and so we use the convenient Landau gauge $\vec{A} = (0, Bx, 0)$. Rewritten, our Hamiltonian becomes:

$$\hat{H} = \frac{\hat{p}_x^2}{2m} + \frac{1}{2m}\big(\hat{p}_y - eB\hat{x}\big)^2 \tag{2.4}$$

.

Since $\hat{p}_y$ commutes with the Hamiltonian, we replace it with its eigenvalue $\hbar k_y$:

$$\hat{H} = \frac{\hat{p}_x^2}{2m} + \frac{1}{2}m\omega_c^2\big(\hat{x} - \frac{\hbar k_y}{m\omega_c}\big)^2 \tag{2.5}$$

where ω_c is the cyclotron frequency:

$$\omega_c = \frac{\hbar}{ml_B^2} = \frac{eB}{m} \tag{2.6}$$

.

We see that this is exactly the Hamiltonian for the quantum harmonic oscillator with a minimum of potential shifted in coordinate space by $x_0 = \frac{\hbar k_y}{m\omega_c}$, or $k_y l_B^2$ where $l_B = \sqrt{\frac{\hbar}{eB}}$ is the magnetic length. Consequently, the system has the following energy levels:

$$E_n = \hbar\omega_c\left(n + \frac{1}{2}\right). \tag{2.7}$$

This gives us quantized energy levels that have energy spacing of $\hbar\omega_c$. The wavefunctions of the system are a product of the momentum eigenstates in the y-direction and harmonic oscillator states $|\phi_n>$ shifted by x_0 in the x direction:

$$\psi_{(x,y)} = e^{ik_y y}\phi_n(x - x_0) \tag{2.8}$$

.

Fig. 2.3A shows the density of states of the 2D system when the magnetic field is at $B = 0$. The application of magnetic field causes all the states in an energy range $\hbar\omega_c$ to be amassed into a single Landau level, a delta function in energy (Fig. 2.3B). In a real 2DEG, there is disorder in the system which broadens out each of these delta functions over a range of energy.

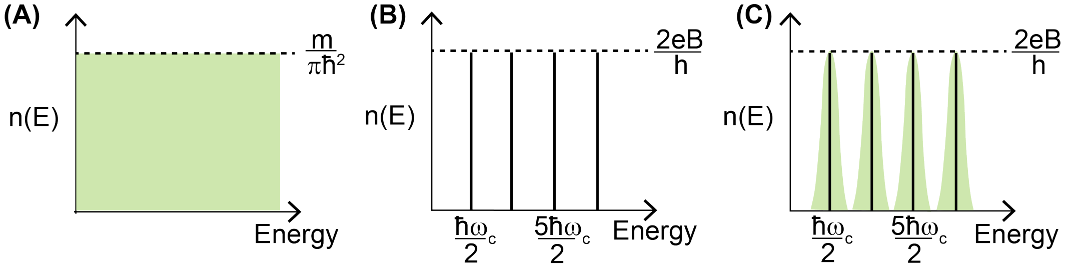

Figure 2.3: **The density of states in a 2DES before and after magnetic field is applied (A)** A 2DES with zero applied field **(B)** a 2DES after applying a sufficiently large magnetic field, causing Landau quantization **(C)** a 2DES after applying a sufficiently large magnetic field and adding in effects of disorder.

We would like to know how many states are in each LL. Assuming periodic boundary conditions gives the constraint $k_y = (2\pi/L_y)j$ where j is an integer. The integer j is further restricted by that fact that x_0 must lie within the system giving us $(0 \leq x_0 < L_x)$. We find a bound for j:

$$0 \leq N < \frac{L_x L_y}{2\pi l_B^2} \tag{2.9}$$

Thus in our sample, the number of wavefunctions (or electrons) per Landau level is given by: $\frac{L_x L_y}{2\pi l_B^2}$. We define a quantity called the filling factor, denoted by ν, which indicates how many LLs have been completely filled:

$$\nu = \frac{\text{Total number of electrons}}{\text{electrons per LL}} = \frac{N_e \cdot 2\pi l_B^2}{L_x L_y} \tag{2.10}$$

where N_e is the number of electrons and is equal to the density of electrons multiplied by the area $(n_e \cdot A)$. We find:

$$\nu = 2\pi l_B^2 n_e = \frac{h n_e}{eB} \tag{2.11}$$

We also see that the density of states per filled Landau level is $n_e = eB/h$. A quantum of magnetic flux is defined as $\Phi_0 = h/e$, and the number of states per unit area is B/Φ_0. Therefore we can say that there is one state (or 2 if we account for the spin degree of freedom) per flux quantum in each Landau level. Additionally, each state occupies an area of $h/eB = 2\pi l_B^2$.

2.1.2 Edge states

A real 2D sample is finite in its dimensions, and requires a confining potential at the boundary, altering the properties of electrons at the edge compared to the bulk. Usually, the edges of the sample are ignored because they are such a small contribution to the overall conductance of a sample. However, in the case of the quantum Hall effect, the edge states play a very large role in how the current flows across the 2DES [10]. For a typical wide conductor, the confinement potential $V(x)$ looks similar to what is pictured in Fig. 2.4A. The dispersion relation for the energy can be found using perturbation theory and assuming that the potential $V(x)$ changes slowly enough that it can be approximated as a constant over each state. We then only need to add a position-dependent term to the energies given by equation 2.7. The new energies are then:

$$E_n = \hbar\omega_c\left(n + \frac{1}{2}\right) + V\left(\frac{\hbar k_y}{eB}\right). \tag{2.12}$$

When a single Landau level has been filled, the Fermi energy lies in between the first and second energy level. Because there is a direct mapping from the y-momentum $\hbar k$ to the x-direction, we can represent the dispersion relation for the energy as depicted in Fig. 2.4B. To figure out what kind of conductance we expect from the system, we apply a voltage difference (V) across the device, which changes the chemical potential difference $\Delta\mu = eV$ on the two sides of the sample, as shown in Fig. 2.4C. Then we can integrate the drift velocity over all the filled states:

$$I_y = -e\int_{-\infty}^{\infty} \frac{dk}{2\pi} v_y(k). \tag{2.13}$$

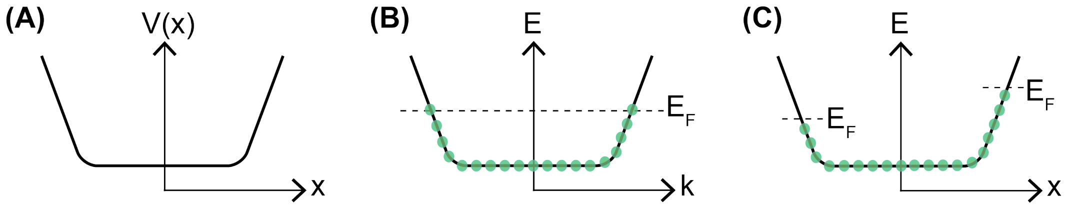

Figure 2.4: **Effects of a confining potential on a 2DES in a magnetic field. (A)** The confinement potential $V(x)$ of a typical wide conductor. **(B)** The energy dispersion of the states of the 2DES in a magnetic field with a confining potential. **(C)** Applying a chemical potential difference to the system causes an imbalance to the energy levels on either side of the device.

The drift velocity in the y-direction is caused by the force of the magnetic field and the electrostatic potential and given by [11]:

$$v_y = -\frac{1}{eB}\frac{\delta V}{\delta x}. \tag{2.14}$$

Also, since each state with y-momentum $\hbar k$ is at position x, this is approximately equal to integrating over x, so we get the equation:

$$I_y = \frac{e}{2\pi l_B^2}\int_0^x dx \frac{1}{eB}\frac{\delta V}{\delta x}. \tag{2.15}$$

Since the change in potential from one side of the device to the other is just $\Delta\mu$:

$$I_y = \frac{e}{2\pi\hbar}\Delta\mu. \tag{2.16}$$

We therefore expect a conductance $I_y/V = e^2/h$ for each Landau level. This is the conductance expected for a 1D mode with perfect transmission, indicating that electrons injected into the QH regime cannot be backscattered. This makes sense because we see that $\frac{\delta V}{\delta x}$ changes sign on opposite ends of the sample, indicating that the edge states on either side of the device carry currents in opposite directions – we call these chiral edge states. When the Fermi level is between Landau levels, an electron scattering site must scatter an electron from one side all the way to the opposite side in order to affect the conductance, a low-probability event in a typical micron sized device.

In a simple two-terminal measurement, as depicted in Fig. 2.5A, we see that the suppression of backscattering means that the edge state originating from the left lead will be completely coupled to the chemical potential of that lead [13]. Similarly, the edge state originating from the right lead will be completely coupled to the right lead. When the edge states reach the opposite lead from which they originate there will be a "hot spot" where all the voltage drops. This was actually seen in an experiment done in 1991, where a quantum Hall sample was put in liquid helium and the heating at the hot spots caused a local vaporization of the helium – imaged in Fig. 2.5B [12].

This difference in chemical potential between the two sides of the device are what is measured by the transverse voltage V_{xy} (Fig. 2.5C), where we will find the same conductance as measured in the two terminal configuration: $\sigma_{xy} = e^2/h$. This is because one of the voltage probes is coupled to one edge state, and the other is coupled to the one on the opposite edge. If we are to measure the longitudinal voltage (V_{xx}) across the same side of the device, we find that that $V_{xx} = 0$. This is because both voltage probes are coupled to the same edge state, which remains at

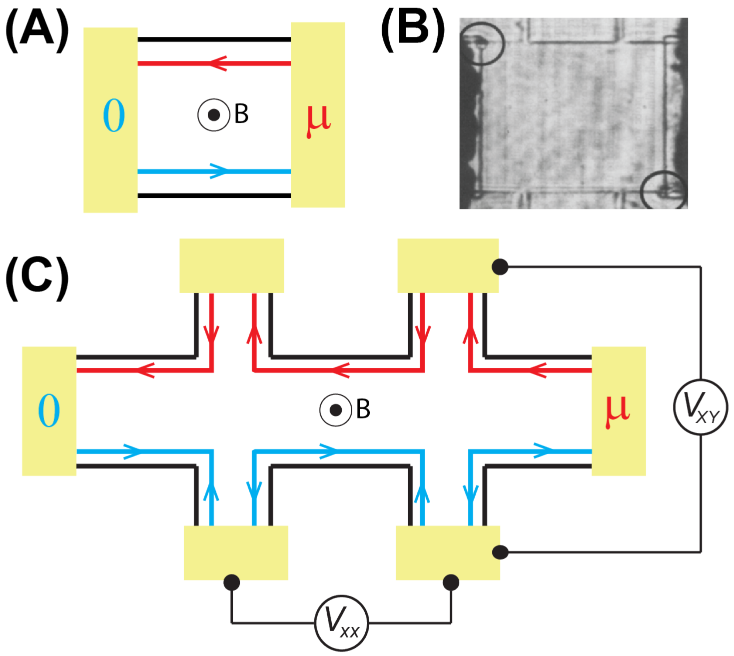

Figure 2.5: **Transport schematics in the quantum Hall regime.** **(A)** A two-terminal measurement in which an applied voltage causes an imbalance in chemical potential between the two sides. **(B)** A 2DES (GaAs/AlGaAs heterostructure) with metal contacts on both sides, where 80 μA is applied across the device. Two helium drops are visible in the upper right and lower left (circled in the image) and show where heat is being dissipated in the sample. Adapted from [12]. **(C)** A six-terminal measurement where a voltage is applied between the right-most and left-most leads, and V_{xy} and V_{xx} are measured across the sample and along the sample, respectively.

the same chemical potential along the entire length of the device.

2.2 The quantum Hall effect in graphene

2.2.1 Band structure of graphene

Now that we have a basic understanding of the quantum Hall effect, as well as an expectation for what we should see experimentally, we can discuss its manifestation in graphene. The special electronic properites of graphene arise from its special crystal structure. Graphene is a honeycomb carbon lattice, composed of a single crystal layer of graphite (see Fig. 2.6A-B). If we examine its crystal structure (Fig. 2.6C) we see that although each site is an identical carbon atom, the atoms on the **A** sublattice are crystallographically inequivalent to the atoms on the **B** sublattice. This is because an **A** atom is not in the same orientation to nearby atoms as is a **B** atom; consequently, we must view graphene as a triangular Bravais lattice with a two-atom basis. In reciprocal space, there exist two inequivalent corners of the Brillouin zone (arising from the triangular real-space lattice) which we call valleys, or K and K' (Fig. 2.7A).

In order to describe an electronic wavefunction in graphene, we use a superposition of sublattice wavefunctions.

$$\psi_K(\vec{r}) = a_K \psi_K^{(A)}(\vec{r}) + b_K \psi_K^{(A)}(\vec{r}) \tag{2.17}$$

Each of these wavefunction is a linear combitation of the atomic bloch wavefunctions on the **A** and **B** sites:

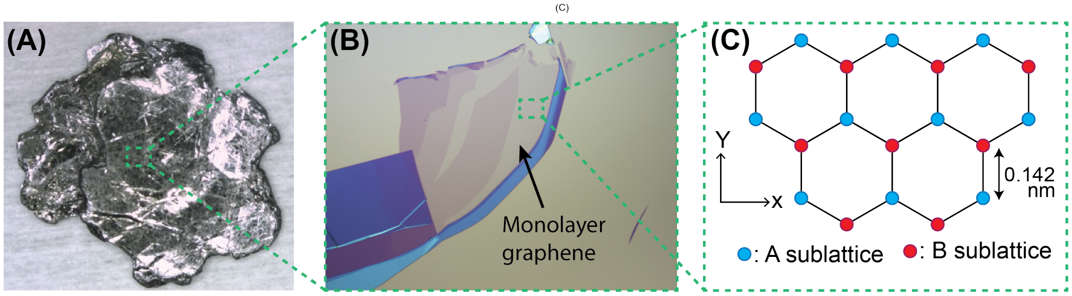

Figure 2.6: **Crystal structure of graphene.** **(A)** Bulk graphite from NGS Naturgraphit GmbH. **(B)** Graphene, a single layer of graphite. **(C)** The hexagonal graphene lattice, composed of two A and B sublattices.

$$\psi_K^{(j)}(\vec{r}) = \sum_{\vec{R}_l} e^{i\vec{k}\cdot\vec{R}_l}\phi^{(j)}(\vec{r} + \delta_j - \vec{R}_l) \tag{2.18}$$

where j = ($\mathbf{A}$, $\mathbf{B}$) and ϕ is centered at $(\vec{R}_l - \vec{\delta}_j)$

We now solve the Schrodinger Equation using this wavefunction:

$$H|\psi_k\rangle = E_k|\psi_k\rangle \tag{2.19}$$

where H is a Hamiltonian for a free particle plus a periodic potential: $H = \frac{\vec{p}^2}{2m} + \sum_i V(\vec{r} - \vec{R}_i)$ where the sum is over all atoms. Assuming nearest-neighbor hopping, meaning we only consider interactions between the **A** sublattice site and the **B** sublattice sites, we find the following Hamiltonian:

$$H_k = \begin{bmatrix} 0 & t\gamma_k* \\ t\gamma_k & 0 \end{bmatrix} \tag{2.20}$$

where t is the nearest-neighbor hopping parameter and γ_k is the sum of nearest-neighbor phase factors:

$$\gamma = e^{i\vec{k}\cdot\vec{\delta_1}} + e^{i\vec{k}\cdot\vec{\delta_2}} + e^{i\vec{k}\cdot\vec{\delta_3}} \tag{2.21}$$

where δ_1, δ_2, and δ_3 are the nearest neighbor vectors. The energies of the system are:

$$E_{\pm}(k) = \pm t|\gamma_k| = \pm t\sqrt{1 + 2\cos^2(\sqrt{3}k_y a) + 4\cos(\frac{\sqrt{3}}{2}k_y a)\cos(\frac{3}{2}k_x a)}. \tag{2.22}$$

This gives us the band structure shown in Fig. 2.7B, with the valence and conduction bands touching right at the K and K' points.

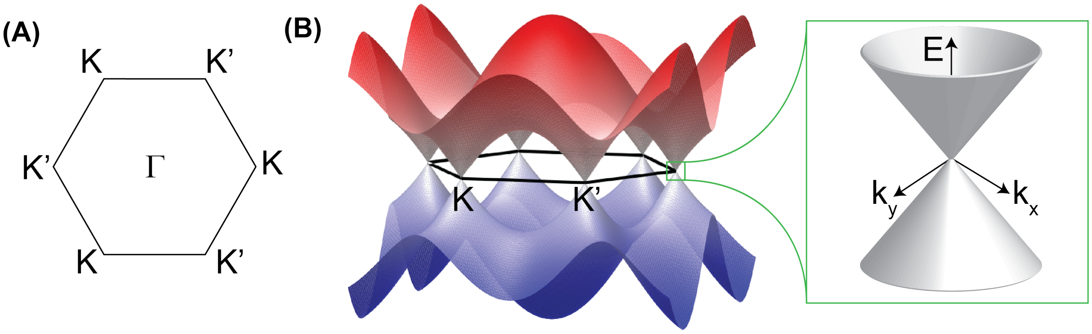

Figure 2.7: **The electronic structure of graphene.** **(A)** The Brillouin zone of graphene. Alternating corners of the BZ are inequivalent and labeled by K and K'. **(B)** The electronic band structure of monolayer graphene. The green box shows a zoomed-in image of the energy dispersion around the K point at low energies.

In undoped graphene the Fermi energy is right at these K and K' points, so we expand around them to get the low-energy Hamiltonians (Fig. 2.7B):

$$H_k = \hbar v_F \begin{bmatrix} 0 & k_x - ik_y \\ k_x + ik_y & 0 \end{bmatrix} = v_F \vec{p} \cdot \vec{\sigma} \tag{2.23}$$

$$H'_k = \hbar v_F \begin{bmatrix} 0 & k_x + ik_y \\ k_x - ik_y & 0 \end{bmatrix} = v_F \vec{p} \cdot \vec{\sigma}* \tag{2.24}$$

$$E \approx \pm \hbar v_F |\vec{k}| \tag{2.25}$$

where $v_F \approx 10^6$ m/s is the fermi velocity and σ denotes the Pauli matrices. We see that the energy dispersion is linear in momentum and is of the same form as the Dirac equation describing relativistic massless fermions. This is why we call the carriers in graphene Dirac fermions. We shall use these Hamiltonians to now solve for graphene in a magnetic field to see what the quantum Hall effect should look like in graphene.

2.2.2 Landau quantization in graphene

Again we write our kinetic momentum as a function of the lattice momentum and the vector potential:

$$\vec{\Pi} = \vec{p} + e\vec{A}. \tag{2.26}$$

We can rewrite our Dirac Hamiltonian as:

$$H_D = \hbar v_F \vec{\Pi} \cdot \vec{\sigma} = v_F \begin{bmatrix} 0 & \vec{\Pi}_x + i\vec{\Pi}_y \\ \vec{\Pi}_x + i\vec{\Pi}_y & 0 \end{bmatrix} \tag{2.27}$$

and we can solve this Hamiltonian using the ladder operator approach. Again we us the Landau gauge where p_y commutes with the Hamiltonian and can be treated like a c-number while p_x is treated like an operator. We find the gauge invariant commutation relation:

$$\left[\Pi_x, \Pi_y\right] = \frac{-i\hbar}{l_B^2}. \tag{2.28}$$

And use this to find appropriate ladder operators as:

$$\hat{a} = \frac{1}{\sqrt{2}}\frac{l_B}{\hbar}[\vec{\Pi}_x - i\vec{\Pi}_y] \tag{2.29}$$

$$\hat{a}^{+} = \frac{1}{\sqrt{2}}\frac{l_B}{\hbar}[\vec{\Pi}_x + i\vec{\Pi}_y]. \tag{2.30}$$

Note we are only going to solve the Hamiltonian for our K point, and would need to solve the K' Hamiltonian for the K' point. Our Hamiltonian looks like:

$$\hat{H} = \hbar\omega' \begin{bmatrix} 0 & \hat{a} \\ \hat{a}^{+} & 0 \end{bmatrix} \tag{2.31}$$

where $\omega' = \frac{\sqrt{2}v_F}{l_B}$ and the harmonic oscillator eigenstates are 2-spinors, shifted by $x_0 = kl_B^2$ in the x-direction (We omit the momentum eigenstates e^{iky} in the y-direction):

$$\psi_n = \begin{pmatrix} u_n \\ v_n \end{pmatrix}. \tag{2.32}$$

Again we find quantized energy levels:

$$E_n = \lambda\sqrt{2\hbar v_f^2 eBn}. \tag{2.33}$$

Here, our Landau levels vary with $\sqrt{B}$ (instead of linearly with B as in the 2DES case). Additionally, we find that we get both positive and negative LLs, which means our n=0 LL is composed of both electrons and holes. This is different from previous 2D systems in which a large band gap separates the electron band from the hole band. These systems could only host hole or electron carriers, while in graphene one can continuously tune between electrons and holes with a gate voltage. Another difference is that these LLs have an extra degeneracy, that of the valley index. Previous systems only had a 2-fold spin degeneracy, whereas graphene has a total 4-fold degeneracy (2 for spin and 2 for valley). Since each Landau level is four-fold degenerate, when we look at the transport we find plateaus at intervals of $4e^2/h$, as shown in (Fig. 2.8).

It is also important for our purposes to emphasize the unique n=0 LL and note that if you solve for the first spinor component, we get 0 (solving for the second spinor component, you get the groundstate of the harmonic oscillator):

$$\psi_{n=0} = \begin{pmatrix} 0 \\ |n=0\rangle \end{pmatrix}. \tag{2.34}$$

Since the basis for our Hamiltonian was the sublattices, our wavefunction is localized completely on one sublattice. If we were to solve the Hamiltonian for our K′ point, we would find that those wavefunctions are completely localized on the other sublattice. This means that in the n=0 LL, our valley and sublattices are completely coupled – an important point to remember when the spin and valley symmetries in the system begin to break.

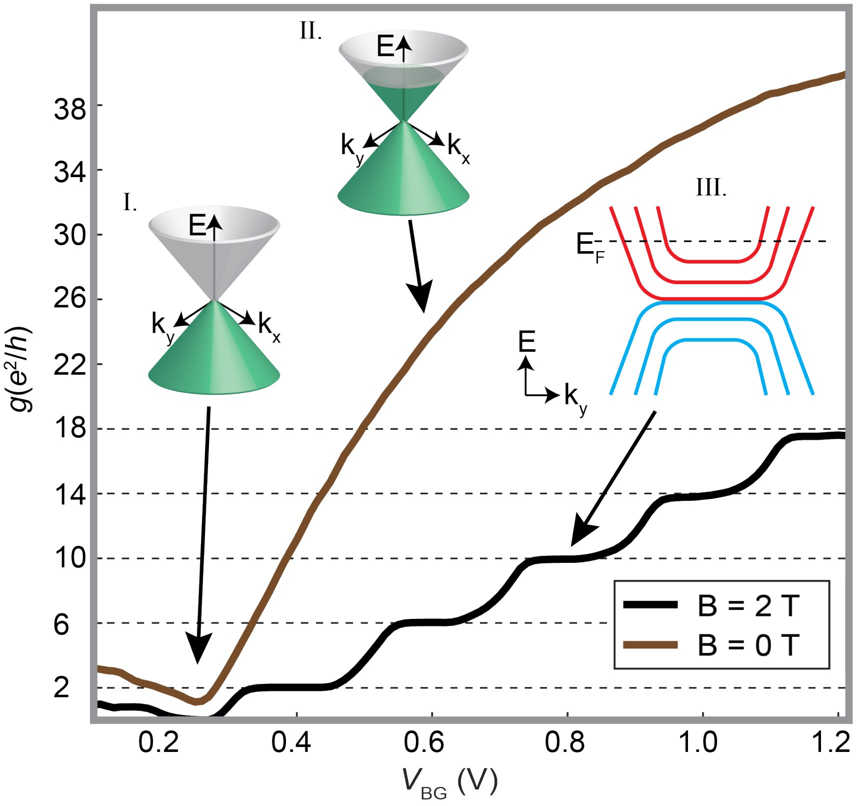

Figure 2.8: **Two-terminal conductance measurement of monolayer graphene.** The brown line shows a measurement in the absence of an applied magnetic field. The conductance reaches a minimum when the Fermi level is exactly where the electron and hole bands touch in (I); we call this the Dirac point. It is offset from 0V on the backgate due to impurities in the graphene and effects of the substrate. As we increase the gate voltage in (II), we fill more electron states and the conductance increases. At higher magnetic fields (2T), we now fill flat, Landau bands (III) and begin to see quantized plateaus emerge in transport. Here we focus primarily on electron (instead of hole) transport because the leads are electron-doped in this measurement, therefore measurements are only clear on the electron side.

2.3 Quantum Hall ferromagnetism

At high magnetic fields in both semiconductor 2D materials as well as graphene, instead of plateaus at intervals of every $2e^2/h$ or $4e^2/h$, one begins to see plateaus at every integer. These are called broken symmetry states because they indicate that the spin and valley degeneracies are being broken. The first experiments to show these states in graphene were done at the National High Magnetic Field lab in Tallahassee where the quantum Hall effect was investigated up to 45T [14]. Now, with cleaner samples experimentalists are able to see these broken symmetry states at less than 1T.

These broken symmetry states can be understood by considering the spatial distribution of electrons in each LL. In a fully ferromagnetically aligned system where all spins are parallel, the spin part of the wavefunction is symmetric with respect to exchange of any two electrons:

$$\psi\rangle = \phi(z_1, z_2, ...z_n)| \uparrow\uparrow\uparrow\uparrow\rangle \tag{2.35}$$

The spatial component of the wavefunction will necessarily be antisymmetric due to the Pauli exclusion principle, and it will vanish when two particles approach each other. Therefore electrons of the same spin will experience less Coulomb repulsion than unaligned spins, as depicted in Fig. 2.10A [3].

Even if there is no anisotropy in the system, it will spontaneously order into a completely polarized state. This is called spontaneous symmetry breaking, and the energy gap that forms is called an “exchange gap”, because it arises due to exchange interactions between electrons [15, 16, 3] This creates completely spin- (and valley-

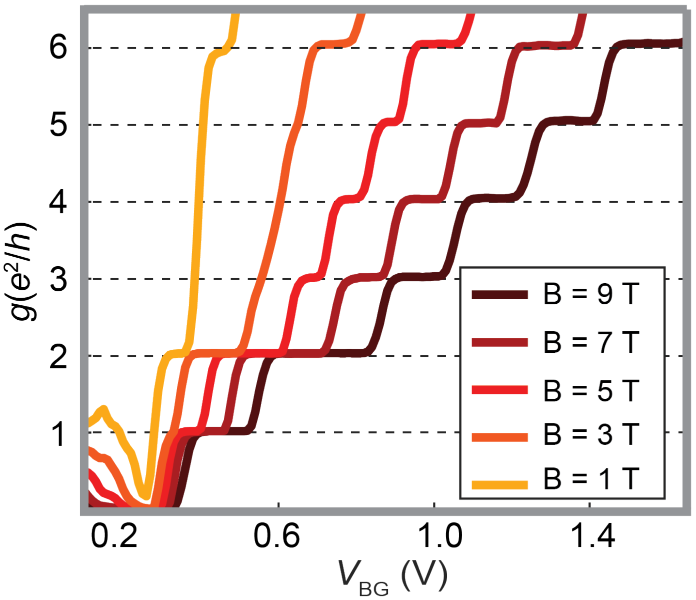

Figure 2.9: **The evolution of LLs in graphene transport measurements.** At low field (B = 1T) only the 4-fold degenerate plateaus at $\nu = 2$ and $\nu = 6$ are evident. As the magnetic field is increased, we see broken symmetry plateaus at every integer emerge.

, in the case of graphene) polarized Landau levels. In graphene, electron-electron interactions give rise to ferromagnetic phases when the N=0 LL is at quarter- and three-quarter-filling [17, 18, 14, 19, 20]. Such QH ferromagnets have an insulating topological bulk and spin-polarized edge states. The spins in a quantum Hall ferromagnet are completely polarized because the energies of all states in a Landau level are degenerate, and there is no kinetic energy cost to polarization.

This exchange gap energy is much larger in magnitude than different anisotropy energies present in these systems. The simplest of these anisotropies is the Zeeman

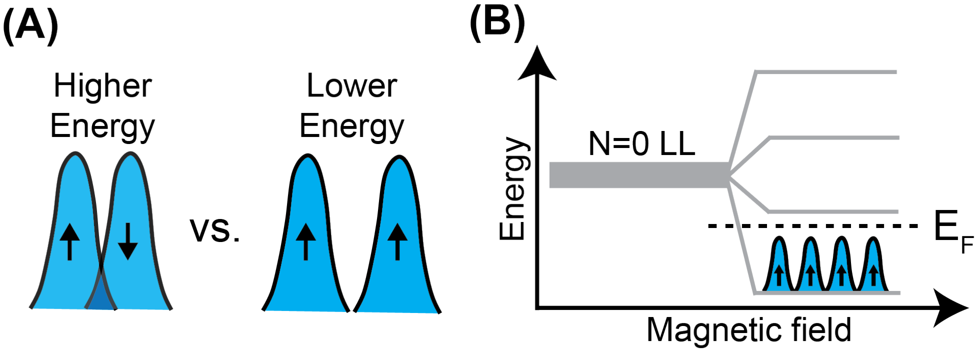

Figure 2.10: **Exchange induced quantum Hall ferromagnetism.** **(A)** When spins are polarized their wavefunctions cannot overlap and the electrons experience less Coulomb repulsion. Consequently, a spin polarized state is lower energy than a spin-unpolarized state. **(B)** As the magnetic field increases, the 4-fold degenerate Landau level will split into four polarized, broken symmetry states.

effect, which dictates which spin-direction the lowest energy state will explicitly order in to. Because spin-orbit is very weak in graphene, the Zeeman effect is the only relevant factor that affects spin symmetry. Additionally, in graphene there is also valley anisotropy that arises from short-range electron-electron interactions and electron-phonon interactions [17, 21, 22]. Additionally, in the $\nu = 0$ LL the valley and sublattice are completely coupled (recall the derivation of eqn. 2.34), so sublattice anisotropies are essentially identical to valley anisotropies.

The hierarchy of energy scales is shown in Fig. 2.11 where we see that the cyclotron energy gaps ($E_n = \hbar v_F \frac{\sqrt{2}}{l_B} \sim 400\sqrt{B[\mathrm{T}]}\mathrm{K}$) and Coulomb energy gaps ($E_C = \frac{e^2}{\epsilon l_B} \sim 100\sqrt{B[\mathrm{T}]}\mathrm{K}$) are much larger than the leading anisotropy energies, the Zeeman energy

($E_Z = g\mu_B B \sim B$[T]K) and the lattice scale interactions ($E_{SR} = \frac{a}{l_B}E_C \sim B$[T]K) (where μ_B is the Bohr magneton, and a is the graphene lattice constant) [23, 17]. We see plateaus at every integer when the sample is clean enough to escape the effects of disorder broadening, and the magnetic field is large enough for the symmetries to break spontaneously.

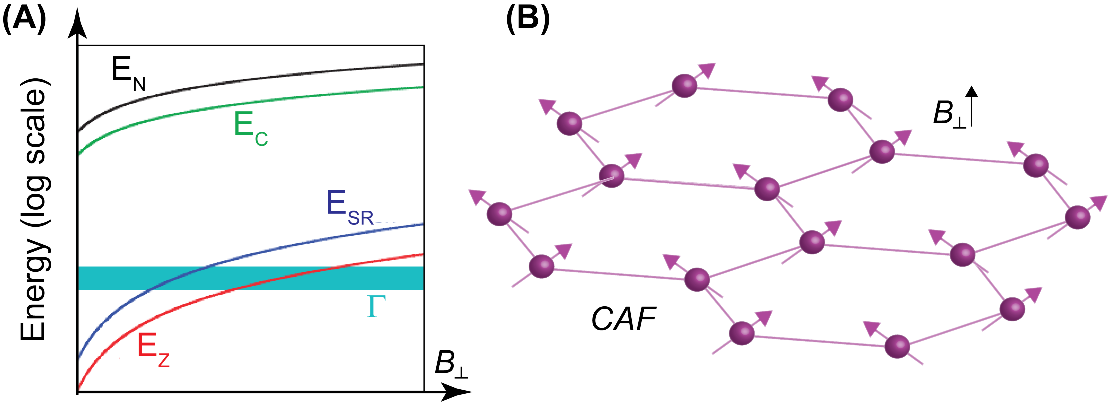

Figure 2.11: **Energy scales involved in quantum Hall ferromagnetism and the canted antiferromagnetic phase.** **(A)** Energy hierarchy, adapted from ref. [23]. At finite magnetic fields the cyclotron energy (E_N) and Coulomb exchange energies (E_C) are much larger than the anisotropy energies Zeeman (E_Z) and lattice scale interaction (E_{SR}), as well as disorder broadening (Γ). **(B)** The canted antiferromagnet at $\nu = 0$. The canting angle depends on the relative strength of the Zeeman energy, which depends on B_{total}, and the antiferromagnetic exchange energy, which depends only on $B_\perp$.

For quarter filling of the Landau level in graphene, the lowest energy ground state is both spin and valley polarized. Half-filling is more complicated because electrons with identical quantum numbers (identical spin and valley) cannot overlap due to

Pauli exclusion. Consequently, we cannot have a state cannot be both spin- and valley- polarized. Consequently, the ground state of the $\nu = 0$ state depends sensitively on the strengths of the different anisotropies in the system. Experimentally, when people first looked at the $\nu = 0$ state they saw that it became highly insulating with increasing magnetic field [24], and also that it was spin unpolarized ([23]). In 2014, a group at MIT showed that you can tune the $\nu = 0$ state continuously between a canted antiferromagnet that is insulating and a ferromagnetic quantum spin Hall phase that has counterpropagating edge states and a conductance nearly quantized at $2e^2/h$ [25].

2.4 Edge state equilibration

As we saw in section 2.1.2, understanding edge states has aided us immensely in our understanding of the quantum Hall effect. A number of studies looking at the transmission and reflection of edge states helped to solidify the edge state picture as an important model needed to understand the QHE [26]. For instance, it was seen that if you gate a region in the middle of a device into a lower filling factor, with fewer edge states, edges will be reflected at this barrier, as shown in Fig. 2.12A.

Alternatively, by gating the central region of a device into a higher filling factor (Fig. 2.12B), one can look at how two edge channels at different energies might look after flowing along next to each other after some distance, otherwise known as how the edge states equilibrate. As a simple example let us first assume that the $\nu = 2$ and $\nu = 1$ edges in Fig. 2.12B do not equilibrate with each other over the distance that they run next to each other. Assuming a chemical potential of μ on one lead

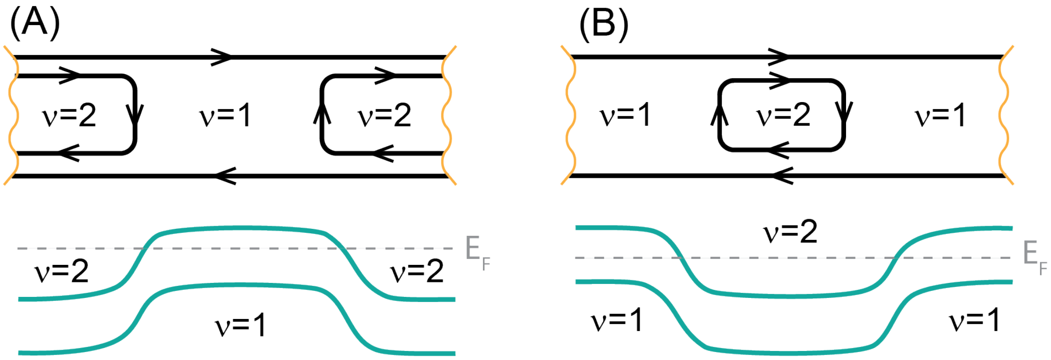

Figure 2.12: **Reflection and transmission of edge states in a device where the filling factor in the central region is changed.** **(A)** The central region is at a lower filling factor and the $\nu = 2$ edge is reflected. **(B)** The central region is at a higher filling factor and the edge states can equilibrate with the extra center edge.

and 0 at the other, we expect to measure a current:

$$I = (\mu - 0)\frac{e}{h} \tag{2.36}$$

which will give us a conductance:

$$\sigma = \frac{I}{V} = \frac{e^2}{h} \tag{2.37}$$

Next, assume we put some kind of equilibration site (perhaps a small piece of metal) at one edge so the two edge states completely equilibrate with each other – i.e. they come to the same energy. This is shown in Fig. 2.13A. This will simply cause the inner edge to float up to the same chemical potential μ as in the upper edge, and we should again measure a conductance of e^2/h, which is not very interesting. Finally,

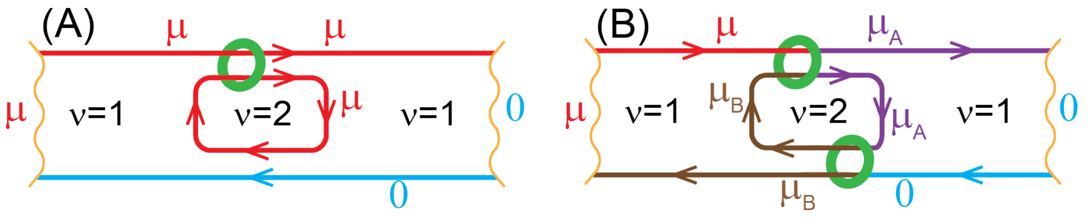

Figure 2.13: **Edge equilibration experiment. (A)** The conductance remains unchanged with just one equilibration site. **(B)** The conductance changes once we have two equilibration sites.

we put equilibration sites on *both* edges, allowing electrons to backscatter into the opposite side of the device Fig. 2.13B. The current we expect in this case is:

$$I = (\mu - \mu_B)\frac{e}{h} \tag{2.38}$$

We solve for the chemical potential μ_B in terms of μ by writing down a set of equations for the current before and after each equilibration site:

$$(\mu + \mu_B)\frac{e}{h} = 2\mu_A\frac{e}{h} \quad \text{and} \quad (\mu_A + 0)\frac{e}{h} = 2\mu_B\frac{e}{h} \tag{2.39}$$

$$\Rightarrow \mu_B = \frac{\mu}{3} \tag{2.40}$$

and find the resulting current to be:

$$I = (\mu - \frac{\mu}{3})\frac{e}{h} = \frac{2}{3}\frac{e}{h}. \tag{2.41}$$

Thus, if we measure a two terminal conductance of $\frac{e^2}{h}$ then the edges did not equilibrate at all, and if we measure a conductance of $\frac{2}{3}\frac{e^2}{h}$ then the edges have equilibrated completely. Experiments of this flavor have been performed extensively in GaAs quantum wells, and it has been observed that it is possible for two separately populated edge channels to travel adiabatically across large distances without equilibrating, sometimes hundreds of microns [27, 28, 29, 30]. For degenerate edge states, conditions for equilibration can provide information about how deep into a Landau level the system is [29]. For non-degenerate states, the equilibration of edge states gives insight into the mechanisms of spin scattering [30], and in the case of graphene, valley scattering [31]. The transport experiments described in this thesis rely heavily on the information we can gather from these types of edge equilibration experiments.

Chapter 3

Mach-Zehnder interferometry using spin- and valley-polarized quantum Hall edge states in graphene

3.1 Introduction

Interference experiments have played a central role in answering some of the most historically pressing questions in physics. Young's double slit interference experiment demonstrated fringes that arose from splitting a single source of light and then coherently recombining the two beams – thereby cementing the idea of light as a wave [32]. About 80 years later, the famous Michelson-Morley experiment measured the speed of light traveling in different directions by examining the interference fringes produced.

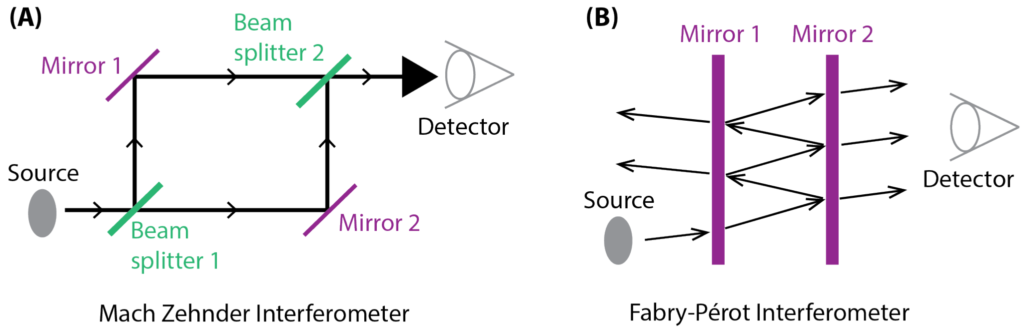

Figure 3.1: **Mach-Zehnder and Fabry-Perot interferometers.** **(A)** Mach-Zehnder interferometer **(B)** Fabry-Perot interferometer.

They found that light traveled at the same speed no matter the direction, disproving the notion of an "aether wind" across the Earth's surface, and helped pave the way for the discovery of special relativity [33]. Besides these seminal experiments, light interferometry has been used to detect gravitational waves [34], to study quantum entanglement [35], and has been used in a large number of industrial applications.

One of the most widely used interferometers is the Mach-Zehnder interferometer (MZI), a type of amplitude-splitting interferometer. In these types of interferometers, an incident light wave on a beamsplitter is split into a reflected beam and a transmitted beam, both with lower amplitudes than the original beam. In an MZI one beam is first split by a beam splitter and then recombined at a second beamsplitter, as shown in Fig. 3.1A [36]. The MZI is sensitive to phase changes interference between the the recombined beams, arising from different path lengths in either of the two arms.

Another well known type of interferometer is the Fabry-Perot interferometer. It can be thought of as a multiple path resonant cavity where two beam splitters are

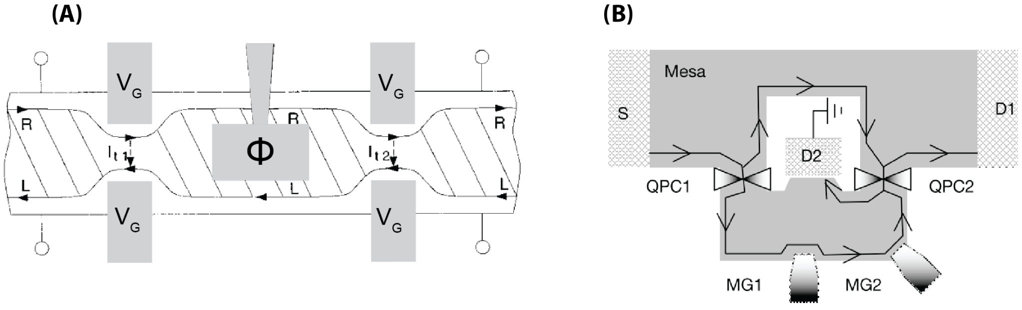

Figure 3.2: **Electronic Mach-Zehnder and Fabry-Perot interferometers in quantum Hall systems.** **(A)** Fabry-Perot interferometer adapted from [38]. **(B)** Mach-Zehnder interferometer adapted from [39]

placed in series, and transmission through the cavity only occurs a particular wavelengths determined by properties of the cavity (Fig. 3.1B) [36].

3.1.1 Electron interferometry in the quantum Hall regime

The wave-like properties of the electron allow us to study beams of electrons using interferometry much in the same way as we can with light [37]. We can potentially extract a great deal of information from these systems, as the phase of an electron can be changed by effects from Coulomb interactions, changes in the magnetic field, fractional and non-Abelian statistics and Coulomb interactions [11, 38, 39, 40, 41, 42]. Quantum Hall edge states provide ideal electron beams for electron interferometry as they are single-mode channels that are protected from backscattering [11]. Furthermore, they can be positioned via electrostatic gating and coupled with with quantum point contacts [43] acting as the beam-splitters and ohmic contacts acting as the detectors.

3.1.2 Aharonov-Bohm effect

For systems where we do not need to consider electron-electron interactions, the relative phase between the two beams of the MZI should be determined by the Aharonov-Bohm effect [44]. The total magnetic flux in the system is given by $\Phi = B \cdot A$, where B is the uniform magnetic field and A is the area enclosed by the loop of the interferometer. The interference, measured via the conductance of the interferometer, will have a period of one flux quantum Φ_0. In experiments, we should see conductance modulations as a function of the magnetic field, as well as the area, which is typically tuned with a metal gate.

Previous to the work done here, the Fabry-Perot interferometer has been simpler to fabricate in quantum Hall systems than the MZI. This is because in order to build an MZI, a large ohmic contact in the middle of the device needed to be connected to an outside ohmic via an air-bridge. This required large areas, which necessarily required small B field oscillations in order to see the Aharonov-Bohm effect (see Fig. 3.2B). However, interference data from Fabry-Perot interferometers can be quite a bit more difficult to understand because of the multiple contributing paths. We will focus here on realizing a Mach-Zehnder interferometer and refer the reader to thorough reviews on the Fabry Perot interferometer in [45] and [46].

Detecting fractional statistics

Mach-Zehnder interferometry is regarded as one of the most promising routes for studying fractional and non-Abelian statistics [47, 40]. At a very basic level, the fractional quantum Hall effect (FQHE) can be thought of as a sort of integer quantum Hall effect with fractionally charged quasiparticles (e/m) where m is an integer. Naively, one might assume that the inteference of these quasiparticles would result in a magnetic field period multiplied by a factor of m. However, these quasiparticles are expected to obey fractional braiding statistics, which electron interferometry experiments should be sensitive to. Signatures of fractional statistics might manifest as regular, discrete phase shifts in the measured interference when the number of enclosed quasi-particles is changed [46]. Although there have been interferometry studies of fractional QH edge states [48, 49, 50, 51, 52], indisputable proof of fractional statistics has yet to be shown. One of the motivations for these experiments was to provide a new platform, graphene, to potentially investigate interference in the fractional quantum Hall regime.

3.1.3 Electron interferometry in graphene

The energy gaps between Landau levels (LLs) allow for the creation of interferometers and quantum point contacts even in materials that do not have a zero-field bandgap, such as graphene [53, 54]. Graphene may provide an advantage compared to conventional GaAs edge-channel interferometers [41, 55, 42, 56] as the absence of a band gap allows the creation of hole- and electron-like edge channels that naturally meet, co-propagate, and separate at gate-defined PN interfaces [57, 58]. The additional valley degree of freedom and the associated unique nature of graphene quantum Hall states [59, 23] open up new opportunities for addressing long-sought goals of electron interferometry such as the observation of non-Abelian statistics [60]. In addition, the valley isospin provides new possibilities for controlling inter-channel scattering [61], a requirement for creating edge-channel interferometers. However, even though graphene PN junctions in the quantum Hall regime have been studied extensively [31, 57, 58, 62, 63, 64, 65, 66], creating an edge-channel interferometer using spin- and valley-polarized edge channels has remained an outstanding challenge.

3.1.4 Summary of our experimental findings

In this experiment, we engineer MZIs consisting of same-spin, opposite-valley quantum Hall edge channels that co-propagate along a PN junction in graphene. Using magnetic and trans-junction electric fields, we can tune into a regime in which either one or both pairs of the same-spin edge channels belonging to the zeroth Landau level (zLL) form MZIs that coherently mediate the cross-junction transport (Fig. 3.3A). We find that these channels can be well isolated from those belonging to other Landau levels (LLs), enabling us to study a target interferometer over a large range of electric fields and tune into regimes with visibilities as high as 98%. By studying PN interfaces of different lengths, we show that the interferometer beam-splitters are located where the PN interface meets the physical graphene edges, which we attribute to strong inter-valley scattering at the physical graphene edge and the absence of inter-valley scattering along the gate-defined edge. We independently verify this conclusion using a device in which we can tune the number of edge channels co-propagating along either a physical or gate-defined edge.

3.2 Experimental results

3.2.1 Constructing a Mach-Zehnder interferometer in a graphene PN junction

To construct a MZI of spin- and valley-polarized edge channels, we use a hexagonal boron nitride (hBN) encapsulated monolayer of graphene (see Fig. 3.3B and section A.1). We tune into the quantum Hall regime using a perpendicular magnetic field B, and define two regions of different charge densities n_{T} and n_{B} using a bottom gate that affects both n_{T} and n_{B} and a top gate that affects only n_{T} (Fig. 3.3B). The number of edge channels in these regions is given by the filling factors $\nu_{\mathrm{T,B}} = (h/eB)n_{\mathrm{T,B}}$, where e is the electron charge and h is Planck's constant. The observation of integer quantum Hall steps in a measurement of the two-terminal conductance at $B = 4$ T in the regime where $\nu_{\mathrm{T}} > 0$ and $\nu_{\mathrm{B}} > 0$ confirms that the spin- and valley-degeneracy is lifted (fig. A.1).

Next, we create a PN junction by tuning into the regime where $\nu_{\mathrm{T}} < 0$ and $\nu_{\mathrm{B}} > 0$ and study which edge channels mediate charge transport across the junction. When we measure the conductance g as a function of $\nu_{\mathrm{T}} < 0$ and $\nu_{\mathrm{B}} > 0$ at $B = 4$ T , we observe four regions with distinct ranges of conductance values, as well as the first indications of conductance oscillations (Fig. 3.3C). In region I, the conductance of the junction is near zero, which we attribute to the situation depicted in the top panel of Fig. 3.3A (where $\nu_{\mathrm{B}} = 1$ and $\nu_{\mathrm{T}} = -1$). Here, one N-type spin-down and one P-type spin-up edge channel co-propagate along the junction. As these channels have opposite spin, inter-channel scattering is suppressed [31]. When we

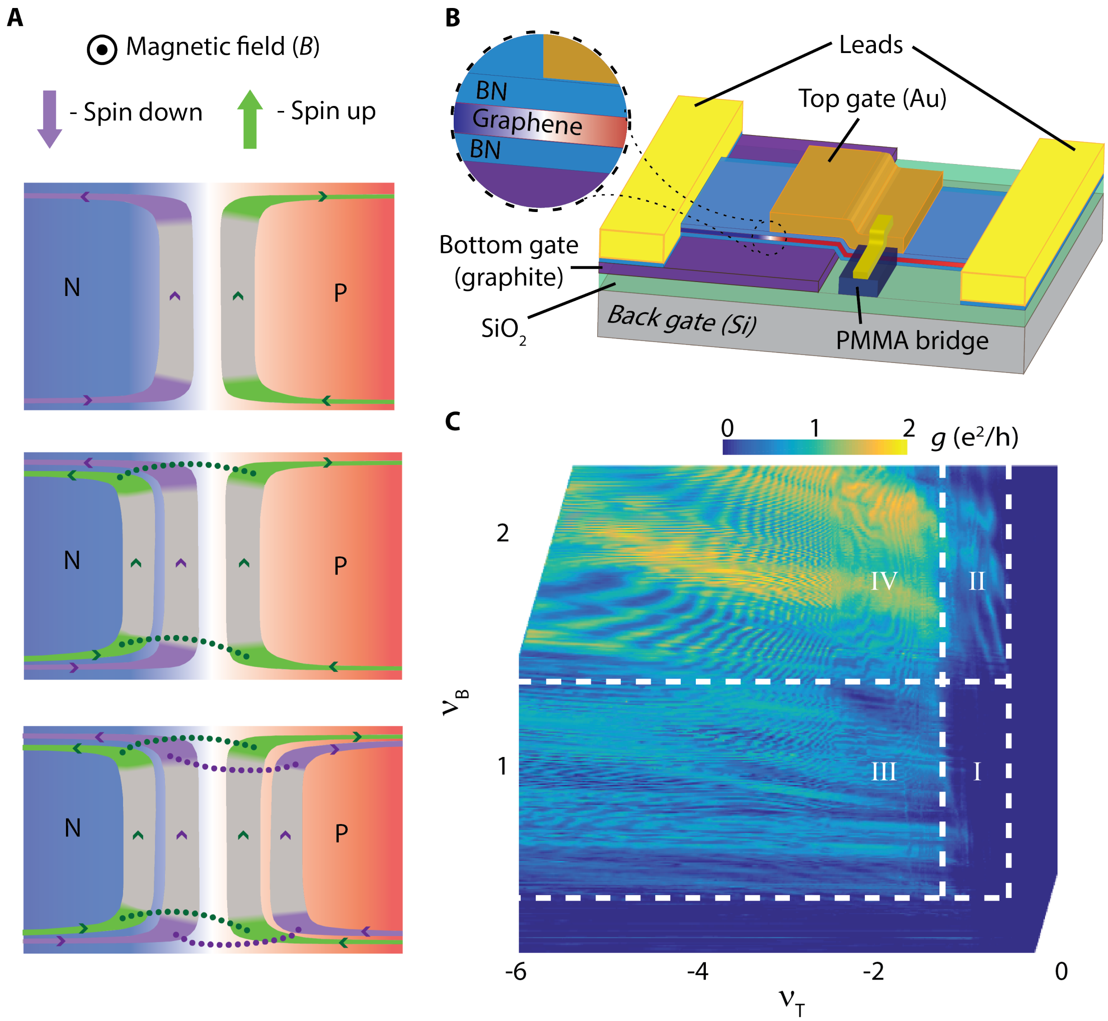

Figure 3.3: **Creating a Mach-Zehnder interferometer using spin- and valley-polarized quantum Hall edge channels.** **(A)** Schematic illustration of the formation of Mach-Zehnder interferometers (MZIs) at a graphene PN junction. Green and purple denote quantum Hall edge channels of opposite spin. Top panel: at $(\nu_\mathrm{B}, \nu_\mathrm{T})$=(1,-1), where ν_B (ν_T) is the filling factor in the N- (P-) region, two edge channels run along the interface. Their opposite spin suppresses inter-channel scattering.

Figure 3.3: (Continued) Middle panel: at (ν_{B},ν_{T})=(2,-1), a pair of spin-up edge channels forms a MZI. Inter-channel scattering occurs at the ends of the junction as indicated by dotted lines. Bottom panel: at (ν_{B},ν_{T})=(2,-2), two pairs of same-spin edge channels form two MZIs. **(B)** Device 1: an edge-contacted monolayer graphene flake encapsulated in hexagonal boron nitride (hBN). The top gate (Au) and bottom gate (graphite) define the PN junction (P: red color, N: blue color). The top (bottom) hBN gate dielectric is 20 (30) nm thick. The top gate is contacted by a lead that runs over a bridge fabricated from hard-baked PMMA to avoid shorting to the graphene flake. The back gate (Si) is used to strongly increase the p-doping of the graphene leading up to right lead and reduce the contact resistance. The SiO_2 back-gate dielectric is 285 nm thick. **(C)** Two-terminal conductance of device 1 in the PN regime at B = 4 T. We distinguish four regions (dashed boxes). Region I corresponds to (ν_{B},ν_{T}) = (1,-1). Region II corresponds to $\nu_{\mathrm{T}} = -1$ and $\nu_{\mathrm{B}} \geq 2$. Region III corresponds to $\nu_{\mathrm{B}} = 1$ and $\nu_{\mathrm{T}} \leq -2$. Region IV corresponds to $\nu_{\mathrm{B}} \geq 2$ and $\nu_{\mathrm{T}} \leq -2$.

cross from region I into region II, we begin to observe transport across the junction. We attribute this to an additional spin-up edge channel having entered on the N-side (so that $\nu_{\mathrm{B}} = 2$ and $\nu_{\mathrm{T}} = -1$) and that electrons in this channel can scatter into the spin-up channel on the P-side (see middle panel in Fig. 3.3A). The observed conductance ranges approximately between 0 and e^2/h, consistent with one pair of edge channels mediating transport across the junction. Similarly, in region III we obtain the situation in which $\nu_{\mathrm{B}} = 1$ and $\nu_{\mathrm{T}} = -2$, and we attribute the observed conductance to scattering between the two spin-down edge channels. Strikingly, in region III the conductance does not change notably as we keep adding edge channels on the P-side (going to $\nu_{\mathrm{B}} = 1$ and $\nu_{\mathrm{T}} < -2$). We conclude that these additional channels do not contribute to the trans-junction conductance, presumably because they belong to a higher LL which makes them spatially too distant from the PN interface. Crossing into region IV ($\nu_{\mathrm{B}} \geq 2$ and $\nu_{\mathrm{T}} \leq -2$), we observe that the average conductance increases and ranges between 0 and $2e^2/h$. We attribute this to two pairs of same-spin edge channels mediating transport across the junction. Again, we see no sign of edge channels belonging to higher LLs entering the system and contributing to the trans-junction conductance. We conclude that the edge channels belonging to the zLL mediate the trans-junction conductance, well isolated from edge channels belonging to higher LLs.

Markedly, in region III, the conductance does not change notably when we keep adding edge channels on the p-side (going to $\nu_B = 1$ and $\nu_T < -2$). We conclude that these additional channels do not contribute to the trans-junction conductance, presumably because they belong to a higher LL, which makes them spatially too distant from the pn interface, which has also been seen in the study of Klimov *et al.* [67]. Crossing into region IV ($\nu_B \geq 2$ and $\nu_T \leq -2$), we observe that the average conductance increases and ranges between 0 and $2e^2/h$. We attribute this to two pairs of same-spin edge channels mediating transport across the junction. Again, we see no sign of edge channels belonging to higher LLs entering the system and contributing to the transjunction conductance. We conclude that the edge channels belonging to the zLL mediate the trans-junction conductance, well isolated from edge channels belonging to higher LLs.

The relative isolation of the edge channels that belong to the zLL allows us to study a target pair of edge channels over a large range of filling factors. As we increase the magnetic field to $B = 9$ T and concentrate on region III, in which $\nu_\mathrm{B} = 1$ and $\nu_\mathrm{T} \leq -2$, we observe a striking pattern of conductance oscillations (Fig. 3.4A) whose key features such as shape and periodicity depend on both ν_B and ν_T. These oscillations cannot be explained by semi-classical snake states or similar low-field phenomena [68, 69, 70, 71] since in our device electron transport is mediated by quantum Hall edge channels. Instead, as we will further argue below, the well-defined periodicity of these oscillations indicates that scattering between the two edge channels that mediate the cross-junction transport occurs at only two points along the junction. These points form the beamsplitters that define our MZI. Its conductance, in units of e^2/h, is given by

$$g = |r_1 t_2|^2 + |t_1 r_2|^2 + 2|t_1 t_2 r_1 r_2| {\scriptstyle\cos}(\phi + \phi_0) \tag{3.1}$$

where t_i (r_i) is the transmission (reflection) amplitude of the i-th beamsplitter, with $|r_i|^2 + |t_i|^2 = 1$. The phase $\phi = \frac{2\pi BA}{\Phi_0}$ arises from the Aharonov-Bohm effect, where

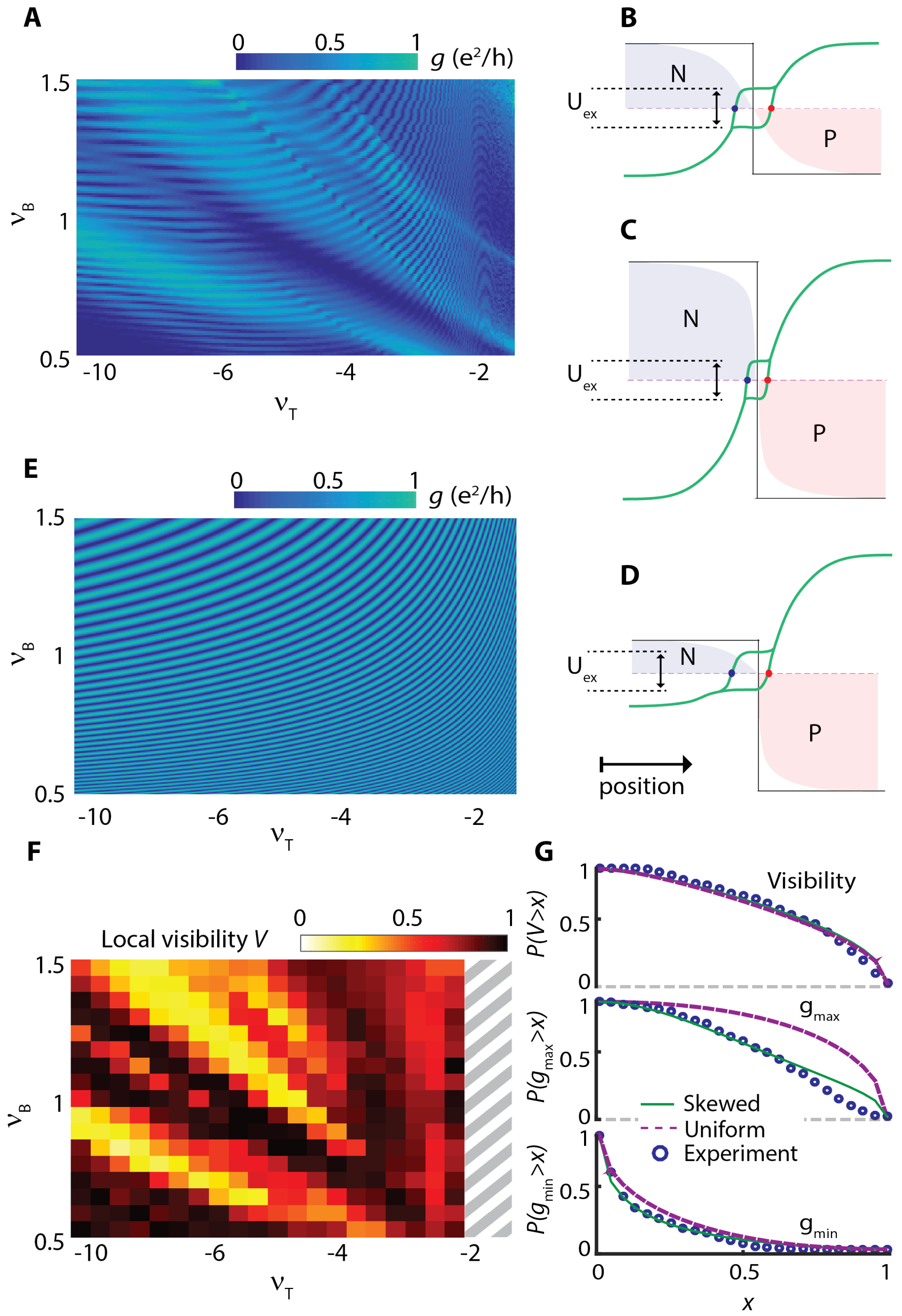

Figure 3.4: **Characterization of a single Mach-Zehnder interferometer. (A)** Two-terminal conductance of device 1 at $B = 9$ T, over a range of filling factors corresponding to a single interferometer at the PN junction.

Figure 3.4: (Continued) **(B)** Modeling the charge-density dependence of the distance between the edge channels that form a MZI. The red and blue shading illustrates the spatial variation of the charge density close to the PN junction. The green line illustrates the spatial variation of the energies of the exchange-split $\nu = 1$ and $\nu =$ -2 Landau sublevels. The edge channels are located at the positions where these sublevels intersect the Fermi energy. The distance between the edge channels determines the flux through the interferometer. Far from the PN junction, where the lowest LL is completely empty ($\nu = 2$) or completely full ($\nu = 2$), the exchange splitting U$_{ex}$ vanishes. Near the PN junction, however, the electronic ground state can develop an imbalance in the valley occupation, leading self-consistently to a non-zero U$_{ex}$. **(C)**, Increasing the electron and hole densities decreases the distance between the edge channels. **(D)**, A strong imbalance between the electron and hole densities. **(E)**, Simulation of the two-terminal conductance as a function of filling factors based on the model sketched in (B-D). **(F)** Local visibility of the conductance oscillations observed in (A). The grey dashed box indicates where the visibility was not extracted due to non-resolved oscillations. **(G)** Blue circles: Experimentally determined probability of finding a visibility, g_{max}, or g_{min} greater than x. Visibility is extracted from the color plot in (F); g_{min} and g_{max} are extracted from the color plots in Fig. A.3(A and B). Purple dashed line: The theoretical prediction based on MZIs with beamsplitters described by random scattering matrices that correspond to beamsplitter transmission probabilities uniformly distributed between 0 and 1. Green solid line: The theoretical prediction based on MZIs with beamsplitters described by a skewed distribution of transmission probabilities (fig. A.3C and section A.3).

$\Phi_0 = h/e$ is the flux quantum, A the effective area enclosed by the two edge channels, and ϕ_0 is an unknown phase associated with the beamsplitters.

Since the measurement in Fig. 3.4A is performed at a fixed magnetic field, we attribute the conductance oscillations to a changing distance between the two edge channels and a resulting changing flux through the interferometer. We can analyze the charge-density-dependent locations of these channels by determining where the two corresponding exchange-split Landau sublevels cross the Fermi energy, using a simple model for the spatial dependence of the sublevel energy (Fig. 3.4B-D and A.2). This model indicates that as the charge densities increase (from Fig. 3.4B-C), the edge-channel separation decreases. Furthermore, when the charge density is small (large) on a particular side of the junction, the edge-channel separation is relatively sensitive (insensitive) to the charge density on that side of the junction (Fig. 3.4D). Figure 3.4E shows that this model reproduces the key features of the data in Fig. 3.4A. Further data in the $\nu_{\mathrm{B}} \geq 2$ and $\nu_{\mathrm{T}} \leq -2$ regime, in which two MZIs act simultaneously (as depicted in the bottom panel of Fig. 3.3A), are shown in fig. A.2.

3.2.2 Beamsplitter characteristics

The visibility of the oscillations in a MZI depends on the phase coherence and the transmission characteristics of the beamsplitters. We analyze the range of visibilities observed in the measurement shown in Fig. 3.4A by dividing the measurement range into a grid and calculating the local visibility $V = (g_{\max} - g_{\min})/(g_{\max} + g_{\min})$, with $g_{\max}$ and $g_{\min}$ the maximum and minimum conductance within each block (Fig. 3.4F and fig. A.3A-B). In Fig. 3.4G we plot the resulting experimental cumulative probability distribution function that indicates the probability of finding a visibility,g_min, or g_max greater than x. We compare these distributions to a theoretical prediction that is based on the assumption that the incoming and outgoing channels of each of the two beamsplitters of the MZI are connected by random U(2) matrices in valley space (see section A.3). This comparison indicates that in the measurement of Fig. 3.4A, the beamsplitter transmission probabilities are not perfectly uniformly distributed between 0 and 1 (Fig. 3.4G) but are instead somewhat skewed toward lower trans-junction conductance (fig. A.3C and section A.3). Remarkably, in several regions of the conductance map (Fig. 3.4A) we find visibilities as high as 98%, indicating near-perfect phase coherence along the PN interface. Additionally, in some regions the conductance oscillates nearly between 0 and e^2/h, indicating nearly 50/50 beam splitters. Further insight into beamsplitter transmission probabilities yielding a particular Mach-Zehnder visibility can be gained from fig. A.3(D-E).

3.2.3 Dependence of the Mach-Zehnder interference on magnetic field and DC voltage bias

Next, we tune to a region of high visibility and study the conductance as a function of B and a DC voltage bias V_{DC} (Fig. 3.5A). We observe that the visibility stays near-unity for $|V_{\mathrm{DC}}| < 0.5$ mV (Fig. 3.5B), and decreases at larger $|V_{\mathrm{DC}}|$, which may be due to thermal averaging or electron-electron interactions [39, 56]. For the 8 to 9 T field range of Fig. 3.5C, measurements at $V_{\mathrm{DC}} = 0$ show a constant oscillation period ΔB, which is consistent with an assumption that the area enclosed by the interferometer is constant and given by $A = \frac{\Phi_0}{\Delta B}$. Subject to this assumption, we determine an edge-channel separation of 52 nm. Oscillations with V_{DC} are also observed (Fig. 3.5D) indicating a bias-dependent edge-channel separation, which may be a result of a bias-induced electrostatic gating effect [56]. We note that at larger filling factors we see multiple frequencies, changing frequency with field, and lobe structures, which have previously been attributed to Coulomb interactions in GaAs devices [41, 42, 56] (fig. A.4). We leave the analysis of these effects to a future study.

3.2.4 Varying the length of the PN interface

To confirm that the beamsplitters are located where the PN interface meets the physical graphene edges, we measure the MZI oscillation frequency as a function of the interface length. We use device 2 (Fig. 3.6A-B), which has five top gates (TG1 to TG5) of varying lengths that we can address individually in two-terminal conductance measurements by using the appropriate leads. Using top and bottom gates to control the filling factors in the top-gated and non-top-gated regions, ν_T and ν_B respectively, we can tune into a regime where $\nu_T < 0$ and $\nu_B > 0$ to create an NPN configuration with two PN junctions in series (fig. A.5). When we measure the two-terminal conductance at $B = 8$ T as a function of ν_T and ν_B (Fig. 3.6C and fig. A.5), we recognize the regions corresponding to zero, one, and two pairs of same-spin edge channels mediating transport across the PN junctions, as discussed above for the measurement in Fig. 3.3C and further analyzed in section A.4. In addition, we observe clear conductance oscillations, of which we expect the frequencies to reflect the gate lengths. To analyze these frequencies, we focus on the limit $|\nu_{B,T}| >> 1$ in which the edge-channel separation and the associated Aharanov-Bohm flux are

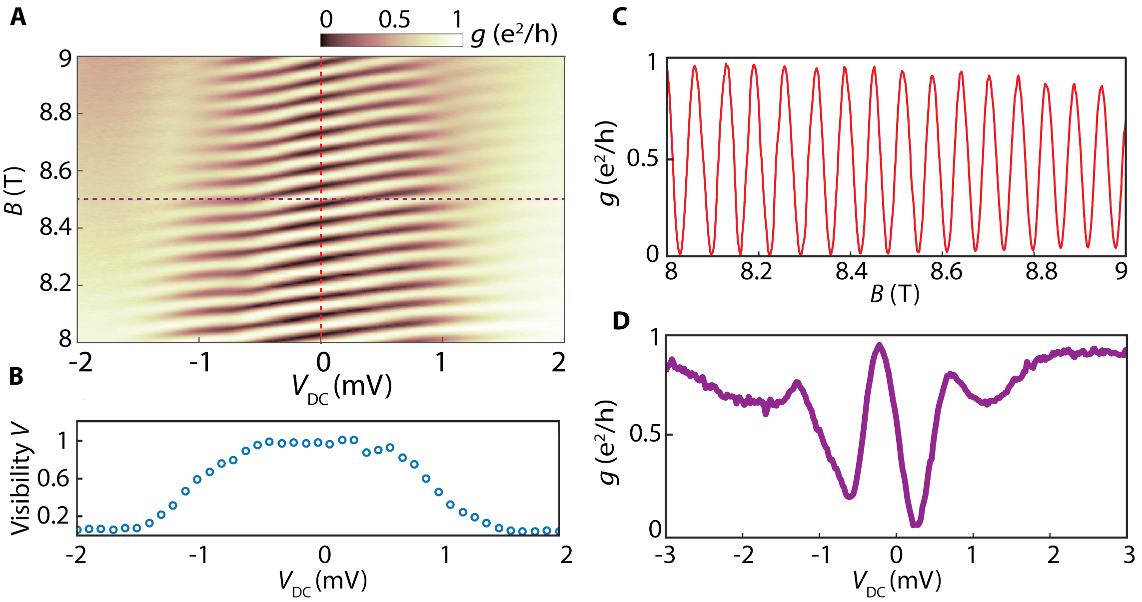

Figure 3.5: **Mach-Zehnder oscillations as a function of magnetic field and DC voltage bias.** **(A)** Two-terminal differential conductance as a function of magnetic field B and DC voltage bias V_{DC} at (ν_{B},ν_{T})=(1,-2), for which only one interferometer is formed at the PN interface. **(B)** Visibility of the conductance oscillations shown in a as a function of DC bias.**(C)** Conductance oscillations with B at zero DC bias corresponding to the red dotted line in (A). From the period $\Delta B = 66$ mT we calculate the distance between edge states to be 52 nm, assuming that the distance between the beamsplitters is given by the 1.2 μm width of the device. **(D)** Line trace corresponding to the purple dotted line in (A) showing oscillations with respect to V_{DC}.

expected to vary as $\sim 1/(\sqrt{\nu_B}+\sqrt{-\nu_T})$ (section A.5). We plot the conductance data against $1/(\sqrt{\nu_B}+\sqrt{-\nu_T})$ and use a Fourier transform to determine the frequency spectrum (Supplementary fig. A.6). Normalizing the frequency axis to the average length of TG5, we find peaks at locations that correspond reasonably well to those expected based on the lengths of the different gates (Fig. 3.6D). We conclude that the beamsplitters are located where the PN interfaces meet the physical graphene edge. Remarkably, it follows that each oscillation corresponds to a minute change in the edge-channel separation: for example, for the L=1.2 μm gate length of device 1, this change equals $\frac{\Phi_0}{BL} = 3.7$ Å.

3.2.5 Edge-channel equilibration along gate-defined and physical edges

Finally, we demonstrate the absence of inter-channel scattering along a gate-defined edge and the full equilibration of same-spin edge channels running along a physical edge. We use device 3 (Fig. 3.7A-D), which has two top gates that determine the number of edge channels running from the left to the right lead, and a top gate (referred to as the side gate) that determines which fraction of the edge channels in the central region travel along the lower physical edge instead of along the side-gate-defined edge. We first confirm the presence of robust broken-symmetry quantum Hall states (fig. A.7C). We then apply a bias V_{IN} between the left and top lead, and measure the potential at the right lead (V_{OUT}) as a function of the side-gate filling factor (Fig. 3.7E). Edge-channel equilibration in the central region should reduce the chemical potential at the right lead below that of the input lead. The precise match between data and model (described in section A.6) in Fig. 3.7E clearly demonstrates that edge channels do not equilibrate along the side-gate-defined edge, while they do equilibrate along the physical edge provided they have the same spin [31]. We note that we observe no MZI oscillations as we sweep the magnetic field between 8.9 and 9 T (fig. A.7D-F), presumably because there are no locations acting as beamsplitters as the edge channels do not meet at a physical edge before and after co-propagating along a gate-defined edge.

3.3 Discussion and future directions

The experiments presented here demonstrate a robust method of engineering a high-visibility MZI in a graphene quantum Hall system by harnessing edge channels copropagating along a pn junction. Although previous measurements on graphene pn junctions in the quantum Hall regime showed results ranging from full equilibration between edge channels co-propagating along the pn junction(with no noticeable interference effects) [58] to a complete absence of transpn junction conductance [31], we believe we observe interference between the copropagating channels belonging to the zLL because we have (i) a low-disorder device in which the Landau level degeneracy is fully lifted and in which dephasing is sufficiently low and (ii) we use a top gate that is relatively close to the graphene [closer than the top gate used in the study of Amet *et al.* [31]] so that the electrical potential profile across the pn junction is sharp and allows the edge states to come close enough to each other to be coupled and form beamsplitters. This opens up the possibility of a variety of interferometry experiments and grants us the diagnostic capabilities of measuring sub-nanometer shifts in edge-channel separation. In our experiments we observe transport across the insulating $\nu = 0$ state, which is expected to be in a canted antiferromagnetic (CAF) phase in bulk graphene [22, 25]. The fact that we find that spin polarization is well preserved in our samples suggests that the CAF phase may be suppressed in a narrow PN junction in favor of a state where spins are fully polarized along the direction of the magnetic field.

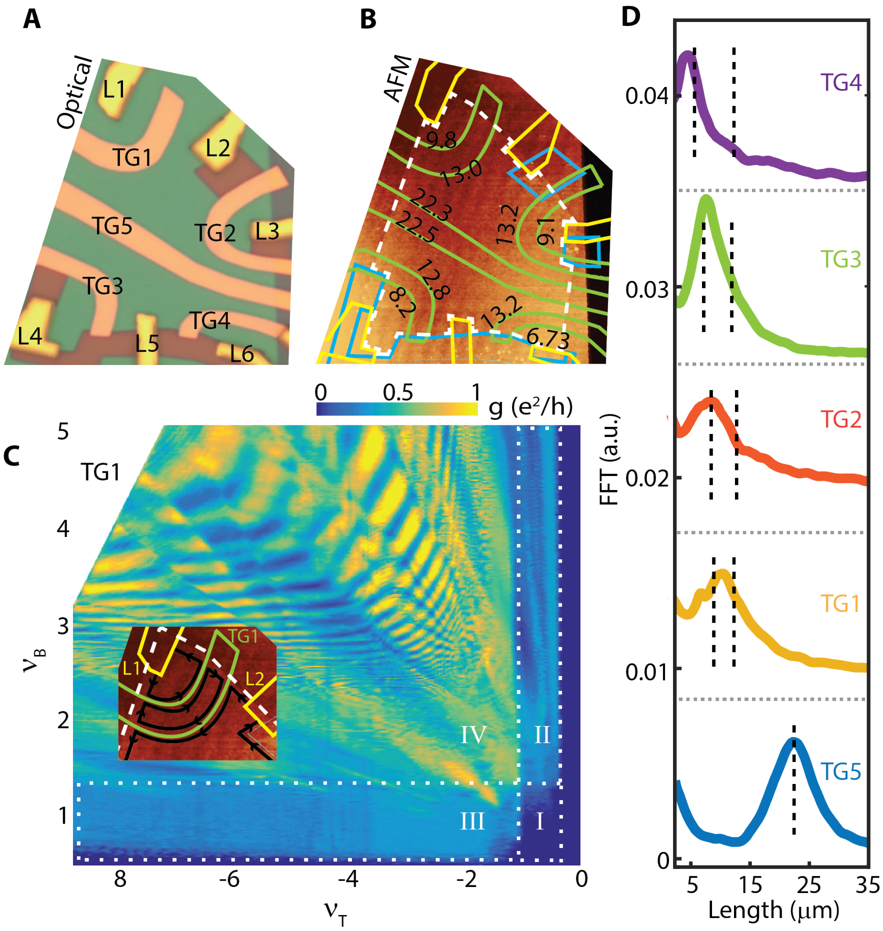

Figure 3.6: **Gate-length dependence of the Mach-Zehnder oscillations. (A)** Optical microscope image of device 2: an edge-contacted, hBN-encapsulated monolayer of graphene with five top gates of different lengths. The top-gate dielectric (hBN) is 17 nm thick. The bottom hBN layer is 16 nm thick. The back-gate dielectric (SiO_2) is 285 nm thick. Leads (L1-L6) are yellow. Top gates (TG1-TG5) are orange. Using a top and back gate, we induce an NPN charge configuration with two PN junctions and their associated MZIs connected in series. **(B)** AFM image of device 2. The graphene is indicated by the dashed white line.

Figure 3.6: (Continued) Top gates are outlined in green, leads in yellow, etched regions in blue. The lengths of both sides of each top gate are indicated in micrometers. **(C)** Two-terminal conductance measured across top gate 1 (TG1) using leads L1 and L2 at B = 8 T. Region I corresponds to (ν_{B}, ν_{T}) = (-1,1). Region II corresponds to ν_{T} = -1 and $\nu_{\mathrm{B}} \geq 2$. Region III corresponds to $\nu_{\mathrm{T}} \leq -2$ and $\nu_{\mathrm{B}} = 1$. Region IV corresponds to $\nu_{\mathrm{B}} \geq 2$ and $\nu_{\mathrm{T}} \leq -2$. Inset: close-up of (B) showing the top gate and the two leads used in this measurement. The edge channels are indicated by black lines. **(D)** Frequency spectrum (FFT, Fast Fourier Transform) of the conductance oscillations for all top gates. The x-axis is normalized to the length of TG5. The expected frequencies for each gate are indicated by the black dashed lines.

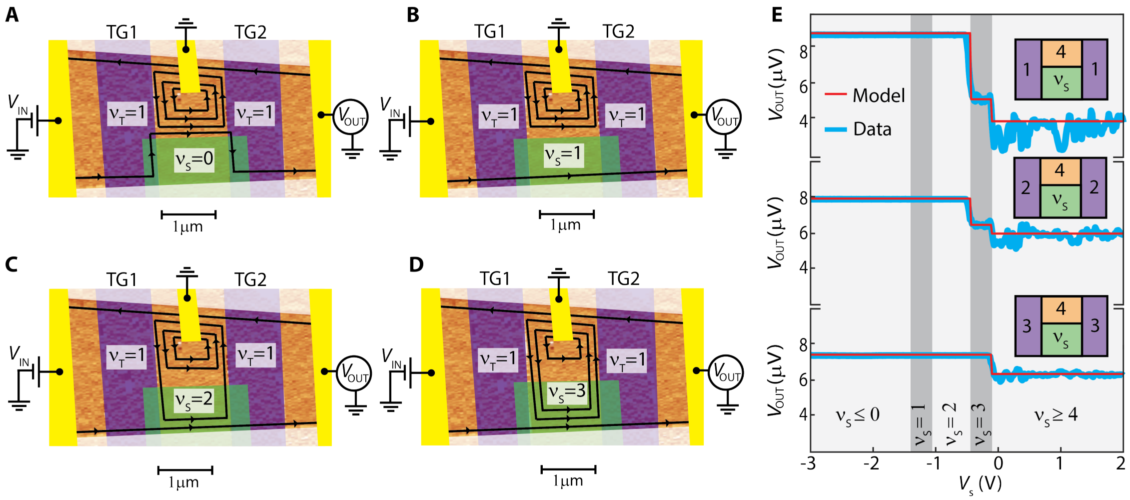

Figure 3.7: **Absence of equilibration between edge channels running along a gate-defined edge.** **(A-D)** Schematic of device 3: an edge-contacted, hBN-encapsulated monolayer of graphene with two top gates and a side gate. An AFM image shows the top gates (TG1 and TG2, false-colored purple) on top of the hBN-encapsulated graphene flake. Yellow (green) indicates the leads (side gate). The progression of panels (A-D) illustrates the changing locations of the edge channels in the central region as the filling factor under the side gate is tuned from ν_S = 0 to ν_S = 3, while the regions under TG1 and TG2 are kept at ν_T = 1 and the rest of the device is kept at ν_B = 4. The circulating edge states near the contacts are omitted for clarity. **(E)** Voltage measured at the right contact as a function of the side-gate voltage V_S that tunes the side-gate filling factor ν_S, for ν_T = 1, ν_T = 2, and ν_T = 3 as indicated by the insets. The data (blue) is an average of a set of traces taken at different magnetic fields between 7.9 and 8 T (Supplementary fig. A.7).

Figure 3.7: (Continued) The red line indicates the expected values given by a model that assumes no equilibration along the gate-defined edge and full equilibration between same-spin channels along the physical edge, taking into account the independently measured contact resistances (Supplementary Note 5). The top trace corresponds to the sequence depicted in (A-D).

Chapter 4

Electrical generation and detection of spin waves in a quantum Hall ferromagnet

4.1 Introduction

4.1.1 Spin waves

Just like electrical currents are an illuminating tool to examine semiconductors and metals, spin waves can tell us a great deal about magnetic systems. They can give us information about the magnetic ordering of the ground state, as well as possible magnetic excitations. There is also the possibility of studying magnetic analogues to electrical phenomena such as superconductivity (spin superfluidity [72]), a magnonic quantum Hall effect [73], or ballistic transport (ballistic magnons). Additionally, spintronics has emerged as an increasingly promising platform for more efficient information technology [74].

Spin waves are the elementary excitations of a ferromagnet, and magnons which are quantized spin waves [75, 76]. In a ferromagnetic material we can view each atomic site as having an electron spin that can be aligned to the rest if the temperature is below a value specific to the ferromagnet called the Curie temperature. We can think of the spin of each atom as a local magnetic moment, and if one of the spins is perturbed a small amount, it will create a small magnetic field that in turn perturbs neighboring magnetic moments, as shown in Figure 4.1.

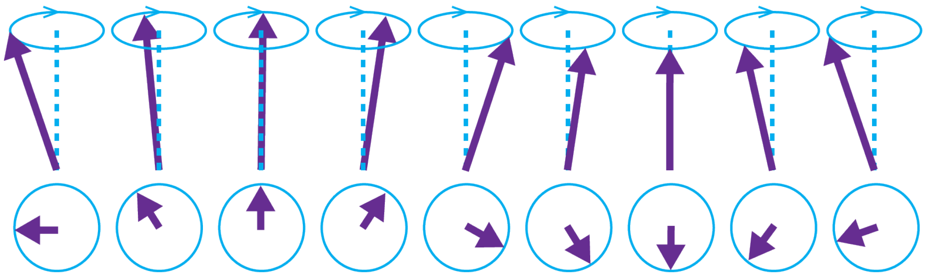

Figure 4.1: **A magnon represented by a chain of spins that are slightly perturbed from equilibrium.** Adapted from [76]. The lower part of the figure shows the direction of the spin projected onto a 2D plane, depicting how the spin processes around a circle.

A spin-wave is just a wave of these deflected spins propagating through the crystal. Each spin will precess around the direction of the external magnetic (B) field with a certain frequency, eventually dissipating into the lattice as heat. This characteristic frequency is typically in the GHz range and can consequently be probed by microwave techniques [77, 78]. Optical techniques have also been used to detect magnons in various systems [79, 80].

However, in order to integrate spintronics into our current information processing systems, it is necessary to be able to generate and detect spin via electrical methods. Additionally, this opens up the ability to conduct measurements in extreme conditions such as low temperature and high magnetic field. A good review on the topic can be found in [74]. The general idea is to couple a metal with large spin orbit coupling to a magnetic material. By flowing a large current through the metal, it will cause a large spin imbalance to be created via a mechanism called the spin Hall Effect [81]. This causes a spin wave to flow through the magnetic material, which can be detected in a distant metal interface via an inverse process called the inverse spin Hall effect. One particularly attractive version of this is the electrical generation and detection of spin waves in a magnetic insulator such as YIG [82, 83, 74, 84], because it avoids heating associated with conduction elections.

4.1.2 Spin waves in a quantum Hall ferromagnet

As described in section 2.3, the quantum Hall ferromagnet is a result of electron-electron interactions in the quantum Hall regime. Due to the large degeneracy of a Landau level there is a negligible kinetic energy penalty for spins to polarize and the system can become 100% ferromagnetic in the absence of disorder [3]. One can consider the QH ferromagnet as an itinerant magnet because the electrons are free to move around as in a metal, and derive a spin wave dispersion, as is done by Girvin in [3] (See Fig. 4.2). We can see that the lowest energy of a magnon in the system is $E_Z = g\mu_B B$, the Zeeman energy [85], where g is the electron g-factor, μ_B is the Bohr magneton, and B is the external magnetic field. We can also understand this intuitively by recognizing that the magnetization of the QH ferromagnet is extremely dilute, so there are negligible demagnetizing fields and the minimum energy to excite magnons would be the Zeeman energy [78].

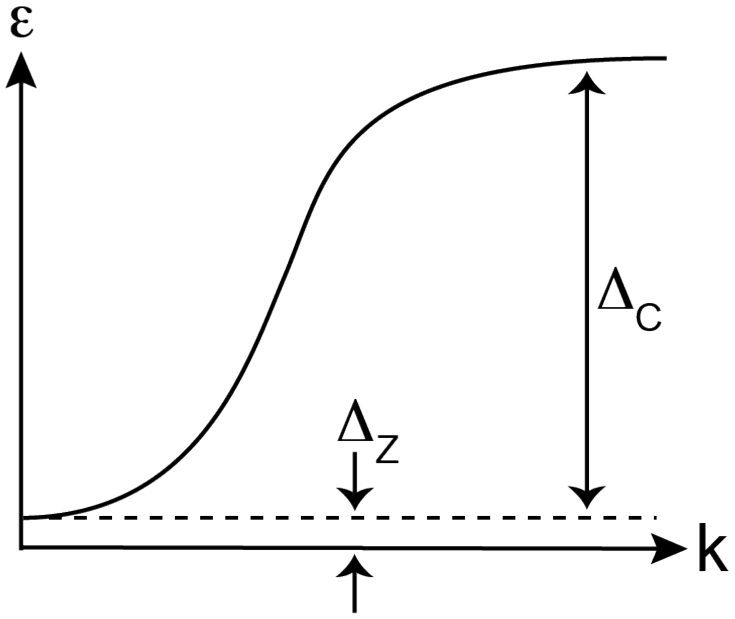

Figure 4.2: **Magnon dispersion in a quantum Hall ferromagnet.** Adapted from [3]. The minimum energy of a magnon in a QHF is the Zeeman energy Δ_Z. The energy saturates at the Coulomb exchange energy scale Δ_C.

In GaAs 2D systems, the lowest energy charged excitation arises in the form of a Skyrmion, or a topological spin texture of partially flipped spin in a vortex-like configuration [86], which has been seen in transport [87, 88], optical measurements [89, 90] and NMR [91, 92, 93]. These skyrmions have also been seen in transport experiments done in graphene [23]. There have also been measurements of the $\nu = 1$ spin wave in GaAs using inelastic light scattering experiments [90], which also indicated the formation of a gapless spin wave away from $\nu = 1$. However, previous to the work done in this thesis, there were no transport experiments examining magnons in the $\nu = 1$ ferromagnet due to their chargeless nature.

4.1.3 Bose Einstein condensate of magnons

Magnons have a spin of 1 and are therefore able to undergo Bose-Einstein condensation. Experimentally, this has been used to explain spin relaxation and dynamics in ^{3}He systems [94, 95, 96], and has also been observed in several magnetic insulators [97, 98, 99, 100, 101]. A good discussion of spin superfluidity can be found in [102]. In these systems it is possible that a supercurrent of spin, defined as a dissipationless transport of spin, can propagate [103]. A number of theoretical proposals have suggested that it might be possible to generate such as spin supercurrent using an electrical generation scheme, similar to those described in section 4.1.1 [104, 105, 106, 107, 108]. The proposal that began our interest in studying magnons was one by Takei in 2016 that suggested that the canted antiferromagnet phase in the $\nu = 0$ quantum Hall regime of graphene would be able to host a spin superfluid [109].

4.1.4 Summary of our experimental findings

In our experimental setup, we generate magnons by creating an imbalance of chemical potential between two edge states of opposite spin that run along the boundary of a QH magnet. If this imbalance is smaller than the energy required for generating magnons in the QH magnet (and there are no thermal magnons already present in the system), scattering between these two edge states is forbidden because the change in angular momentum of a scattered electron cannot be absorbed by the system. Indeed, previous measurements have shown that oppositely spin-polarized edge channels do not equilibrate as long as the imbalance is small [31, 110]. However, we find edge channel equilibration commences when the imbalance exceeds the minimum energy required for exciting magnons in the QH ferromagnet. Although magnon generation does not directly affect the conductance of the system, the reverse process of magnon absorption by far-away edge states does, allowing us to detect the propagation of magnons electrically, in close analogy to the conventional detection of magnons in insulators via the inverse spin Hall effect [82, 83, 74, 84]. Our experiments provide direct evidence for long-distance spin-wave propagation through the three-quarters-filled N=0 Landau level (LL), which is known to be ferromagnetic [23]. Additionally, we observe spin-wave propagation across a wide insulating strip tuned to half-filling, which is believed to be an insulating canted antiferromagnet (CAF) [22, 25]. Our results provide the first experimental evidence for spin-wave transport in QH magnets, opening a new arena of experimental investigation into the fundamental magnetic properties of these exotic two-dimensional electron systems.

4.2 Experimental Results

4.2.1 Demonstration of spin wave generation and propagation

To demonstrate spin wave propagation, we begin with a dual-gated monolayer graphene device (device 1) where the central region can be tuned to a different filling factor than the adjacent regions (Fig. 4.3A). Connecting the two leads is a chiral edge state that carries spin-polarized electrons aligned with the magnetic field, which we call spin-up. We tune the central region to a three-quarters-filled LL ($\nu = 1$), whereas the outer regions are tuned to a non-magnetic fully filled LL ($\nu = 2$). We apply a source-drain voltage V_{dc} to induce a difference in chemical potential $\mu = -eV_{\text{dc}}$ between the edge channels emerging from the two contacts, where e is the electron charge. Once $|\mu| \geq E_{\text{Z}}$, an electron traveling in a high-energy ("hot"), spin-down edge state can relax into a low-energy ("cold"), spin-up edge state by emitting a magnon into the ferromagnetic bulk (Fig. 4.3B-C). Because equilibration must occur close to the ferromagnetic bulk in order to launch magnons, the edge states must equilibrate over short length scales at localized "hot spots" where the hot and cold edges meet. This makes graphene an ideal platform to observe this phenomenon, where edge state equilibration can occur over length scales $< 1\mu$m [31, 58, 62] (See B.2 for further discussion). Because only spin-down angular momentum can be propagated into the spin-up bulk, magnon generation occurs at the location denoted by an encircled minus sign when $\mu \geq E_{\text{Z}}$ (Fig. 4.3B) and at the location denoted by an encircled plus sign when $\mu \leq -E_{\text{Z}}$ (Fig. 4.3C). These magnons propagate through the insulating QH ferromagnet and can be absorbed by the reverse process between other edge channels (Fig. 4.3B-C), which causes a deviation in the conductance from a well-quantized $\nu = 1$ QH state.

When we measure the conductance of the graphene device (Fig. 4.3E, atomic force microscopy image in fig. B.3) as a function of V_{dc}, we find that the $\nu = 1$ QH ferromagnet remains precisely quantized at the expected value of e^2/h, and then changes once the applied bias reaches the Zeeman threshold ($V_{\mathrm{dc}} = \pm V_{\mathrm{EZ}} = \mp E_{\mathrm{Z}}/e$), as expected from our model (Fig. 4.3F). Interestingly, we find that thanks to contact doping (see B.2 and [111]) we can tune the entire device to $\nu = 1$ and find the same phenomenon of conductance deviation at the Zeeman threshold (fig. B.4).

By tilting the external magnetic field with respect to the sample-plane normal axis, we verify that the change in conductance occurs when the applied chemical potential exceeds the bare Zeeman energy $E_{\mathrm{Z}} = g\mu_{\mathrm{B}}B_{\mathrm{T}}$ (g=2), which is given by the total field B_{T} (Fig. 4.3G – sample is tuned entirely to $\nu = 1$). In contrast, previous transport studies of spin and valley excitations in graphene and GaAs have only found excitations related to the exchange energy gap [23, 86, 87], which depends on the component of the field perpendicular to the sample plane ($B_{\perp}$). Our tilted-field measurements therefore corroborate our magnon-based interpretation of the observed change in sample conductance. All subsequent experiments described in this work are done at perpendicular field.

The conductance change at E_{Z} can either be positive or negative, depending on the number of magnons absorbed at each contact. To examine this, we use different sets of leads in the same device (Fig. 4.4A, device 2) to perform two-terminal conductance

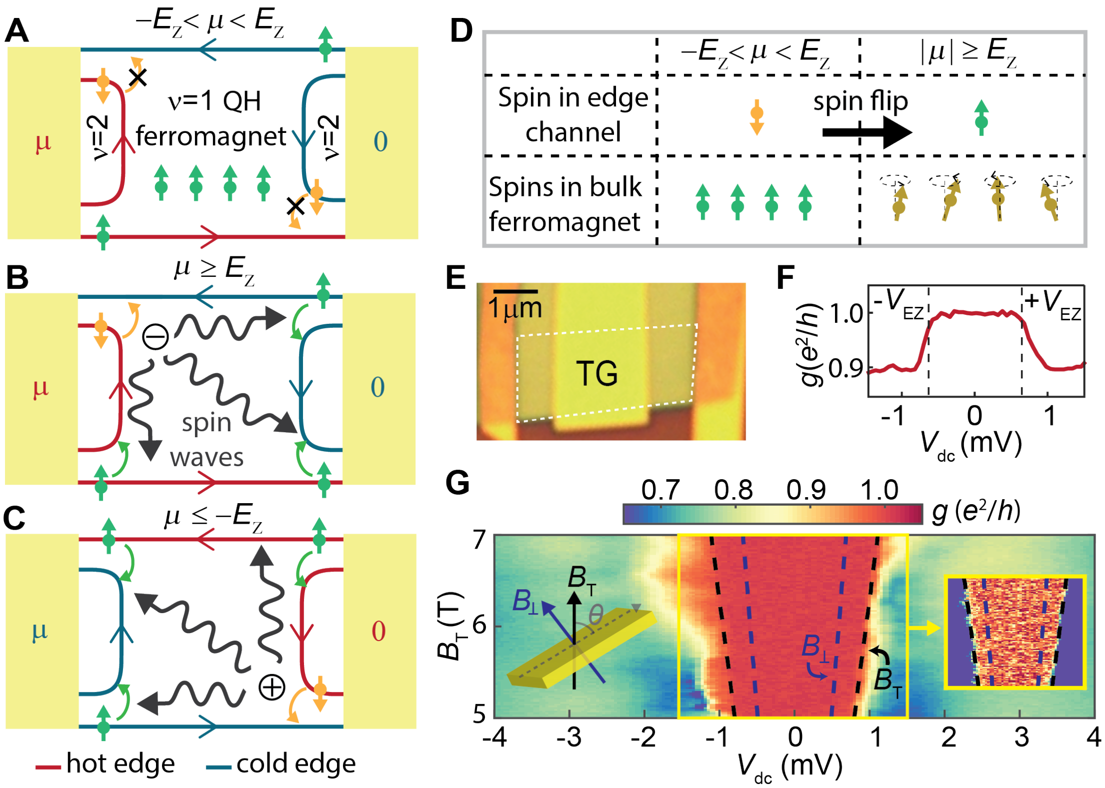

Figure 4.3: **Magnons in a quantum Hall ferromagnet.** **(A-C)** A chemical potential difference (μ) is applied between the left and right leads. Edge channels with high and low chemical potential are labeled “hot” and “cold”, respectively. Spin-up and spin-down polarization is denoted by the green and orange arrows, respectively. The central region is tuned to $\nu = 1$ and adjacent regions are tuned to $\nu = 2$. **(A)** The chemical potential difference (μ) between the spin-up and spin-down edge channel is less than the Zeeman energy (E_Z), and scattering is suppressed. **(B)** $\mu \geq E_Z$: Electrons have enough energy to flip their spins and transfer spin angular momentum (magnons) into the bulk (at the encircled minus sign). These magnons are absorbed at distant corners, causing electrons to flip from spin-up into spin-down channels.

Figure 4.3: (Continued) **(C)** $\mu \leq -E_{\mathrm{Z}}$: Magnons are generated at the location denoted by the encircled plus sign. **(D)** Bulk spin polarization before and after magnon creation, conserving total spin angular momentum. **(E)** Optical micrograph of device 1; graphene is outlined in white. TG, top gate. **(F)** A dc voltage (V_{dc}) and a 50-μV ac excitation voltage (V_{ac}) are applied to the left contact and the differential conductance ($\mathrm{d}I/\mathrm{d}V$, where $V = V_{\mathrm{ac}} + V_{\mathrm{dc}}$) is measured through the right contact ($B_{\mathrm{perp}} = 4$ T, $V_{TG} =$ -0.18 V, $V_{BG} = 3$ V). Conductance is quantized to e^2/h until $|\mu| \geq E_{\mathrm{Z}}$. **(G)** $\mathrm{d}I/\mathrm{d}V$ as a function of bias and magnetic field. The blue dashed line is the Zeeman energy, $E_{\mathrm{Z}\perp} = g\mu_B B_\perp$ calculated using the perpendicular (total) magnetic field $B_\perp$; The black dashed line is the Zeeman energy, $E_{\mathrm{ZT}} = g\mu_{\mathrm{B}} B_{\mathrm{T}}$ calculated using the total magnetic field B_{T}). Both the top gate (V_{TG}) and back gate (V_{BG}) are swept to stay at $nu = 1$ throughout the device from 7T ($V_{TG} = 0.16$ V, $V_{BG} = 0.73$ V) to 5T ($V_{TG} = 0.12$ V, $V_{BG} = 0.44$ V) The decrease in conductance from e^2/h evolves linearly with the magnetic field coinciding with E_{ZT} rather than $E_{\mathrm{Z}\perp}$. Right inset: A saturated color plot (from 0.98 to 1.02 e^2/h) of the region enclosed by the yellow box. All measurement are conducted in a cryostat with a base temperature of 20 mK.

measurements. We start with leads L_2 and L_1 in Fig. 4.4B. We label the amount of redistributed chemical potential at each of the absorption sites ε_i, with i indexing the absorption site (note that $\varepsilon_i = 0$ for $-E_\mathrm{Z} < \mu < +E_\mathrm{Z}$), where ε_i is proportional to the number of magnons absorbed at site i. Absorption at ε_1 and ε_2 have opposite effects on the conductance, as magnon absorption transfers chemical potential from the outer edge to the inner edge. Therefore, for $\mu \geq E_\mathrm{Z}$, magnon absorption at ε_1 decreases the particle current ($I_\mathrm{P} = -I/e$ where I is the charge current) whereas magnon absorption at ε_2 increases I_P (Fig. 4.4B). For $\mu \leq -E_\mathrm{Z}$, the hot and cold reservoirs are reversed, and we now consider the change to the negative particle current $-I_\mathrm{P}$. Although ε_1 still decreases the particle current, I_P is now negative, and so ε_1 actually increases the magnitude of the particle current ($|-I_\mathrm{P}|$); similarly, for $\mu \leq -E_\mathrm{Z}$, ε_2 decreases $|-I_\mathrm{P}|$ (Fig. 4.4C). We can quantify this using current conservation to formulate the differential conductance as a function of ε_i and μ:

$$\frac{\mathrm{d}I}{\mathrm{d}V} = \frac{\mathrm{d}I_\mathrm{P}}{\mathrm{d}\mu} = \frac{1}{R_\mathrm{Q}}\Big(1 + \frac{\mathrm{d}\varepsilon_2}{\mathrm{d}\mu} - \frac{\mathrm{d}\varepsilon_1}{\mathrm{d}\mu}\Big) \tag{4.1}$$

where $R_\mathrm{Q} = h/e^2$ is the resistance quantum, $V = V_\mathrm{ac} + V_\mathrm{dc}$, and we have neglected contact resistance (see B.4 for a derivation of Eq. 4.1, which takes contact resistance into account). We find that the conductance decreases at negative bias and increases at positive bias (Fig. 4.4D) – indicating that $\varepsilon_1 > \varepsilon_2$ for both positive and negative bias. This implies that more magnons are absorbed at ε_1 than at ε_2. Because our contacts have all been fabricated identically, we conclude this is because ε_1 is closer to magnon generation than ε_2 (for both positive and negative bias, see Fig. 4.4A-B). Using different sets of contacts and top gates (Fig. 4.4E-H) we can change the relative distances of ε_i to the locations of magnon generation. We confirm that for each configuration, the conductance values after E_{Z} correspond to a greater number of magnons absorbed at the site closer to magnon generation.

This change to the conductance is not a consequence of QH breakdown. Conductance deviations after the Zeeman threshold that depend on the sign of V_{dc} are not explained by any current breakdown theories [112]. Additionally, we find that the threshold voltage bias does not depend on the lead configuration (Fig. 4.4), the size of the $\nu = 1$ region (fig. B.4), or the density of the $\nu = 1$ region (fig. B.6) – which is all inconsistent with trivial QH breakdown, but consistent with our magnon model. In total, we have measured this $\nu = 1$ conductance deviation occurring at the Zeeman energy for eight devices of widely varying geometries (figs. B.3, B.4, and B.11).

4.2.2 Non-local measurements

Thus far we have established that we are able to generate and absorb magnons at current carrying contacts. If these chargeless excitations propagate through the insulating bulk, we also expect to see signatures of magnon propagation and absorption via non-local voltage measurements ($\mathrm{d}V_{\mathrm{NL}}/\mathrm{d}V$referred to as nonlocal signal S_{NL}), away from the source-drain current. To measure S_{NL} we use L_3 and L_2 in device 2 as source-drain contacts, and use contacts L_4 and L_5 as voltage probes (Fig. 4.5A). These contacts are separated from the source-drain contacts by a top gate (TG2) which we tune between ν_{TG2} = -2 and ν_{TG2} = 2, where all other regions are tuned to $\nu = 1$. The conductance between L_3 and L_2 drops at V_{EZ} in accordance with our model (Fig. 4.5B), whereas magnon generation is largely unaffected by TG2 (fig. B.7A). At

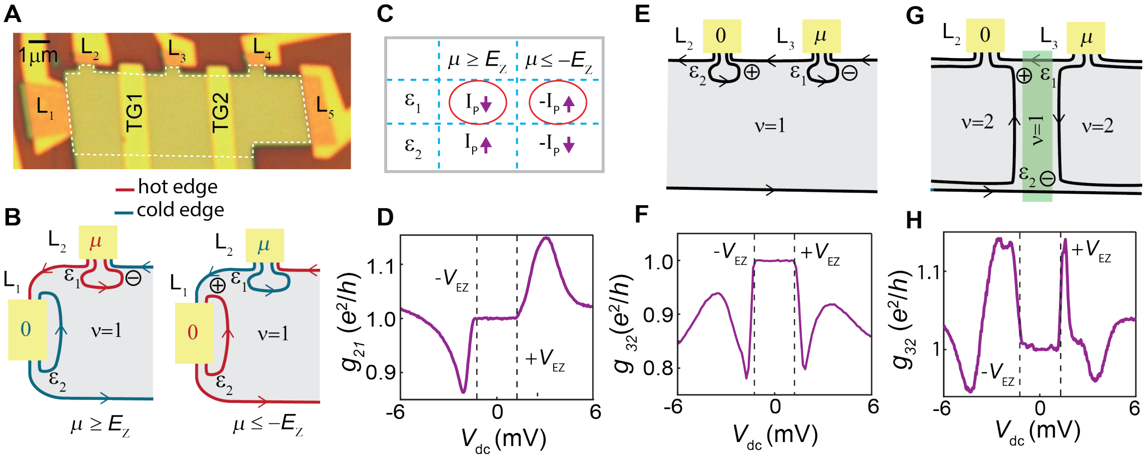

Figure 4.4: **Effect of relative magnon absorption on conductance.** **(A)** Optical micrograph of device 2. Graphene is outlined in white. **(B)** Schematic of a two-terminal conductance measurement using leads L_2 and L_1 where hot and cold edges are colored red and blue, respectively, for both $\mu \geq E_\mathrm{Z}$ (left) and $\mu \leq -E_\mathrm{Z}$ (right), and the magnon generation site is labeled by the encircled plus or minus sign indicating positive or negative bias. $\mu \geq E_\mathrm{Z}$: magnon absorption at ε_1 transfers chemical potential from a forward-moving edge to a backward-moving edge, causing the particle current ($I_\mathrm{P} = -I/e$) to decrease. Conversely, magnon absorption at ε_2 transfers chemical potential from a backward-moving edge to a forward-moving edge, increasing I_P. $\mu \leq -E_\mathrm{Z}$: Magnon absorption at ε_1 causes an increase in $|-I_\mathrm{P}|$; absorption at ε_2 causes a decrease in $|-I_\mathrm{P}|$. **(C)** The effects of ε_1 and ε_2 at $\mu \geq E_\mathrm{Z}$ and $\mu \leq -E_\mathrm{Z}$. The current changes caused by ε_1 are dominant and are circled in red. The purple arrows indicate an increase (up) or decrease (down) in the magnitude of the signed particle current.**(D)** Conductance from L_2 to L_1 ($g_{21} = \mathrm{d}I/\mathrm{d}V = \mathrm{d}I_\mathrm{P}/\mathrm{d}\mu$) decreases at $V_\mathrm{dc} = -V_\mathrm{EZ}$ and increases at $V_\mathrm{dc} = V_\mathrm{EZ}$, indicating that ε_1 has a larger effect than ε_2 (B = 8 T, V_{BG} = 4 V). See Appendix B for full circuit analysis.

Figure 4.4: (Continued) **(E-F)** Conductance from L_3 and L_2 (g_{32}) where the entire device is tuned to $\nu = 1$ ($V_{BG} = 4$V, TG1 $= 0$V is not shown). At positive bias, $\varepsilon_2 > \varepsilon_1$, and at negative bias, $\varepsilon_1 > \varepsilon_2$, resulting in a conductance drop for both biases.**(G-H)** Conductance from L_3 to L_2 (g_{32}) where TG1 is tuned to $\nu_{\mathrm{TG1}} = 1$ (TG1=-0.36 V) while the regions outside are set to $\nu_{\mathrm{bg}} = 2$ ($V_{BG} = 6.5$V). At positive bias, $\varepsilon_1 > \varepsilon_2$, and at negative bias, $\varepsilon_2 > \varepsilon_1$, resulting in a conductance rise for both biases. See fig. B.5. for a detailed analysis.

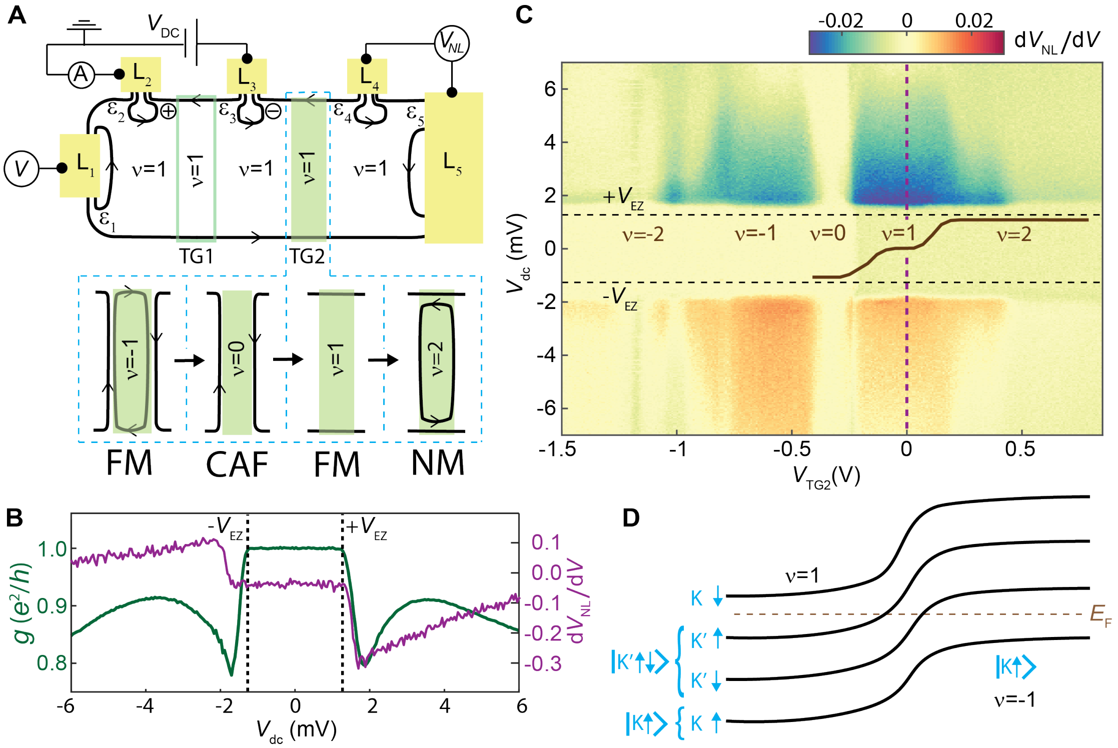

Figure 4.5: **Non-local voltage signal due to magnon absorption.** Shown are the data from device 2. **(A)** Schematic circuit configuration for measuring a non-local voltage in device 2. The filling factor under TG1 (ν_{TG1}) = 1 for all measurements while the filling factor under TG2 (ν_{TG2}) is swept from -2 to 2, and the rest of the device is kept at $\nu_{\mathrm{bg}} = 1$ ($V_{BG} = 4$ V). The bottom panel highlights the magnetic properties of different cases of ν_{TG2}: non-magnetic (NM), ferromagnetic (FM), or canted antiferromagnetic (CAF). **(B)** S_{NL} (purple) superimposed onto $\mathrm{d}I/\mathrm{d}V$ (green) as a function of V_{dc} when $\nu_{\mathrm{TG2}} = 1$ ($B = 8$ T). The onset of S_{NL} is slightly offset in bias from the decrease in conductance, indicating that magnon generation needs to reach a threshold before being absorbed in distant contacts. **(C)** A pronounced S_{NL} signal when $\nu_{\mathrm{TG2}} = 1$ and $\nu_{\mathrm{TG2}} =$ -1 (See Fig. S8 for similar measurements using TG1).

Figure 4.5: (Continued) Tuning TG2 to the nonmagnetic QH phases ($\nu_{\mathrm{TG2}} = 2$ and $\nu_{\mathrm{TG2}} = -2$), as well the $\nu_{\mathrm{TG2}} = 0$ CAF state, strongly suppresses S_{NL}. There is a small finite background S_{NL} when edge states pass through TG2, discussed in fig. S7, B. Solid brown line indicates where $\nu_{\mathrm{TG2}} = 0$, 1, and 2 (fig. S7, C and D). **(D)** The spatial variation of the LLs at a $\nu = 1/\nu = -1$ junction, with the expected valley and spin polarizations of each level labeled.

$\nu_{\mathrm{TG2}} = 1$ we measure a change in S_{NL} at $\pm V_{\mathrm{EZ}}$ due to the relative absorption at each magnon absorption site (ε_i).

The sign of S_{NL} indicates that there is more magnon absorption at sites closer to where magnon generation occurs. Through current conservation (B.5) we find that the measured differential voltage (unitless) is:

$$\frac{\mathrm{d}V_{\mathrm{NL}}}{\mathrm{d}V} = \left(\frac{\mathrm{d}\varepsilon_4}{\mathrm{d}\mu} - \frac{\mathrm{d}\varepsilon_5}{\mathrm{d}\mu}\right) \tag{4.2}$$

The site labeled by ε_4 is closer to magnon generation than ε_5 for both negative and positive bias, so $|\mathrm{d}\varepsilon_4| > |\mathrm{d}\varepsilon_5|$. However, the differential change in voltage ($\mathrm{d}\varepsilon_i/\mathrm{d}\mu$) is negative for $V_{\mathrm{dc}} \geq V_{\mathrm{EZ}}$ and positive for $V_{\mathrm{dc}} \leq -V_{\mathrm{EZ}}$, corresponding to an overall negative value for S_{NL} at $V_{\mathrm{dc}} \geq V_{\mathrm{EZ}}$ and a positive value at $V_{\mathrm{dc}} \leq -V_{\mathrm{EZ}}$ (Fig. 4.5C).

The device geometry used for our non-local measurements allows us to tune TG2 away from $\nu_{\mathrm{TG2}} = 1$, and thereby examine magnon transmission through different filling factors. We make two surprising observations. We observe that when $\nu_{\mathrm{TG2}} = -1$ the signal s_{NL} is almost identical signal to when $\nu_{\mathrm{TG2}} = 1$ (Fig. 4.5C and fig. B.8). This signal arises in the absence of any charge leakage across the $\nu_{\mathrm{TG2}} = -1$ region (fig. B.9), so that changes in S_{NL} can be attributed to magnon transport through the $\nu_{\mathrm{TG2}} = -1$ ferromagnet. This suggest that there is neither spin nor valley mismatch between the ferromagnetic states on either side of the boundary. We therefor propose an ordering of the LLs that does not require a spin or valley flip for magnons to travel across the interface between $\nu_{\mathrm{BG}} = 1$ and $\nu_{\mathrm{TG2}} = -1$ (Fig. 4.5D; see B.6 for a theoretical discussion.)

4.2.3 Magnetic signals through the $\nu = 0$ canted antiferromagnet

In addition, we unexpectedly find that S_{NL} is suppressed at $\pm V_{\mathrm{EZ}}$ when $\nu_{\mathrm{TG2}} = 0$. For non-magnetic regions such as $\nu_{\mathrm{TG2}} = 2$, it is expected that magnons will be blocked from passing through, as experimentally confirmed in Fig. 4.5C (the non-local signal occurring at the transition between $\nu = 1$ and $\nu = 2$ is explained in Fig. B.7E). However, $\nu = 0$ is purportedly a canted antiferromagnet which is theoretically capable of hosting even zero-energy magnons [109]. It appears that the probability for an incident magnon to be transmitted across the junction between the $\nu = 0$ and $\nu = 1$ regions is very small for energies close to E_{Z}. This may be caused by, in part, the mismatch in propagation velocities in the two phases, or a barrier due to the complex nature of the interface region. Close to the boundary with a $\nu = 1$ phase, the ground state of the $\nu = 0$ phase may not have canted spins but may instead be in an aligned antiferromagnet state, where spins are parallel to the magnetic field on one sublattice and antiparallel on the other. Eventually, far from the boundary, we may expect the local spin arrangement to rotate into the CAF orientation (Fig. 4.6B). In the transition region, the minimum magnon energy will be larger than E_{Z} due to effects of the valley-dependent interaction terms [22], which were initially responsible for the antiferromagnet arrangement to be favored over the ferromagnetic arrangement. In order to cross from the $\nu = 1$ region to the CAF region, a magnon with energy close to E_{Z} would have to tunnel through the barrier region, and we would expect the transmission rate to be low. If the magnons have enough energy to overcome this barrier, they should be able to more easily enter the CAF region. Fig. 4.6C shows that

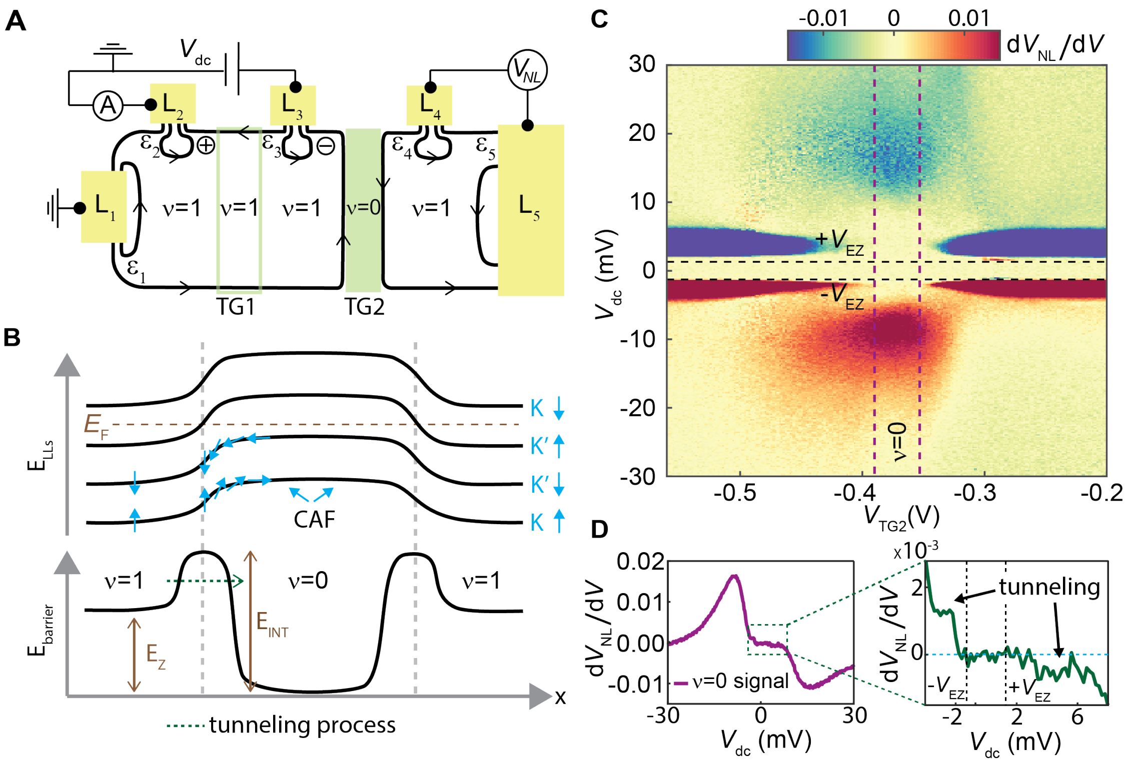

Figure 4.6: **Non-local voltage signal due to magnon propagation through the $\nu = 0$ CAF. (A)** Schematic of the circuit used to measure S_{NL} in device 2 across a $\nu = 0$ region. $\nu_{\text{TG1}} = 1$ for all measurements while ν_{TG2} is swept from -1 to 1 ($\nu_{BG} = 1$, $V_{BG} = 4$ V). **(B)** Top: Postulated spatial variation of the LLs and spin arrangement in a $\nu = 1/\nu = 0/\nu = 1$ geometry. Close to the interface between $\nu = 1$ and $\nu = 0$, spins in the two filled Landau levels prefer to be in an aligned antiferromagnetic (AF) arrangement. Deeper into the $\nu = 0$ region, the spins slowly rotate into the canted antiferromagnetic phase. Because the minimum magnon energy in the aligned AF region is higher than E_{Z}, it should present a barrier for incident magnons close to the energy threshold. Bottom: Energy barrier seen by the magnons as a function of position, where E_{INT} is the energy barrier of the interface.

Figure 4.6: (Continued) **(C)** When magnons are generated, we see another onset of S_{NL} at energies exceeding $\pm V_{\mathrm{EZ}}$ ($B = 8$ T), indicating that higher energy magnons have overcome E_{INT} and have propagated through the $\nu_{\mathrm{TG2}} = 0$ region. Purple dashed lines indicate a region where vertical line cuts were taken and averaged to obtain the line trace in (D). **(D)** A clear onset of S_{NL} is shown at biases exceeding $\pm V_{\mathrm{EZ}}$ when $\nu_{\mathrm{TG2}} = 0$. It is not presently understood why the signal is asymmetric both in energy of onset and strength of signal. The zoomed-in region shows a clear increase in S_{NL} at -V_{EZ} and a signal consistent with a decrease, slightly offset from $+V_{\mathrm{EZ}}$, indicating that magnons can tunnel through the interface barrier at lower energies (S_{NL} is offset by 0.01 μV at $V_{dc} = 0$ and is manually corrected for).

we can experimentally exceed this barrier, where we see non-local signals at higher $|V_{\mathrm{dc}}|$ with signs in agreement with our magnon model. The onset of this magnon signal is unaffected by any charge transport across the $\nu_{\mathrm{TG2}} = 0$ region (fig. B.10). Closely examining the signal at $\nu_{\mathrm{TG2}} = 0$, we see signals commencing at $\pm V_{\mathrm{EZ}}$ which we attribute to tunneling events across this $\nu_{\mathrm{BG}} = 1/\nu_{\mathrm{TG2}} = 0$ barrier (Fig. 4.6D).

Note that all non-local signals (occurring at ν_{TG2} =-1, 0, and 1) appear only in a finite band of V_{dc}. This suppression of the differential voltage signal indicates that either magnon generation is suppressed, or alternatively, that the differently-spaced contacts begin to see identical amounts of magnon absorption once the system has reached a certain magnon density threshold. We further speculate that this cut-off could be related to the magnon bandwidth, but leave this to a future investigation.

4.3 Discussion and future directions

The experiments presented here introduce a method of using magnons to probe the SU(4) spin and valley anisotropies of graphene QH systems, whichc can be used to probe highly correlated states such as the fractional QH regime [113], or the quantum-spin Hall phase of monolayer graphene [25]. Owing to the theoretical prediction for spin superfluidity in the CAF state [109], this study paves the way for exploring and realizing dissipationless spin waves in a Bose-Einstein condensate (BEC) of magnons. Such condensates should result in a coherent precession of the spin in the QH magnet, which may be probed through emitted microwave radiation. Furthermore, coherent spin waves associated with a BEC may be able to propagate long distances with negligible dissipation, which could be tested by careful length dependence measurements.

Appendix A

Additional information for Mach-Zehnder interferometry experiments

A.1 Methods

A.1.1 Sample fabrication

All devices were fabricated on doped Si chips with a 285 nm layer of SiO_2 that acted as a dielectric for the Si back gate. Graphene was mechanically exfoliated from bulk graphite obtained from NGS Naturgraphit GmbH using 1009R tape from Ultron Systems and subsequently encapsulated in hexagonal boron nitride (hBN) using a dry transfer process [114]. For device 1, we placed the resulting stack on a graphite bottom gate. Before the first metal deposition step, we annealed the devices in vacuum at

500°C to improve device quality. We then created top gates using electron-beam lithography and thermal evaporation of Cr/Au. To fabricate edge-contacts to the graphene in device 1 without shorting to the graphite bottom gate, we selectively etched the stack down such that the bottom hBN flake remained and protected the graphite while simultaneously exposing the graphene flake. To fabricate edge-contacts to the graphene in devices 2 and 3, we etched through the entire hBN/graphene stack. We then created edge contacts by thermally evaporating Cr/Au while rotating the sample using a tilted rotation stage. Finally, we etched the devices into the desired geometry by reactive ion etching in O_2/CHF_3 using a PMMA/HSQ bilayer of resist (patterned by electron-beam lithography) as the etch mask.

A.1.2 Measurement

Our measurements were performed in a Leiden dry dilution refrigerator with a base temperature of 20 mK. Measurements of differential conductance were performed using a lock-in amplifier with an AC excitation voltage of 10 μV at 17.77 Hz. All measurements of differential conductance were corrected for contact/line resistances, which were independently determined by lining up the robust $\nu = 2$ quantum Hall conductance plateau with $2e^2/h$. We estimated all filling factors based on a parallel-plate capacitor model with a correction to account for quantum capacitance (Supplementary Note 6).

A.2 Modeling the distance between the edge channels forming an MZI

In this note we describe the model used for the calculations shown in Fig. reffig:F2E of the main text, which shows the conductance of a PN junction as a function of filling factors to the left and right of the PN junction, ν_{B} and ν_{T}, respectively. As discussed in the main text, we attribute the oscillations to a changing flux enclosed by the two edge channels forming a Mach-Zehnder interferometer. At fixed magnetic field, this change is caused by a change in distance between the edge channels. We analyze the locations of the two interferometer-forming edge channels by determining where the corresponding exchange-split Landau sublevels cross the Fermi energy, using a simple model for the spatial dependence of the sublevel energy described by

$$E_{\pm}(x) = \frac{\mu_{\mathrm{T}} - \mu_{\mathrm{B}}}{2} g(x) + \frac{\mu_{\mathrm{T}} + \mu_{\mathrm{B}}}{2} \pm \frac{U_{\mathrm{ex}}(x)}{2} \tag{A.1}$$

where $\mu_{\mathrm{B(T)}}$ is the chemical potential to the left (right) of the junction, $U_{\mathrm{ex}}(x)$ is the exchange splitting, and $g(x)$ is a function that smoothly changes from -1 to 1 across the PN junction over a distance W that is similar to the distance of the graphene to the gates. For simplicity, from now on we neglect the spatial dependence of U_{ex}.

To link the chemical potentials to filling factors, we note that in general $\mu = \int_0^{\nu} \frac{\delta\mu}{\delta\nu'} d\nu'$, which increases stepwise as Landau levels are filled. For simplicity, we make the approximation $\mu = \frac{E_C}{2}\mathrm{sgn}(\nu_{T,B})\sqrt{|\nu_{T,B}|}$, where $E_C = \sqrt{2e\hbar B v_F^2}$ and v_F is the Fermi velocity [7]. Defining $f_{\pm}(x) = \frac{4E_{\pm}(x)}{E_C}$, and limiting ourselves to the case of $\nu_{\mathrm{T}} < 0$ and $\nu_{\mathrm{B}} > 0$ relevant in our PN measurements, we get

$$f_{\pm}(x) = -(\sqrt{-\nu_{\mathrm{T}}} + \sqrt{\nu_{\mathrm{B}}})g(x) + \sqrt{\nu_{\mathrm{B}}} - \sqrt{-\nu_{\mathrm{T}}} \pm u_{\mathrm{ex}} \tag{A.2}$$

where we have defined $u_{\text{ex}} = \frac{2U_{\text{ex}}}{E_C}$. The location of an edge channel is then obtained by solving $f(x) = 0$, so that the distance between two edge channels is given by

$$\Delta_x = g^{-1}\left[\frac{\sqrt{\nu_{\text{B}}} - \sqrt{-\nu_{\text{T}}} + u_{\text{ex}}}{\sqrt{-\nu_{\text{T}}} + \sqrt{\nu_{\text{B}}}}\right] - g^{-1}\left[\frac{\sqrt{\nu_{\text{B}}} - \sqrt{-\nu_{\text{T}}} - u_{\text{ex}}}{\sqrt{-\nu_{\text{T}}} + \sqrt{\nu_{\text{B}}}}\right] \tag{A.3}$$

For $g(x)$ we use a logistic function of width W:

$$g(x) = \frac{2}{1 + e^{-\frac{X}{W}}} - 1. \tag{A.4}$$

This has the inverse

$$g^{-1}(y) = W\ln\left[\frac{1+y}{1-y}\right]. \tag{A.5}$$

Combining Eqns. A.3 and A.5, we find the distance between the two edge channels

$$\Delta_x = W\ln\left[\frac{\sqrt{\nu_{\text{B}}} + u_{\text{ex}}/2}{\sqrt{\nu_{\text{B}}} - u_{\text{ex}}/2}\frac{\sqrt{-\nu_{\text{T}}} + u_{\text{ex}}/2}{\sqrt{-\nu_{\text{T}}} - u_{\text{ex}}/2}\right] \tag{A.6}$$

To calculate the plot of Fig. 3.4E we now assume a MZ interferometer with 50/50 beam splitters and calculate the conductance using

$$g = 0.5 + 0.5\cos\left(2\pi\frac{BL\Delta_x}{\Phi_0}\right) \tag{A.7}$$

In Fig. 3.4E , we used $B = 9$T, $L = 1.2$ μm, $\Phi_0 = h/e$, W = 52 nm and, to qualitatively resemble the data, u_{ex}=0.4.

A.3 Scattering model for an MZI at a graphene PN junction

In this note we provide a background discussion of the electronic wavefunctions corresponding to the edge channels that form an interferometer along the PN junction.

We then analyze the probability to find a particular visibility of the Mach-Zehnder conductance oscillations for an interferometer that has beamsplitters described by random transmission/reflection matrices. The resulting cumulative probability distribution function for the visibility is shown as the theoretical curve in Fig. 3.4G of the main text.

A.3.1 Straight junction of infinite length

Let us first consider the case of an infinite, translationally-invariant PN junction aligned with the y-axis. The overall problem can be formulated in terms of a solution to the time-independent single-particle Schrödinger equation at an energy E equal to the Fermi energy. We may write this solution in the form $\psi(x, y, \tau)$, where τ is a valley index, and we consider only one spin state. We work in a gauge where the vector potential is parallel to the junction. Then, if there are just two edge states at the junction, we may write, in the vicinity of the junction

$$\psi(x, y, \tau) = c_1 \mathrm{e}^{ik_1 y} \mathit{\Phi}_1(x, \tau) + c_2 \mathrm{e}^{ik_2 y} \mathit{\Phi}_1(x, \tau) \tag{A.8}$$

where k_j, for j = 1,2, are the two eigenvalues of the translation operator, $\mathit{\Phi}_j$ are the corresponding eigenvectors, and c_j are arbitrary constants. It will be convenient to choose the normalizations of $\mathit{\Phi}_j$ so that

$$u_j \int_{\infty}^{\infty} dx \sum_{\tau} |\mathit{\Phi}_j|^2 = 1, \tag{A.9}$$

where $u_j = (\mathrm{d}k_j/dE)^{-1}$ is the velocity of the edge mode.

In the simplest model that we have in mind, the functions $\mathit{\Phi}_j$ will have the approximate form

$$\mathit{\Phi}_j(x,\tau) \approx \chi_j(\tau)\mathrm{exp}[-(x-x_j)^2/(2l_{\mathrm{B}}^2)], \tag{A.10}$$

where l_B is the magnetic length, χ_j is the center of gravity of the state j, and the spinor χ_j is a function of the valley index τ. The separation $\Delta_x = x_2 - x_1$ may be written as

$$\Delta_x = U_{\mathrm{ex}}/V', \tag{A.11}$$

where V' is the gradient of the electrostatic potential and U_{ex} is the exchange splitting, which we assume to be constants in the vicinity of the p-n junction. The separation Δ_x is related to the momentum difference $k_2 - k_1$ by

$$\Delta_x = |k_2 - k_1| l_{\mathrm{B}}^2 \tag{A.12}$$

The exchange splitting in Eq. (2.4) results from a term in the Hartree-Fock Hamiltonian of form:

$$H_{\mathrm{ex}} = \frac{U_{\mathrm{ex}}}{2}\hat{n}\cdot\vec{\tau}, \tag{A.13}$$

where $\hat{n}$ is a three-component unit vector and $\vec{\tau}$ are the three Pauli matrices, acting on the valley index τ. In an approximation where one neglects valley-dependent electron-electron interactions, which only occur when two electrons are very close together, there is nothing to pick out one particular orientation of $\hat{n}$ over another. Nevertheless, the exchange splitting may be greater than zero. The choice of $\hat{n}$ at a particular PN junction will then depend on small-symmetry breaking terms, which we will not attempt to predict, and it could vary as one moves along the junction. The spinors $\mathit{\Phi}_j$ are the eigenstates of $\hat{n}\cdot\vec{\tau}$.

The magnitude of the exchange splitting must be determined self consistently, based on the local difference in the occupation of the two valley states. On the microscopic level, we would expect that the exchange potential is not actually a constant over the range of the width of the PN junction, so the quantity U_{ex} in the above equations should be taken as an average over a region covered by the wave functions Φ_j.

It is straightforward to generalize the discussion of a translationally invariant junction to a situation where properties of the junction, including its orientation, may vary adiabatically along its length. (Adiabatically means that the distance scale for changes along the length of the junction should be large compared to $(k_2 - k_1)^{-1}$.) We choose a gauge where the vector potential is always oriented parallel to the junction at the position of the junction. We may now write

$$\psi(x, y, \tau) = c_1 \mathrm{e}^{i\varphi_1(y)} \Phi_1(x, \tau) + c_2 \mathrm{e}^{i\varphi_2 y} \Phi_2(x, \tau) \tag{A.14}$$

$$\psi_j(y) = \int_0^y k_j(y')\mathrm{d}y' \tag{A.15}$$

where y is the distance along the edge and x is measured in the local perpendicular direction. The fact that the magnitudes $|c_j|$ are independent of y is a consequence of conservation of current and our choice for the normalization of Φ_j.

A.3.2 Junction connected to sample edges

Now we consider a PN junction of length L, connected to the sample boundaries at its two ends as depicted in Fig. 1A. We assume that there is a single chiral edge state at any segment of the boundary, and we assume that the edge states at $y = 0$ flow into the junction, while the edge states at $y = L$ flow away from the junction. The portions of the wave function ψ incident at $y = 0$ may be characterized by complex amplitudes a_1 and a_2, such that $|a_1|^2$ and $|a_2|^2$ are, respectively, the currents incident from the left and from the right. Similarly, we may characterize the outgoing wave function by amplitudes b_1 and b_2 for electrons moving to the right and left, respectively, away from the end of the junction at $y = L$. The amplitudes c_j for the wave function along the PN junction will be related to the amplitudes a_j by a 2 x 2 unitary matrix $S^{(0)}$, whose form will depend on details of the sample in the region where the junction meets the edge. Similarly, we may define a matrix $S^{(L)}$, which relates the outgoing amplitudes b_j to the amplitudes $c_j e^{i\varphi_j(L)}$ at the end of the PN junction. The outgoing amplitudes b_j will then be related to the incoming amplitudes a_j by a matrix N, which we may write as

$$N = S^{(L)} M S^{(0)}, \tag{A.16}$$

where M is a diagonal matrix with elements $M_{jj'} = \delta_{jj'} \mathrm{e}^{i\varphi_j(L)}$. Suppose that there is incident beam impinging on the junction from the left, so that $a_2 = 0$. Defining the transmission coefficient T as the probability for an electron to wind up in the right-moving state after leaving the junction, we see that

$$T = |N_{11}|^2 \tag{A.17}$$

Let $\hat{n}_\alpha$ be the unit vector on the Bloch sphere that corresponds to the two-component unit vector $a_j \equiv S^{(0)}_{j,1}$, and let $\hat{n}_\beta$ be the unit vector on the Bloch sphere that corresponds to the two-component unit vector $\beta \equiv \left[\left(S^{(L)} \right)^{-1} \right]_{j,i}$. Let R_φ by the

$O(3)$ matrix that represents a rotation by an angle φ about the z-axis, where

$$\varphi = \varphi_2(L) - \varphi_1(L) = \int_0^L (k_2 - k_1)\mathrm{d}y \tag{A.18}$$

Then we have

$$T = \frac{1 + \hat{n}_\beta \cdot R_\varphi \cdot \hat{n}_\alpha}{2} \tag{A.19}$$

If we describe the vectors $\hat{n}_\alpha$ and $\hat{n}_\beta$ by their polar coordinates, (θ, φ), and define $\varphi_0 = \varphi_\beta - \varphi_\alpha$ then we obtain

$$T = C + D\cos(\varphi + \varphi_0) \tag{A.20}$$

$$C = \frac{1 + \cos\theta_\alpha \cos\theta_\beta}{2}, \text{and } D = \frac{\sin\theta_\alpha \sin\theta_\beta}{2} \tag{A.21}$$

where we recognize Eq. 1 of the main text with $|t_1|^2 = \cos^2 \frac{\theta_\alpha}{2}$ and $|r_2|^2 = \cos^2 \frac{\theta_\beta}{2}$. If the length L is large, the phase φ will change by a large amount when we vary the magnetic field by an amount that is still too small to affect the other parameters in the above equation. Thus T will oscillate between maximum and minimum values given by

$$T_{\mathrm{max}} = C + D \text{ and } T_{\mathrm{min}} = C - D \tag{A.22}$$

If we define the visibility by

$$V = \frac{T_{\mathrm{max}} - T_{\mathrm{min}}}{T_{\mathrm{max}} + T_{\mathrm{min}}} \tag{A.23}$$

then we find

$$V = \frac{D}{C} = \frac{\sin\theta_\alpha \sin\theta_\beta}{1 + \cos\theta_\alpha \cos\theta_\beta} \tag{A.24}$$

A.3.3 Random scattering model

Since the matrices $S^{(0)}$ and $S^{(L)}$ depend on details that we do not know how to calculate, we will consider a model in which the matrices are random matrices in the group $U(2)$. In this case, the unit vectors $\hat{n}_\alpha$ and $\hat{n}_\beta$ will be randomly distributed on the Bloch sphere. We wish to calculate the probability $P(\epsilon)$ that the visibility V is greater than 1 - ϵ. It is useful to change variables to

$$x = \frac{\cos\theta_\alpha + \cos\theta_\beta}{2}, y = \frac{\cos\theta_\alpha - \cos\theta_\beta}{2} \tag{A.25}$$

The probability $P(\epsilon)$ is then given by:

$$P(\epsilon) = \frac{A(\epsilon)}{2} \tag{A.26}$$

where A is the area of the $x - y$ plane that satisfies the constraints

$$-1 < x < 1, -1 < y + x < 1, -1 < y - x < 1, \tag{A.27}$$

$$\begin{gathered}\epsilon > \frac{C - D}{C} = \\ \frac{1 + x^2 - y^2 - [(1 - y^2 - x^2 - 2xy)(1 - y^2 - x^2 + 2xy)]^{(1/2)}}{1 + x^2 - y^2}\end{gathered} \tag{A.28}$$

Ideally, we should compute $A(\epsilon)$ numerically, which we do to calculate the theoretical curve displayed in Fig. 3.4G. However, we can make an analytic approximation, which should be valid in the limit of small ϵ. In this limit, we can expand the right hand side of Eq. A.28 and replace it by the constraint

$$\epsilon > \frac{2x^2}{(1 - y^2)^2} \tag{A.29}$$

Since this constraint forces $|x| < (\frac{\epsilon}{2})^{1/2}$, when ϵ is small we can replace the constraints (Eqn. A.27) by

$$-1 < y < 1 \tag{A.30}$$

The integral is now simple to carry out, giving us

$$P(\epsilon) \approx \int_{-1}^{1} \mathrm{d}y (1 - y^2)(\epsilon/2)^{1/2} = \left(\frac{8\epsilon}{9}\right)^{1/2} \tag{A.31}$$

A.3.4 Skewed distribution Model

As shown in Fig. 3.4G of the main text we find that the experimentally determined values of g_{max} and g_{min} (extracted from fig. A.3A-B) are somewhat lower than those expected from the model based on beamsplitters with uniformly distributed transmission probabilities (discussed in the previous subsection). In fact, from a fit to the data in Fig. 3.4G of the main text, we extract a distribution of beamsplitter transmission probabilities that is significantly skewed (fig. A.3C). This skewness and the corresponding lower values of g_{max} and g_{min} may be related to a relatively low disorder in our sample. In particular, when disorder is low compared to the scale over which the pn junction electrical profile changes, we may expect that an edge channel traveling along the physical graphene edge transforms adiabatically into an edge channel traveling along the pn junction thus suppressing trans-junction scattering and leading to zero trans-junction conductance (as was e.g. observed in [31]). If instead disorder is large where the pn junction meets the graphene edge, we would expect a more uniformly distributed scattering probability into the other edge channel. The skewed distribution that we extract from the data (fig. A.3C) may therefore indicate a regime of intermediate disorder.

A.4 Conductance of two Mach-Zehnder interferometers in series

In this note, we analyze the conductance values observed in the different regions indicated in Fig. 3.6C. As discussed in the main text, we attribute the conductance observed in regions II and III to the presence of one interferometer at each of the PN junctions, and the conductance in region IV to the presence of two interferometers at each of the PN junctions. We thus analyze the expected conductance of MZ interferometers that are connected in series, as depicted in fig. A.4A.

We first assume that we have only one interferometer at each of the PN junctions (corresponding to regions II and III). We also assume that phase coherence is lost in the region between the two interferometers, as the edge channels run along several microns of vacuum edge. The transmission through the two interferometers is given by

$$\begin{aligned} T = T_1 T_2 \sum_{k=0}^{\infty} [(1-T_2)(1-T_1)]^k &= T_1 T_2 \frac{1}{1-(1-T_2)(1-T_1)} \\ &= \frac{1}{\frac{1}{T_1} + \frac{1}{T_2} - 1} \end{aligned} \tag{A.32}$$

where T_i is the transmission probability through interferometer i. Recalling Supplementary Eq. A.20, the transmission through a MZ interferometer is given by

$$T_i = C_i + D_i \cos\left(\varphi^{(i)} + \varphi_0^{(i)}\right) \tag{A.33}$$

Likewise, the transmission through an NPN device with two interferometers (that are independent because of their opposite spin) at each PN interface is given by

$$\begin{aligned} T &= T^{\uparrow} + T{\downarrow} \\ &= \frac{1}{\frac{1}{T_1^{\uparrow}} + \frac{1}{T_2^{\uparrow}} - 1} + \frac{1}{\frac{1}{T_1^{\downarrow}} + \frac{1}{T_2^{\downarrow}} - 1} \end{aligned} \tag{A.34}$$

To compare the average conductance observed in regions II, III, and IV of Fig. 4C of the main text to expectations based on this model, we now assume 50/50 beam splitters and average Eqns. A.32 and A.34 over $\varphi^{(i=1,2)}$. The results are shown in

Supplementary figure A.4C. We see a reasonable agreement. However, we note that it is unclear why one should expect 50/50 beamsplitters.

A.5 Analyzing the gate-length dependence of the Mach-Zehnder oscillation frequencies observed in the NPN measurements on device 2.

To determine the location of the beamsplitters of our Mach-Zehnder interferometers, we analyze the frequency of the conductance oscillations in the top gate/back gate sweeps of our NPN device (device 2) for each of the five top gates. As discussed in the main text, we analyze the frequency of the oscillations observed in the NPN conductance data such as those shown in Fig. 3.6C by focusing on the region of large filling factors ($|\nu_{\mathrm{B,T}}| \gg 1$). In this regime, we can linearize the function g(x) in Eq. A.3, so that it follows that for a given value of $(\sqrt{\nu_{\mathrm{B}}} - \sqrt{-\nu_{\mathrm{T}}})$, the edge-channel separation varies approximately as $\Delta_x \propto \frac{1}{\sqrt{\nu_{\mathrm{B}}}+\sqrt{-\nu_{\mathrm{T}}}}$.

As such, the frequency of the Mach-Zehnder oscillations should be constant as a function of $\frac{1}{\sqrt{\nu_{\mathrm{B}}}+\sqrt{-\nu_{\mathrm{T}}}}$. Therefore, for each top gate, we take the NPN conductance data (such as the data shown in Fig. 3.6C) and plot it against $x = \frac{-1}{\sqrt{\nu_{\mathrm{B}}}+\sqrt{-\nu_{\mathrm{T}}}}$ and $y = (\sqrt{\nu_{\mathrm{B}}} + \sqrt{-\nu_{\mathrm{T}}})$ (fig. A.5). We then divide the measurement range as indicated by the boxes, focusing on the limit $|\nu_{\mathrm{B,T}}| \gg 1$ (i.e, focusing on the right-hand side of the plots), and calculate the absolute value of the Fourier transform with respect to the x-coordinate for all data traces within each box. For each box we average these

Fourier transforms over the y-coordinate. In order to convert from frequency to gate length, we multiply the x-coordinates in each box by a scale factor, which depends on the y-coordinate but is the same across all gates for all boxes with the same y-coordinate. The scale factors are chosen so that for TG5, the peak of the Fourier transform occurs at the gate length 22 μm for each value of y. Finally, we average the resulting frequency-axis-normalized spectra (1 for each box) over all boxes. The results are plotted in Fig. 3.6D of the main text.

We emphasize here that although there may be multiple edge states present corresponding to higher Landau Levels at these higher filling factors, they are so spatially separated from the pn interface that they do not contribute to transport across the junction, as evidenced by the conductance values seen in this region. We therefore believe our MZI picture with two spin species is correct here as well. Increasing the density further will decrease the distance between edge states, and if we go to higher electric fields we expect this picture to eventually break down. Multiple Landau levels may be able to scatter across the junction and a picture analogous to the semiclassical snake state picture may be more applicable. However, we do not believe that we reach that regime in our experiments as we do not see an increase in the average conductance with increasing filling factor.

A.6 Gate-defined equilibration studies.

In this note, we describe how we derive the expected equilibration curves shown in Fig. 3.7E of the main text (red lines), which are based on the assumption that edge-channels only equilibrate if they have the same spin and run along the physical graphene edge.

In the measurements of Fig. 3.7E we apply a voltage V_{IN} to the left lead, ground the top lead ($V_{\mathrm{G}} = 0$), and measure the voltage V_{OUT} at the right lead. Our goal is to calculate V_{OUT} as a function of the side-gate filling factor ν_{S}. We keep the filling factor under the left and right top gate equal, calling it ν_{T}. Furthermore, we work in the regime where $\nu_{\mathrm{B}} > \nu_{\mathrm{T}} \geq 1$, where ν_{B} is the filling factor in the non-top-gated regions, so that we expect $V_{\mathrm{OUT}} = V_{\mathrm{IN}}$ if there is no edge-channel equilibration in the central region and under the assumption that the resistances of the leads are zero.

To calculate the expected V_{OUT}, we start by assuming an infinite input impedance of our voltmeter, allowing us to relate V_{OUT} to the chemical potentials of the edge channels arriving at the right lead as

$$V_{\mathrm{OUT}} = -\frac{\nu_{\mathrm{T}}^{\uparrow}\mu_{\mathrm{OUT}}^{\uparrow} + \nu_{\mathrm{T}}^{\downarrow}\mu_{\mathrm{OUT}}^{\downarrow}}{\nu_{\mathrm{T}}^{\uparrow} + \nu_{\mathrm{T}}^{\downarrow}} \tag{A.35}$$

where $\nu_{\mathrm{T}}^{\uparrow}$ and $\nu_{\mathrm{T}}^{\downarrow}$ are the number of spin-up and spin-down edge channels under the left and the right top gate, with $\nu_T = \nu_{\mathrm{T}}^{\uparrow} + \nu_{\mathrm{T}}^{\downarrow}$, and $\mu_{\mathrm{OUT}}^{\uparrow}$ and $\mu_{\mathrm{OUT}}^{\downarrow}$ are the chemical potentials of these channels when they arrive at the right lead.

We now assume that edge channels only equilibrate if they have the same spin and run along the physical graphene edge. The number of spin-up and spin-down edge channels running along the lower physical edge in the central region is given by $\nu_{\mathrm{S}}^{\uparrow}$ and $\nu_{\mathrm{S}}^{\downarrow}$, respectively, with $\nu_{\mathrm{S}} = \nu_{\mathrm{S}}^{\uparrow} + \nu_{\mathrm{S}}^{\downarrow}$. We thus expect

$$\begin{gathered} \mu_{\mathrm{OUT}}^{\uparrow,\downarrow} = \frac{\nu_{\mathrm{T}}^{\uparrow,\downarrow}\mu_{\mathrm{IN}} + (\nu_{\mathrm{S}}^{\uparrow,\downarrow} - \nu_{\mathrm{T}}^{\uparrow,\downarrow})\mu_{\mathrm{G}}}{\nu_{\mathrm{S}}^{\uparrow,\downarrow}} \\ \text{for } \left(\nu_{\mathrm{S}}^{\uparrow,\downarrow} > \nu_{\mathrm{T}}^{\uparrow,\downarrow}\right) \wedge \left(\nu_{\mathrm{S}} \leq \nu_{\mathrm{B}}\right) \end{gathered} \tag{A.36}$$

and

$$\mu_{\mathrm{OUT}}^{\uparrow,\downarrow} = \frac{\nu_{\mathrm{T}}^{\uparrow,\downarrow}\mu_{\mathrm{IN}} + (\nu_{\mathrm{B}}^{\uparrow,\downarrow} - \nu_{\mathrm{T}}^{\uparrow,\downarrow})\mu_{\mathrm{G}}}{\nu_{\mathrm{B}}^{\uparrow,\downarrow}} \\ \text{for } \left(\nu_{\mathrm{S}}^{\uparrow,\downarrow} > \nu_{\mathrm{T}}^{\uparrow,\downarrow}\right) \wedge \left(\nu_{\mathrm{S}} > \nu_{\mathrm{B}}\right) \tag{A.37}$$

and

$$\mu_{\mathrm{OUT}}^{\uparrow,\downarrow} = \mu_{\mathrm{IN}} \text{ for } \left(\nu_{\mathrm{S}}^{\uparrow,\downarrow} \leq \nu_{\mathrm{T}}^{\uparrow,\downarrow}\right) \tag{A.38}$$

where μ_{G} and μ_{IN} are the chemical potentials of the edge channels emerging from the top and left lead respectively. Equations A.36 to A.38, substituted into Eq. A.35, describe the expected equilibration curves shown in Fig. 3.7E of the main text (red lines). However, to get those curves we need to include the effect of the non-zero resistances of the left and top lead, R_{IN} and R_{G} respectively.

The lead resistances are non-zero because of RC filters, wires, and contact resistance. From current conservation at the left and top lead, we get

$$\mu_{\mathrm{IN}} = -V_{\mathrm{IN}} \frac{\nu_{\mathrm{T}} R_{\mathrm{G}} + R_Q}{\nu_T (R_{\mathrm{IN}} + R_{\mathrm{G}}) + R_Q} \tag{A.39}$$

and

$$\mu_{\mathrm{G}} = -V_{\mathrm{IN}} \frac{\nu_{\mathrm{T}} R_{\mathrm{G}}}{\nu_{\mathrm{T}} (R_{\mathrm{IN}} + R_{\mathrm{G}}) + R_Q}. \tag{A.40}$$

Experimentally, we determine the resistances of the leads by setting $\nu_{\mathrm{B}} = \nu_{\mathrm{T}} = 2$ and measuring the quantum Hall resistance plateau using the left and the top lead. The value of this plateau is given by $R = R_Q/2 + R_{\mathrm{IN}} + R_{\mathrm{G}}$, with $R_Q = h/e^2$, allowing us to extract $R_{\mathrm{IN}} + R_{\mathrm{G}}$. We then assume $R_{\mathrm{IN}} = R_{\mathrm{G}}$ yielding $R_{\mathrm{IN}} = R_{\mathrm{G}} = 4.4k\Omega$. Using Eqns. A.35 to A.40, we obtain the traces plotted in Fig. 3.7E of the main text.

A.7 Calculating charge densities and filling factors from gate voltages.

In this note we describe how we obtain the filling factor values displayed on the axes of our plots. First, we estimate the charge density n_{B} in the non-top-gated region using a simple parallel-plate capacitor model via the equation $n_{\mathrm{B}} = \epsilon_0 \epsilon_{\mathrm{B}} V_{\mathrm{B}}/(d_{\mathrm{B}} e)$, where ϵ_0 is the vacuum permittivity, ϵ_{B} is the dielectric constant of the back-gate dielectric (either hBN or $\mathrm{SiO_2}$), V_{B} is the applied back-gate voltage, d_B is the thickness of the back-gate dielectric, and e is the electron charge. To calculate the charge density n_T in a top-gated region, we use the equation $n_T = n_{\mathrm{B}} + \epsilon_0 \epsilon_{\mathrm{T}} V_{\mathrm{T}}/(d_{\mathrm{T}} e)$, where ϵ_{T} is the dielectric constant of the hBN top-gate dielectric, V_{T} is the applied top-gate voltage, and d_{T} is the thickness of the top-gate dielectric.

To determine the precise location of the charge neutrality point, we measure the conductance while sweeping both the top and bottom gate. We locate the center of the $\nu_{\mathrm{B}} = 0$ plateau, and if it is shifted from $V_{\mathrm{B}} = 0$ by $V_{\mathrm{B,off}}$ we take this into account by substituting $V_{\mathrm{B}} \to V_{\mathrm{B}} - V_{\mathrm{B,off}}$ in our equation for n_{B}. We use a similar procedure for n_{T}. As described in the main text, we then calculate the filling factor $\nu_{(\mathrm{T,B})}$ using the equation $\nu_{(\mathrm{T,B})} = (h/eB) n_{(\mathrm{T,B})}$ where B is the magnetic field, and h is Planck's constant.

Due to quantum capacitance effects, these filling factors do not precisely correspond with the positions where we see robust plateaus in the quantum Hall regime. To correct for this, we tune to an NN' configuration (defined by $\nu_{\mathrm{T}} > 0$ and $\nu_{\mathrm{B}} > 0$) where we are able to identify the locations of particular filling factors by the observation of robust quantum Hall plateaus. We line up the filling factor on the axis with the corresponding plateau by multiplying by a constant factor C_q that accounts for the quantum capacitance. Then, to determine the location of the filling factors in the NP regime, we assume that the quantum Hall plateaus induced on the electron side are of the same size as the quantum Hall plateaus induced on the hole side, and multiply the filling factor obtained from the parallel-plate capacitor model by the same C_q factor. We note that exchange-split levels often span a smaller density range than those separated by a cyclotron energy gap (i.e. the $\nu = 1$ plateau is smaller than the $\nu = 2$ plateau), introducing a small uncertainty into this procedure.

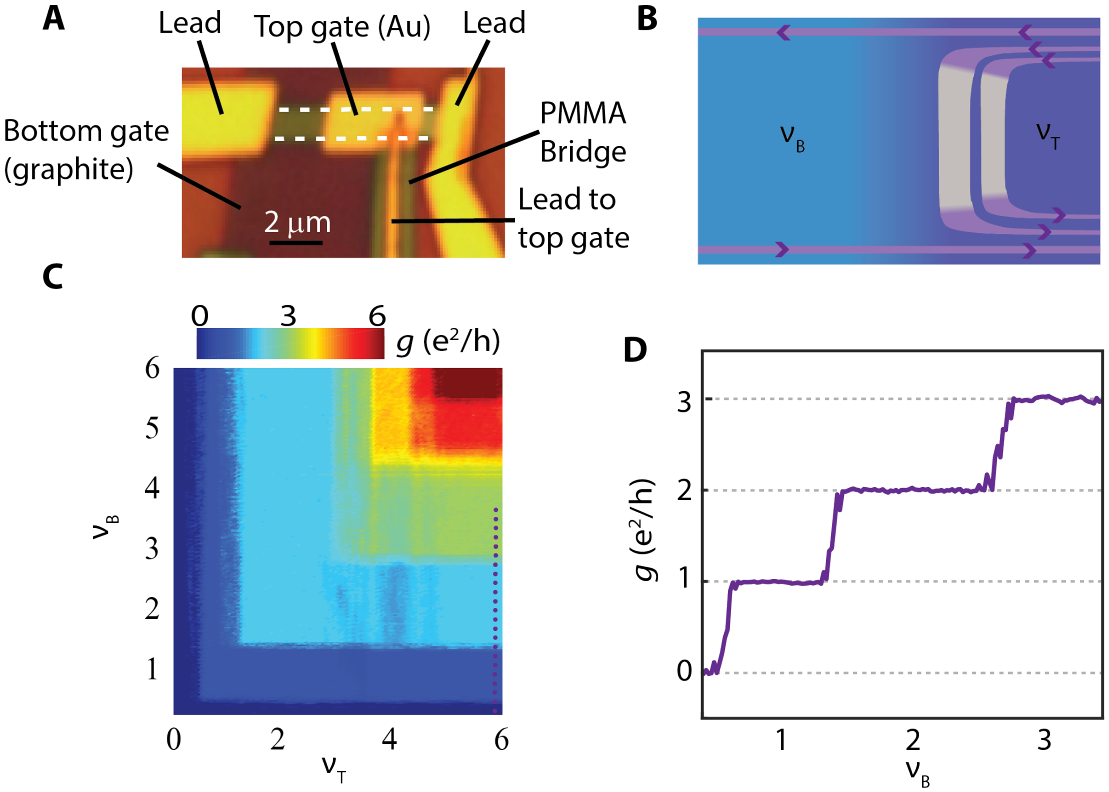

Figure A.1: **Characterization of device 1 in the regime where $\nu_B > 0$ and $\nu_T > 0$ (which we call the NN′ regime). (A)**, Optical microscope image of device 1: a triple-gated, hexagonal boron nitride-encapsulated monolayer of graphene. This image corresponds to the schematic in Fig. 3.3B of the main text. The encapsulated graphene is outlined by the white dashed lines. We tune the filling factor ν_T under the top gate using both the graphite bottom gate and the Au/Cr top gate. We tune the filling factor ν_B in the region to the left of the top gate using the bottom gate only. The device sits on a 285 nm SiO_2/Si global back gate that we use to strongly dope the graphene leading up to the right lead, thus reducing the contact resistance. A bridge of hard-baked PMMA supports the lead contacting the top gate and prevents shorting of this lead to the graphene.

Figure A.1: (Continued) **(B)** A schematic illustration of the edge states present in the system in the NN$'$ regime, with (ν_B, ν_T) = (1,3) as an example. In the NN$'$ regime, the conductance is given by min(ν_B, ν_T). **(C)** Two-terminal conductance in the NN$'$ regime. The Si back gate is set to 60 V. **(D)** Line trace corresponding to the dotted purple line in (B). The observation of conductance quantization in steps of e^2/h confirms that the spin and valley degeneracy is fully lifted in the zLL.

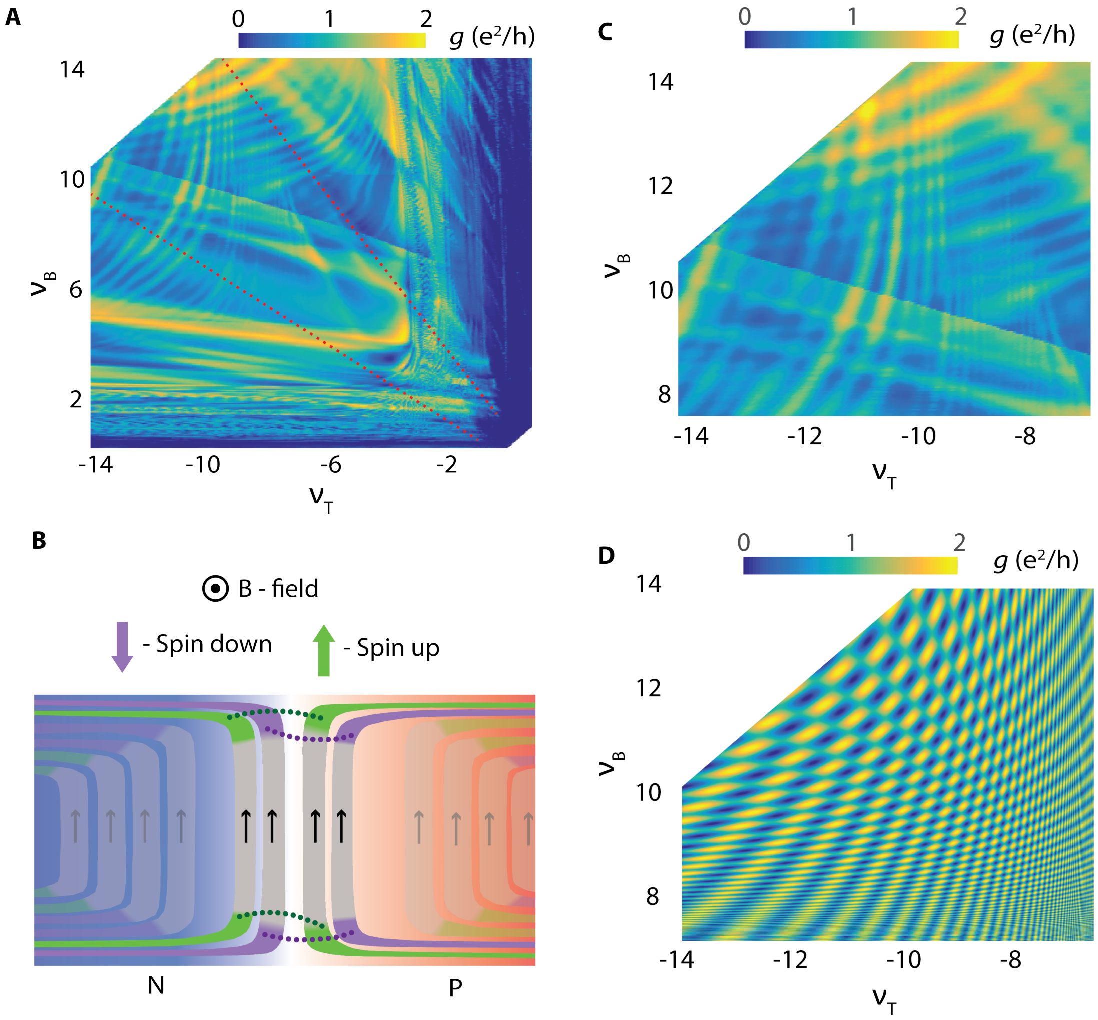

Figure A.2: **Two-terminal conductance of device 1 in the PN regime (in which $\nu_\mathrm{B} > 0$ and $\nu_\mathrm{T} < 0$) at $B = 4$ T and large filling factors. (A)** We observe two hyperbola-shaped sets of conductance oscillations (the red dotted lines guide the eye through the centers of these hyperbolas). As discussed in the main text, our data indicates that these Mach-Zehnders are formed by the two pairs of same-spin edge channels belonging to the zLL.

Figure A.2: (Continued) We observe that the conductance oscillates approximately between 0 and $2e^2/h$, even at large filling factors, indicating that two Mach-Zehnder interferometers mediate transport across the PN junction even when there are many edge channels in the system. **(B)** Schematic that depicts edge channels belonging to higher LLs that do not communicate across the junction or with the zLL, presumably because of their larger spatial separation.**(C)**Zoom in on large filling-factor region of data shown in (A). **(D)** Simulation of the two-terminal conductance as a function of filling factors based on the model sketched in Fig. 3.4(B-D) of the main text.

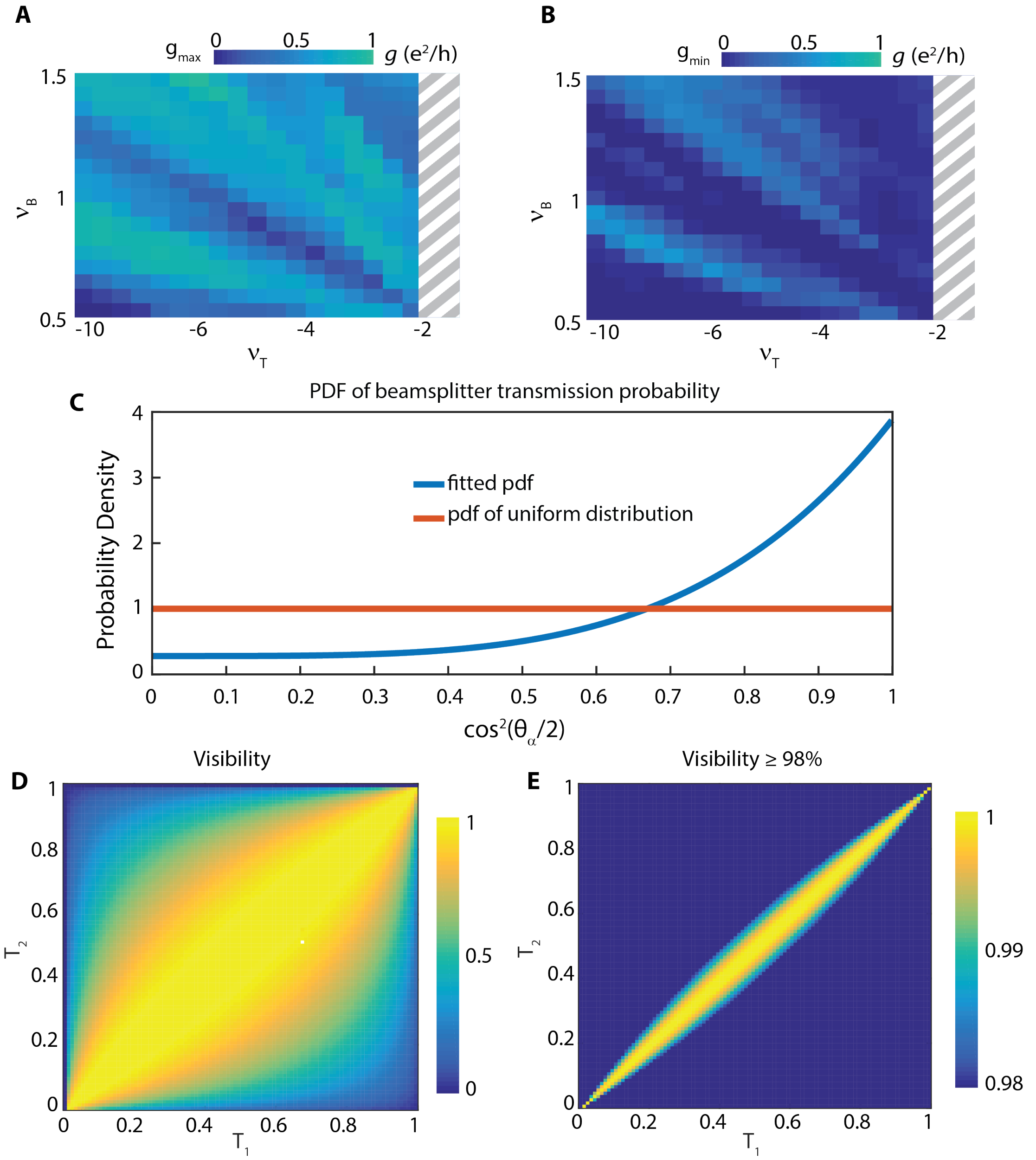

Figure A.3: **Analysis of transmission and reflection in Mach-Zehnder beamsplitters.** **(A)** Local g_{max} of the conductance oscillations observed in Fig. 3.4A of the main text. The grey dashed box indicates where g_{max} was not extracted due to non-resolved oscillations.

Figure A.3: (Continued) **(B)** Local g_{min} of the conductance oscillations observed in Fig. 3.4A of the main text. The grey dashed box indicates where g_{min} was not extracted due to non-resolved oscillations. **(C)** The skewed probability distribution function (blue) used to obtain the curves in Fig. 3.4G of the main text, compared to the uniform distribution function (red).**(D-E)** Theoretical calculation of the Mach-Zehnder visibility(assuming no dephasing) as a function of the transmission probabilities $T_i = |t_i|^2$ of the two beamsplitters, where t_i is the tunneling coefficient of beamsplitter i, for both a large range of visibilities (D) and a range in which the visibility 98% **(E)**. These plots can be used to estimate tunneling coefficients given a measured visibility.

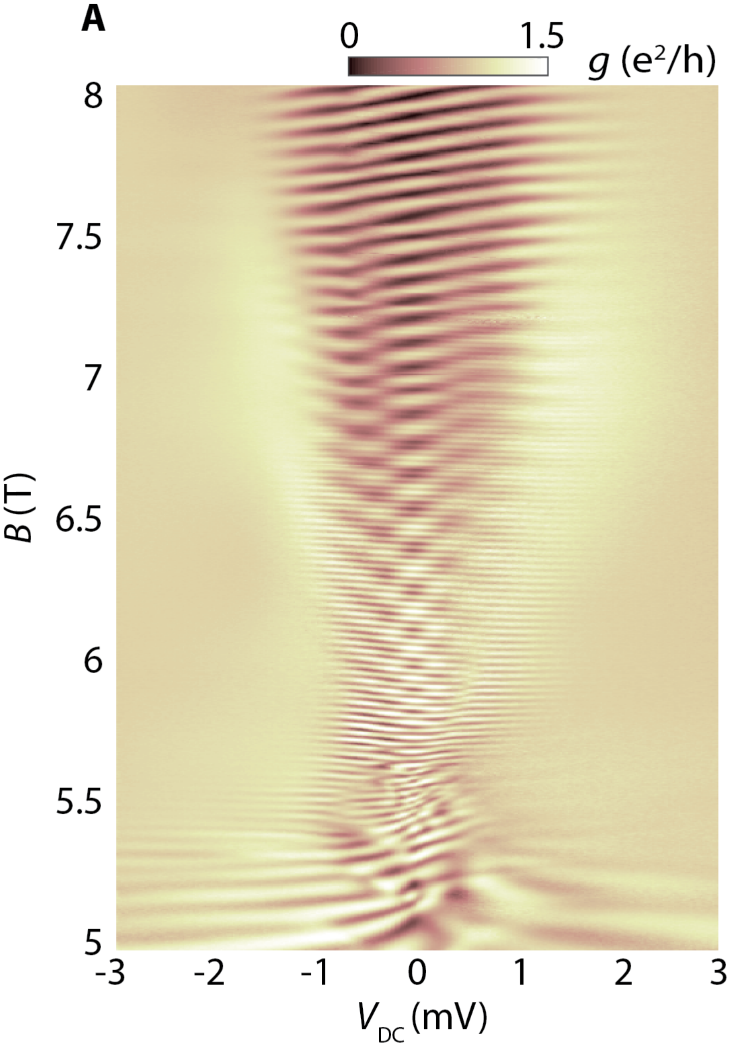

Figure A.4: **The effect of a DC bias on the differential conductance of a PN junction. (A)** Two-terminal conductance of device 1 as a function of magnetic field B and DC voltage bias V_{DC}. At $B = 8$ T, we have $\nu_{\mathrm{B}} = 1$ and $\nu_{\mathrm{T}} = -2$.

Figure A.4: (Continued) Different spatial derivatives of the energies of the two Landau sublevels forming an interferometer (see e.g., Fig. 3.4D of the main text) can lead to an energy-dependent inter-edge-channel distance Δ_x, which results in a differential conductance that depends on V_{DC}: if V_{DC} is applied asymmetrically, as in our measurements (with the chemical potential of the left channel raised to V_{DC} and that of the right channel remaining at 0V), the differential conductance is given by $g \sim \cos[\frac{2\pi BL}{\Phi_0}\Delta_x(V_{\mathrm{DC}})]$. In this case it is clear that a change in Δ_x caused by a change in V_{DC} can be compensated for by a change in B, consistent with the diagonal stripes of constant differential conductance observed in the region around $B = 8$ T and in Fig. 3A of the main text. If the bias is somehow symmetrized, due to e.g. electron-electron interactions [115], the chemical potential of the left (right) channel equals $\frac{V_{\mathrm{DC}}}{2}$ ($\frac{-V_{\mathrm{DC}}}{2}$), and correspondingly $g \sim \cos[\frac{2\pi BL}{\Phi_0}\Delta_x(\frac{V_{\mathrm{DC}}}{2})] + \cos[\frac{2\pi BL}{\Phi_0}\Delta_x(\frac{-V_{\mathrm{DC}}}{2})]$. This may lead to more complex behavior such as the checkerboard patterns observed around $B = 6$ T [115]. We note that a bias-dependent electrostatic gating effect may also change the inter-channel distance [56] and correspondingly lead to a bias-dependent differential conductance.

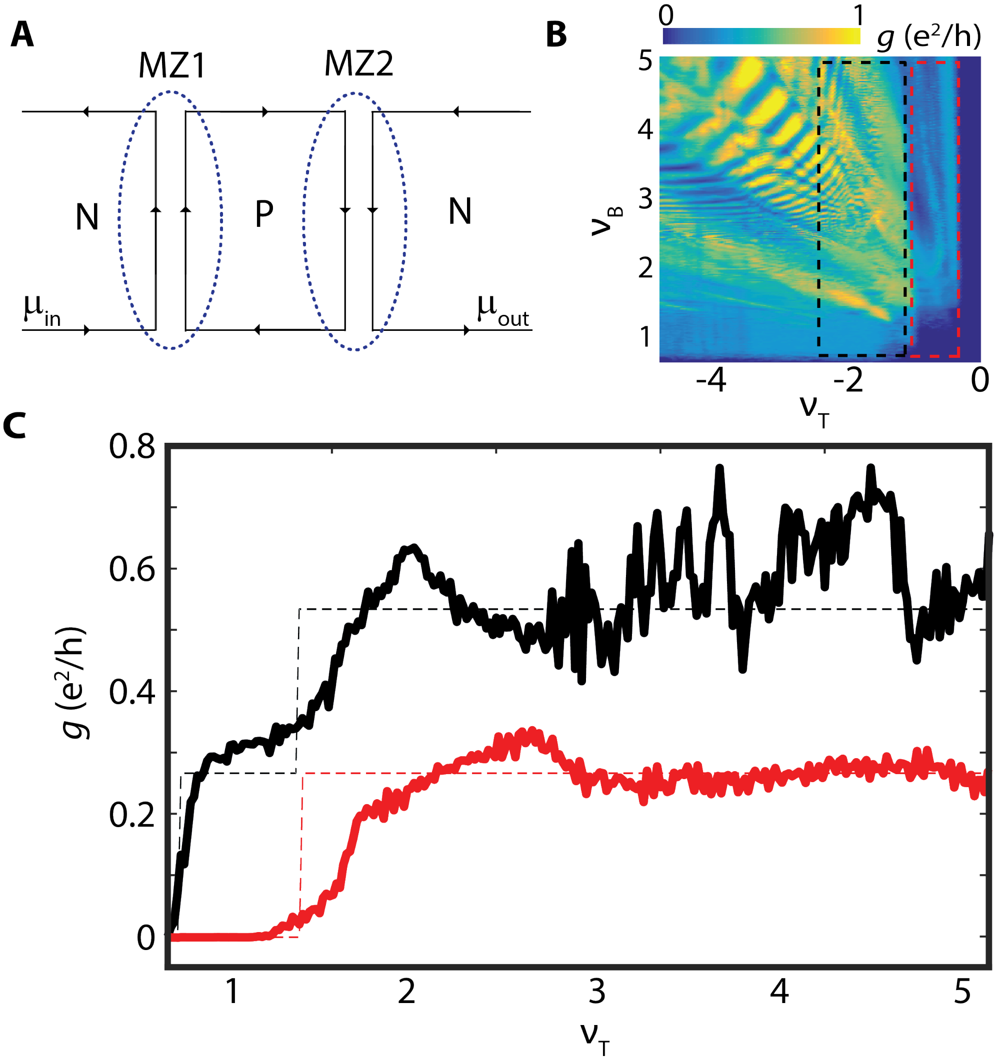

Figure A.5: **Analyzing the average conductance observed in NPN measurements on device 2.** **(A)** Schematic of two PN junctions in series (MZ1 and MZ2), as formed in our NPN device. μ_{in} is the chemical potential of the edge entering the first interferometer and μ_{out} is the chemical potential exiting the second interferometer. **(B)** Two-terminal conductance measurement as a function of back-gate and top-gate filling factors $\nu_{\rm B}$ and $\nu_{\rm T}$, measured across top gate 1. The red (black) dashed box indicates a region with one (two) edge channel(s) in the top-gated region.

Figure A.5: (Continued) **(C)** The red (black) data corresponds to the measured conductance within the red (black) dashed box in (B), averaged over ν_{T}. The dashed lines indicate the expected average conductance corresponding to 0, 1, or 2 interferometers formed at each of the PN interfaces, assuming 50/50 beamsplitters as discussed in section A.4.

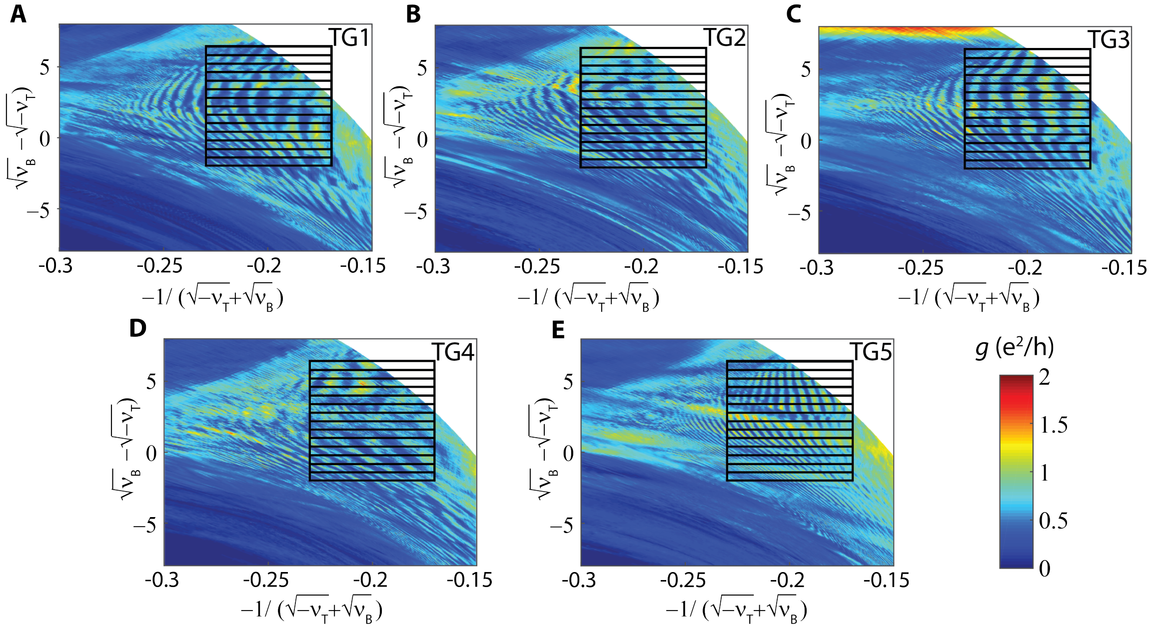

Figure A.6: **Analyzing the gate-length dependence of the Mach-Zehnder oscillation frequencies observed in NPN devices. (A-E)** The conductance maps for all top gates (TG1-TG5) at $B = 8$ T, plotted in a transformed coordinate system. We address each top gate individually by using the appropriate leads. An image of the device is shown in Fig.3.6A of the main text. The lengths of the top gates are shown in Fig.3.6B of the main text. Note that top gate 5 is the longest and correspondingly shows the fastest conductance oscillations. The boxes indicate the regions in which we take Fourier transforms of the data to compare the frequency of the observed Mach-Zehnder oscillations between the different gates, resulting in Fig.3.6D of the main text (see section A.5.

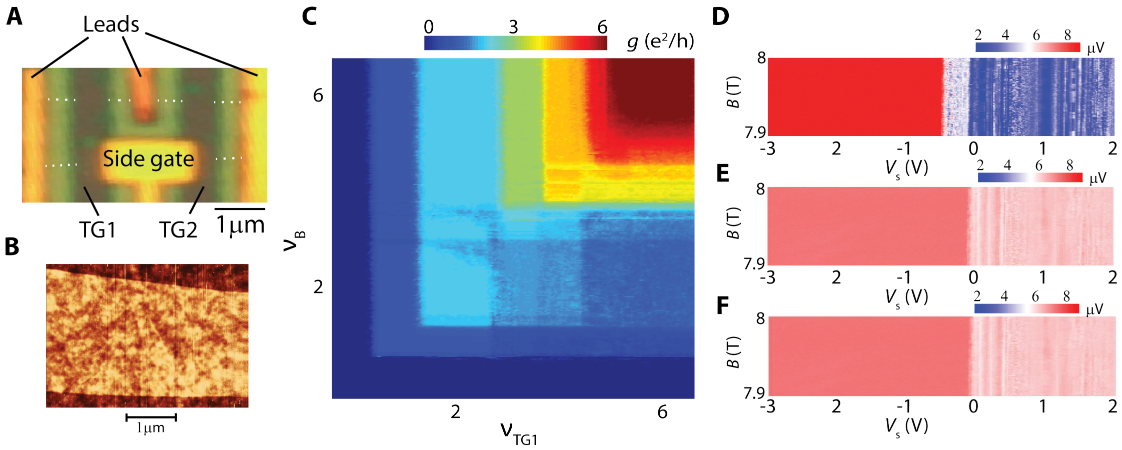

Figure A.7: **Device 3: verifying the presence of broken-symmetry quantum Hall states and measurements of edge channel equilibration as a function of magnetic field.** **(A)** Optical image of device 3. The dotted line outlines the graphene. **(B)** AFM image of the clean, hBN-encapsulated graphene flake used for device 3. **(C)** Two-terminal conductance measured across top gate 1 (TG1) using the left and middle lead, as a function of the filling factor ν_{TG1} under TG1 and the filling factor ν_{B} in the non-top-gated region. Conductance plateaus that are present for all integers from $\nu = 1$ to $\nu = 6$ confirm that the spin and valley degeneracy of the Landau levels is lifted. These plateaus are also present in a similar measurement across TG2 (not shown). **(D-F)** Equilibration measurements as a function of B and the side-gate voltage V_S, as described in the main text. The two top gates are set at ν_{T}=1 for **(D)** ν_{T}=2 for **(E)** and ν_{T}=3 for **(F)**.

Appendix B

Additional information for spin wave experiments

B.1 Methods

B.1.1 Sample fabrication

All devices consist of graphene encapsulated by two layers of hexagonal boron nitride (hBN) on doped Si chips with a 285 nm layer of SiO_2 that acts as a dielectric for the Si back gate. Graphene is mechanically exfoliated from bulk graphite obtained from NGS Naturgraphit GmbH using 1009R tape from Ultron Systems and subsequently encapsulated in hexagonal boron nitride (hBN) using a dry transfer process [114]. Before the first metal deposition step, we annealed the devices in vacuum at 500°C to improve device quality. We then created top gates using electron-beam lithography and thermal evaporation of Cr/Au. We etched the devices into the desired geometry by reactive ion etching in O_2/CHF_3 using a PMMA/HSQ bilayer of resist (patterned by electron-beam lithography) as the etch mask. To fabricate edge-contacts to the graphene we etched through the entire hBN/graphene stack. We then created edge contacts by thermally evaporating Cr/Au while rotating the sample using a tilted rotation stage.

B.1.2 Measurement

Our measurements were performed in a Leiden dry dilution refrigerator with a base temperature of 20 mK. Measurements of differential conductance were performed using a lock-in amplifier with an a.c. excitation voltage of 50 μV at 17.77 Hz. All measurements of differential conductance were corrected for contact/line resistances, which were independently determined by lining up the robust $\nu = 2$ QH conductance plateau with $2e^2/h$.

B.2 Equilibration of edge states at hot spots

One question that arises from this study is why, after decades of experimental investigation into QH ferromagnets, has this phenomenon not been observed in GaAs quantum wells? We posit that this is due to the readiness of edge states in graphene to equilibrate over small length scales due to the sharp confining potentials. Because there is a limited spatial range over which the ‘hot spot’ magnon generation can occur adjacent to the $\nu = 1$ ferromagnetic bulk, spin-flip induced edge equilibration must occur over short lengths. Past studies have shown that in graphene edges of the same spin are able to fully equilibrate over length scales < 1 μm [31, 58, 62], while similar studies done in GaAs found typical lengths of around tens of microns, and sometimes up to 200 μm [28, 29, 116]. In order to experimentally verify that magnons are generated at these corner 'hot spots', we have fabricated a device with gated corners showing conductance changes at E_{Z} in accordance with our magnon model (Fig. B.11).

The difference in experimentally-determined equilibration lengths between graphene and GaAs is likely due to the sharper confining potentials in graphene, which allow for small spatial edge channel separationincreasing the likelihood of inter-channel scattering. Additionally, a smooth potential may allow for edge reconstruction [117], which if present, could also affect the inter-channel scattering rate and limit magnon generation. Experiments in GaAs based systems have shown that edge recondsturction plays an important role due to the smooth confining potential [118]. The graphene devices investigated in this work have gate electrodes located at just a few tens of nanometers distance away, likely limiting the amount of edge reconstruction. Furthermore, the close proximity of the metal gates to the graphene may screen the electric fields that cause edge reconstruction, which is another potential difference with GaAs-based systems [119].

However, interestingly, we note that although an electrostatically-defined confinement potential is able to suppress the magnon signal, it does not eliminate it completely (Fig. B.11). This suggests that strong edge disorder is not required for the $\nu = 2$ and $\nu = 1$ edge channels to equilibrate, and that it is possible that magnons could be generated in GaAs devices with a sharp electrostatic confinement potential. We note, however, that while magnon generation may be possible, magnon propagation may not be as efficient in GaAs systems due to large spin-orbit coupling [30] and more nuclear spins [120] relative to graphene, which could facilitate magnon dissipation. Such dissipative processes would be important because, as we describe in the main text, magnon generation itself does not affect the sample conductance – only when magnons are able to propagate and are absorbed in by electrons in other edge channels do we detect a change in sample conductance.

Additionally, we note that even when we do not explicitly add an extra edge state near the contacts (by gating the side regions to $\nu = 2$), contact doping of the graphene by the Cr/Au leads [111] introduces additional spin-down edge stateswhich also leads to magnon generation at EZ.

B.3 Calculating V_{dc} necessary to exceed V_{EZ} given a finite contact resistance

In a two-terminal measurement, the applied bias voltage (V_{dc}) drops over both the contact resistances at both the source and the drain. The d.c. current is therefore

$$I_{\mathrm{dc}} = \frac{V_{\mathrm{dc}}}{2R_{\mathrm{C}} + R_{\mathrm{Q}}} \tag{B.1}$$

where R_{Q} is the quantum resistance of an edge channel, and where R_{C} includs both the contact resistance at each lead as well as the filtering on the lines. The filtering on each line is 4.5kΩ, and the contact resistance at each lead of a typical device is about 500Ω.

The actual d.c. voltage that drops over the edge channel (V'_{dc}) is therefore given by

$$V'_{\mathrm{dc}} = I_{\mathrm{dc}} R_{\mathrm{Q}} \tag{B.2}$$

Therefore:

$$V_{\mathrm{dc}} = \frac{V'_{\mathrm{dc}}\Big(2R_{\mathrm{C}} + R_{\mathrm{Q}}\Big)}{R_{\mathrm{Q}}} \tag{B.3}$$

In our figures, we use 'V_{EZ}' (V_{EZ} = -E_{Z}/e) to denote the bias at which -eV'_{dc} reaches the Zeeman energy ($E_{\mathrm{Z}} = g\mu_B B_T$).

B.4 Circuit analysis for two-terminal conductance measurement.

In Fig. B.1 The (particle) current conservation equation at the source reservoir (labeled μ_1) is:

$$\frac{2\mu_1}{R_{\mathrm{Q}}} = \frac{\mu_2 - \varepsilon_2}{R_{\mathrm{Q}}} + \frac{\mu_1 + \varepsilon_1}{R_{\mathrm{Q}}} + \frac{\mu - \mu_1}{R_{\mathrm{C}}} \tag{B.4}$$

where R_{Q} is the resistance quantum. As described in the main text, ε_i denotes the chemical potential redistributed between edge states at the ith contact. Additionally, although there are indeed also spin-flips occurring at the negative-bias magnon generation location when positive bias magnons are being generated (and for the reverse case), we ignore these in our analysis because they do not contribute to changes in the conductance.

The equation at the drain contact is:

$$\frac{\mu_2 + \varepsilon_2}{R_\mathrm{Q}} + \frac{\mu_1 - \varepsilon_1}{R_\mathrm{Q}} = \frac{2\mu_2}{R_\mathrm{Q}} + \frac{\mu_2}{R_\mathrm{C}} \tag{B.5}$$

Solving for μ_2 we find

$$\mu_2 = \frac{\mu + \varepsilon_2 - \varepsilon_1}{2 + \frac{R_\mathrm{Q}}{R_\mathrm{C}}} \tag{B.6}$$

Using the chemical potential of the voltage source as $\mu = -eV_\mathrm{dc}$, and the charge current $I = -eI_\mathrm{P}$ (where I_P is defined as $\frac{1}{e^2}\,\frac{\mu_2}{R_\mathrm{C}}$ to normalize the units) the differential conductance measured is

$$\frac{\mathrm{d}I}{\mathrm{d}V_\mathrm{dc}} = \frac{\mathrm{d}I_\mathrm{P}}{\mathrm{d}\mu} = \frac{\big(\mathrm{d}\mu_2/R_\mathrm{C}\big)}{\mathrm{d}\mu} \tag{B.7}$$

$$\frac{\mathrm{d}I}{\mathrm{d}V_\mathrm{dc}} = \frac{1}{2R_\mathrm{C} + R_\mathrm{Q}}\Big(1 + \frac{\mathrm{d}\varepsilon_2}{\mathrm{d}\mu} - \frac{\mathrm{d}\varepsilon_1}{\mathrm{d}\mu}\Big) \tag{B.8}$$

This becomes Equation 1 (main text) in the absence of contact resistance (R_C =0).

B.5 Circuit analysis for non-local voltage measurements.

In Fig. B.2 the chemical potential of the edge states after magnons are absorbed are labeled as $\mu_i - \varepsilon_i$ and $\mu_i + \varepsilon_i$ where 'i' denotes the contact where the chemical potential originates. We calculate the conductance expected after the Zeeman energy has been reached. This device has 5 contacts in total. We write a current conservation equation at each contact:

$$\mathrm{L}_1 : \mu_2 - \varepsilon_2 + \mu_1 + \varepsilon_1 = 2\mu_1 \tag{B.9}$$

$$\mathrm{L}_2 : \mu_3 - \varepsilon_3 + \mu_2 + \varepsilon_2 = 2\mu_2 + \mu_2 \frac{R_{\mathrm{Q}}}{R_{\mathrm{C}}} \tag{B.10}$$

$$\mathrm{L}_3 : (\mu - \mu_3) \frac{R_{\mathrm{Q}}}{R_{\mathrm{C}}} + \mu_3 + \varepsilon_3 + \mu_4 - \varepsilon_4 = 2\mu_3 \tag{B.11}$$

$$\mathrm{L}_4 : \mu_5 - \varepsilon_5 + \mu_4 + \varepsilon_4 = 2\mu_4 \tag{B.12}$$

$$\mathrm{L}_5 : \mu_1 - \varepsilon_1 + \mu_5 + \varepsilon_5 = 2\mu_5 \tag{B.13}$$

Solving for μ_2 we find

$$\mu_2 = \frac{\mu + \varepsilon_2 - \varepsilon_3}{2 + \frac{R_{\mathrm{Q}}}{R_{\mathrm{C}}}} \tag{B.14}$$

Therefore,

$$\frac{\mathrm{d}I}{\mathrm{d}V_{\mathrm{dc}}} = \frac{\mathrm{d}I_{\mathrm{P}}}{\mathrm{d}\mu} = \frac{\mathrm{d}\big(\mu_2/R_{\mathrm{C}}\big)}{\mathrm{d}\mu} = \frac{1}{2R_{\mathrm{C}} + R_{\mathrm{Q}}}\Big(1 + \frac{\mathrm{d}\varepsilon_2}{\mathrm{d}\mu} - \frac{\mathrm{d}\varepsilon_3}{\mathrm{d}\mu}\Big) \tag{B.15}$$

The non-local voltage measured is:

$$S_{\mathrm{NL}} = \frac{\mathrm{d}V_{\mathrm{NL}}}{\mathrm{d}V} = \Big(\frac{\mathrm{d}\varepsilon_4}{\mathrm{d}\mu} - \frac{\mathrm{d}\varepsilon_5}{\mathrm{d}\mu}\Big) \tag{B.16}$$

By defining S_{NL} as the difference between two voltage probes, any edge current which reaches the two voltage probes should not affect the measurement — although we do see some small background voltage which is explained in Fig. B.7B.

A similar circuit analysis can be done for any of the configurations found in the main text or in this appendix.

B.6 Theoretical notes.

We first note that the energy levels shown in the Figure 4.5D are only schematic. The actual Landau levels will be broadened due to electron-electron interactions and, perhaps, disorder. The curves represent more accurately the energy in the middle of the Landau level, and the ordering of the levels is more meaningful than the actual energies.

Our ordering of levels was guided by the following observations. For a uniform graphene system at $\nu = 0$, it is believed that the valley anisotropy energy is large compared to the Zeeman energy, and that the ground state is a canted antiferromagnet state [25, 22]. In this half-filled N=0 Landau level, there is one electron per flux quantum on each sublattice, with spins oriented predominantly in opposite directions. In the absence of Zeeman coupling the antiferromagnetic axis could point equally well in any direction, with no difference in the energy [21]. In the presence of the Zeeman field, there is a small energy gain for the antiferromagnetic axis to line up in the x-y plane, perpendicular to the Zeeman field, allowing the spins on both sublattices to cant slightly in the direction of the Zeeman field. The energy gain for this is of order E_Z^2/E_A, where E_A is the valley anisotropy energy.

For a general filling fraction in the range $-1 < \nu < 0$, if one calculates the ground state energy in a restricted Hartree-Fock approximation, which assumes that only two of the possible spin-valley states are occupied by electrons, one generally finds that one valley, say the K valley, has one electron per flux quantum, while the other valley has occupancy $1 + \nu < 1$. For fillings very close to $\nu = 0$, the system may remain in a canted configuration, but for $|\nu|$ exceeding a critical value, of order E_Z/E_A, it will be more favorable for the antiferromagnetic axis to align in the z-direction, so that the majority spin is fully aligned with the Zeeman field. (See, e.g. the discussion in [121]) Similarly, for $0 < \nu < 1$, we would find the antiferromagnetic spin axis to be aligned with the magnetic field, except for a small region close to $\nu = 0$.

In a situation where the electron density varies rapidly in space, the spin and valley orientationsshould be determined by the dominant exchange energy, arising from the long-range part of theCoulomb interaction, which is indifferent to the specific orientation of the occupied levels in spin-valley space, but disfavors any rapid changes or discontinuities in the occupations. In a boundary between $\nu = -1$ and $\nu = 1$, we are forced to have two discontinuities in occupancy, but we can avoid any other discontinuities, if we choose to fill the levels in the order suggested in Fig. 4.5D. Moreover, it is likely that in a relatively steep boundary, the canted orientation will be completely suppressed, and that spins will remain quantized along the z-axis. We have seen in a previous study an absence of mixing between spin states at a $\nu = 1/\nu = -1$ interface, supporting our assumption of spin alignment in the present case [110].

By contrast, when the filling fraction is $\nu = 0$ under the center of our gate, it is likely that the system will assume the canted orientation near the center of the gate. At the same time, there should be a strip on either side of the gate, where the filling fraction is intermediate between $\nu = 1$ and $\nu = 0$, where the antiferromagnetic axis is in the z-direction. An interval where the filling fraction is between $\nu = 1$ and $\nu = -1$, with spin axes parallel to z, will act as a barrier, to a spin wave incident from a region where $\nu = 1$, as the energy at the bottom of the spin wave band will be raised by an amount of order the valley anisotropy energy (This should be small compared to the Coulomb exchange energy, but larger than the Zeeman energy) [122]. In the case where the filling under the gate is $\nu = -1$, we would expect the barrier regions at the two sides to be relatively thin, and it is plausible that the spin waves can tunnel rather easily through the barrier region. When the filling at the gate center is $= 0$, we would expect the barriers to be much thicker, and tunneling through the barriers should be reduced accordingly.

In a bulk region where the filling is very close to $= 1$, we expect that the unoccupied spin state will have its spin opposite to the magnetic field, but it will have no particular preference for either the K or K valley or an arbitrary linear combination of them. Different valley polarizations may be selected near the physical boundaries of the sample, but we expect that the valley orientation in the vicinity of a gate where the charge density varies rapidly should be determined by energy considerations under the gate. It should cost relatively little energy for the valley orientation to vary smoothly between the sample edges and the gate, and we would not expect spin-wave propagation to be affected by such variations.

Our analysis, based on a Hartree-Fock approximation, ignores correlation effects, which can lead to fractional quantized Hall states, varying spin polarization, and transitions between different spin states in uniform graphene sample [121, 123]. However, we would not expect such correlation effects to be important in the present case, where the charge density varies considerably on a sub-micron scale.

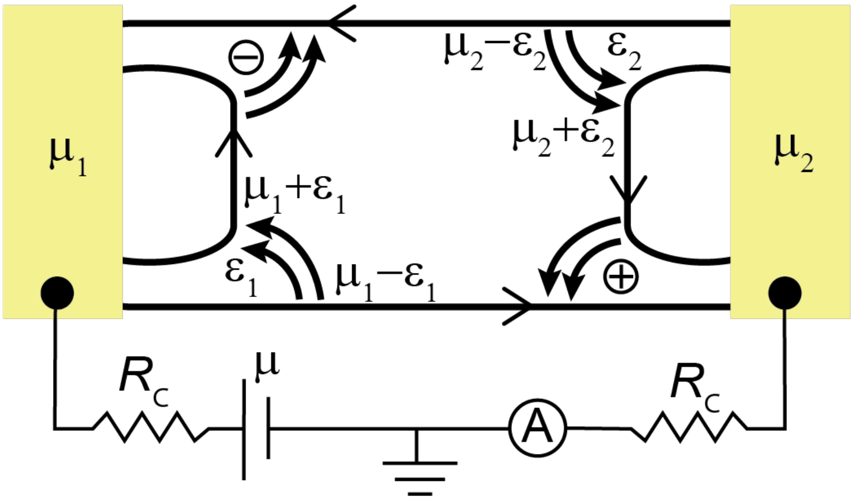

Figure B.1: **Schematic of a two-terminal device where a voltage is sourced at the left contact and drained at the right.** The negative and positive signs denote magnon generation for negative and positive V_{dc} respectively. ε_1 and ε_2 denote locations where magnon absorption occurs. Arrows indicate how the chemical potential redistributes after magnon generation, and the chemical potential of the edge states after magnons are absorbed are labeled. the electrochemical potential applied by the voltage source is defined as μ. μ_1 and μ_2 are the chemical potential reservoirs connected to the source and drain via a contact resistance R_{C} (assumed to be identical for both contacts).

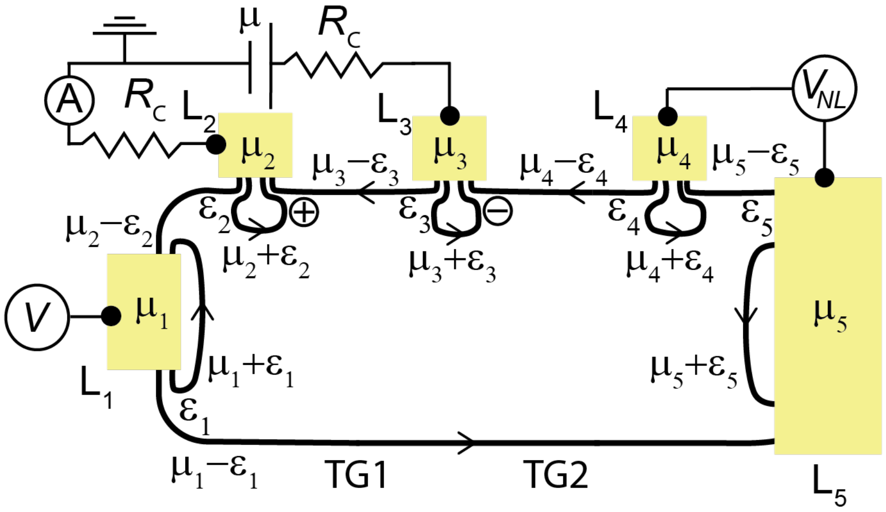

Figure B.2: **Schematic circuit diagram of the multi-terminal device** Device 2 - optical micrograph shown in Fig. 4.4A) that is used to measure S_{NL}. μ_1, μ_2, μ_3, μ_4 and μ_5 are the chemical potential reservoirs connected to each contact (L_1-L_5) by a contact resistance R_{C}. The electrochemical potential applied by the voltage source is defined as μ. Voltage is sourced at L_3 and drained from L_2. L_1 is floating. S_{NL} is measured between L_4 and L_5. The negative and positive signs denote magnon generation for negative and positive V_{dc} respectively. ε_1, ε_2, ε_3, ε_4, and ε_5 label locations of magnon absorption.

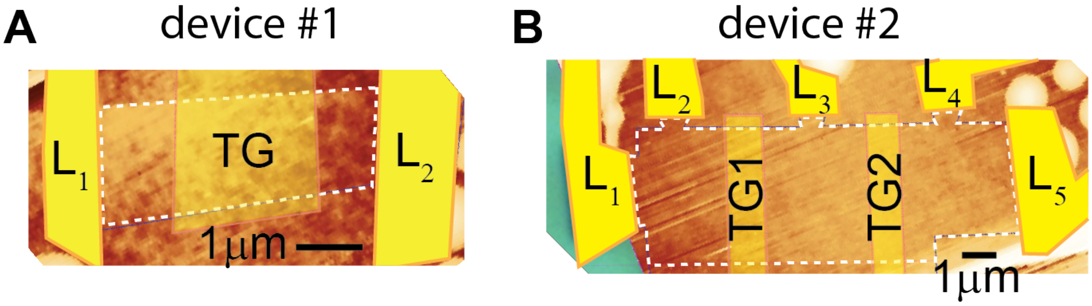

Figure B.3: **Atomic force microscope (AFM) images of device 1 and device 2 (A-B)** AFM images of the hBN/graphene/hBN heterostructures used for device 1 and device 2. Leads are illustrated in solid yellow and top gates are in transparent yellow. Dashed white lines outline the graphene flake. Scale bar: 1 μm.

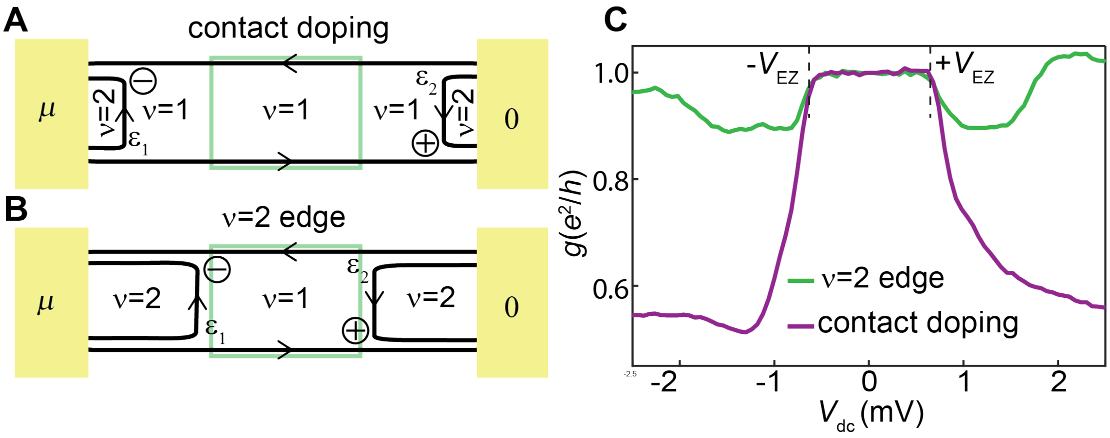

Figure B.4: **Comparison of spin-reservoirs from contact doping and spin reservoirs from the $\nu = 2$ edge (device 1).** **(A)** Schematic of device 1 where both the top and back-gated regions are set to $\nu = 1$ and the magnon generation and absorption occurs at the contacts (See Fig. 4.3 for optical micrograph, and Fig. B.3 for AFM image). The chemical potential redistribution at each magnon absorption site 'i' is labeled by ε_i (see discussion of ε_i in the main text). **(B)** Schematic where the top-gated region is set to $\nu = 1$ and the back-gated regions are set to $\nu = 2$. Magnon generation and absorption occurs at the interface between $\nu = 1$ and $\nu = 2$. **(C)** Two-terminal conductance measurement at $B = 4$ T where a constant d.c. voltage (V_{dc}) and a 50 μV a.c. excitation voltage (V_{ac}) are applied to the left contact and the differential conductance (dI/dV, where V = V_{dc}+V_{ac}) is measured through the right contact. The two cases are compared, one in which contact doping provides an opposite-spin reservoir as shown in (A) (V_{BG} =1.24 V and V_{TG}= 0.12 V) the other where the ν=2 provides the opposite-spin reservoir as shown in (B) (V_{BG} =3 V and V_{TG} = -0.18V.

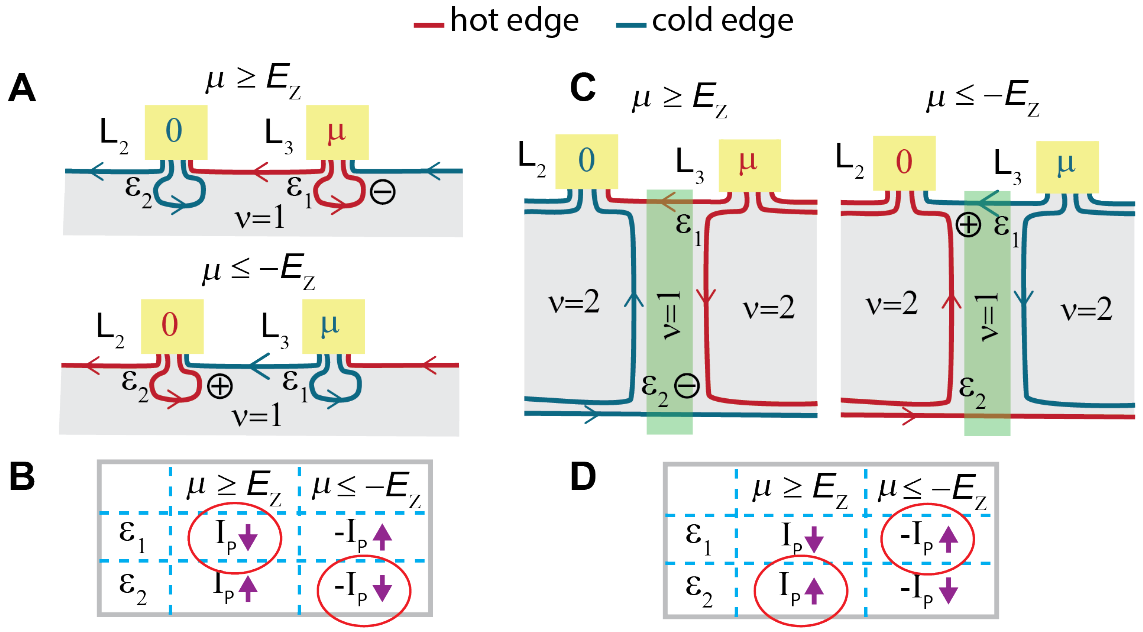

Figure B.5: **Effect of relative magnon absorption on conductance using different lead configurations.** Schematic illustrations of different two-terminal conductance measurement using leads L_3 and L_2 where hot (cold) edges are colored red (blue), for both $\mu \geq E_\mathrm{Z}$ and $\mu \leq -E_\mathrm{Z}$. The magnon generation site is labeled by the plus (minus) sign for positive (negative) bias (See Fig. 4.4A for optical micrograph, and Fig. B.3 for AFM image). **(A)** Measurement where the entire device is tuned to $\nu = 1$, so TG1 is not shown. (Upper panel) $\mu \geq E_\mathrm{Z}$ $(-eV_\mathrm{dc})$: magnon absorption at ε_1 transfers chemical potential from a forward moving edge to a backwards moving edge — causing the particle current (I_P where I_P = -I/e) to decrease. Conversely, magnon absorption at ε_2 transfers chemical potential from a backward moving edge to a forward moving edge, increasing I_P. (Lower panel) $\mu \leq -E_\mathrm{Z}$: magnon absorption at ε_1 (ε_2) causes an increase (decrease) in $|-I_\mathrm{P}|$.

Figure B.5: (Continued) **(B)** A summary of the effects of ε_1 and ε_2 at $\mu \geq E_{\mathrm{Z}}$ and $\mu \leq -E_{\mathrm{Z}}$. For $\mu \geq E_{\mathrm{Z}}$, ε_1 is closer to the magnon generation site, so the current change caused by ε_1 is predicted to be dominant and is circled in red. For $\mu \leq -E_{\mathrm{Z}}$, ε_2 is closer to the magnon generation site, so the current change caused by ε_2 is predicted to be dominant and is circled in red. **(C)** Measurement where the region under TG1 (ν_{TG1}) is tuned to $\nu_{\mathrm{TG1}} = 1$ while the regions outside, tuned by the back gate (ν_{BG}), are set to $\nu_{\mathrm{BG}} = 2$, providing a spin-down reservoir in the inner edge channel. (Left panel) $\mu \geq E_{\mathrm{Z}}$ ($-eV_{\mathrm{dc}}$): magnon absorption at ε_1 transfers chemical potential from a forward moving edge to a backwards moving edge — causing the particle current (I_{P} where $I_{\mathrm{P}} = -I/e$) to decrease. Conversely, magnon absorption at ε_2 transfers chemical potential from a backward moving edge to a forward moving edge, increasing I_{P}. (Right panel) $\mu \leq -E_{\mathrm{Z}}$: magnon absorption at ε_1 (ε_2) causes an increase (decrease) in $|-I_{\mathrm{P}}|$. **(D)** A summary of the effects of ε_1 and ε_2 at $\mu \geq E_{\mathrm{Z}}$ and $\mu \leq -E_{\mathrm{Z}}$. For $\mu \geq E_{\mathrm{Z}}$, ε_2 is closer to the magnon generation site, so the current change caused by ε_2 is predicted to be dominant and is circled in red. For $\mu \leq -E_{\mathrm{Z}}$, ε_1 is closer to the magnon generation site, so the current change caused by ε_1 is predicted to be dominant and is circled in red.

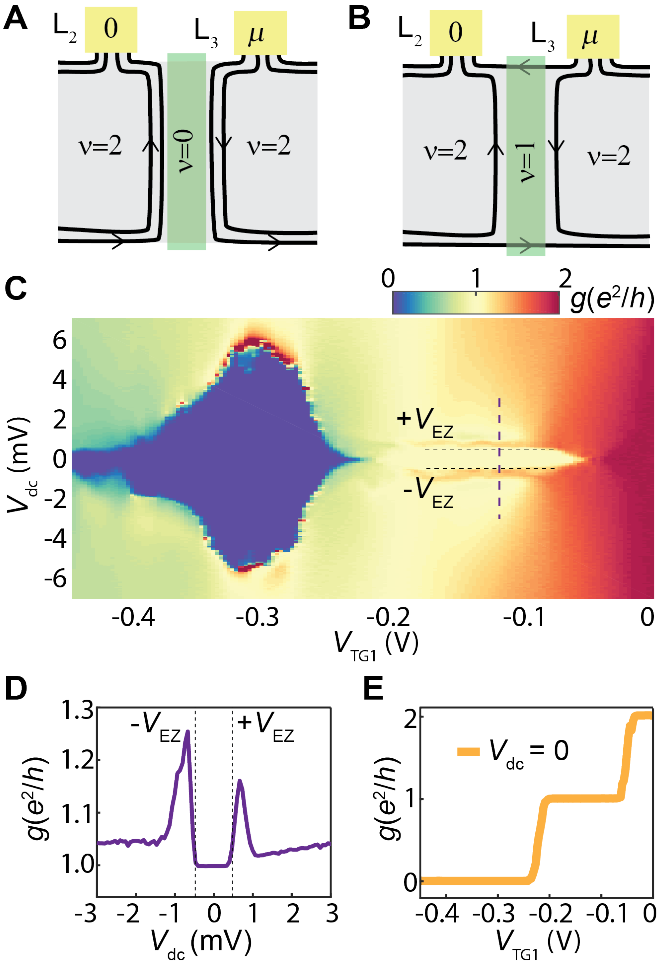

Figure B.6: **Comparison of the breakdown of $\nu = 0$ and $\nu = 1$ LLs as a function of density (device 2).** **(A)** The region under top gate 1 (TG1) is at $\nu_{\text{TG1}} = 0$ while outside regions, gated only by the back gate, are at $\nu_{\text{BG}} = 2$. **(B)** $\nu_{\text{TG1}} = 1$ and $\nu_{\text{BG}} = 2$. **(C)** Two-terminal conductance measurement at $B = 3$ T where a constant d.c. voltage (V_{dc}) and a 50 μV a.c. excitation voltage are applied to L$_3$ and the differential conductance (dI/dV) is measured through L$_2$. TG1 is swept from $\nu_{\text{TG1}} = 0$ to $\nu_{\text{TG1}} = 2$, and $\nu_B G = 2(V_B G = 1.8\text{V})$. The horizontal black dashed lines denote $\pm V_{\text{EZ}}$ and the location of the line cut taken in (D) is shown by the vertical purple dashed line.

Figure B.6: (Continued) The bias at which $\nu_{\mathrm{TG1}} = 0$ breaks down appears heavily dependent on the density under TG1 while the bias at which $\nu_{\mathrm{TG1}} = 1$ breaks down is relatively independent of the density under TG1, occurring at $\pm V_{\mathrm{EZ}}$ across the plateau. **(D)** The dependence of $\mathrm{d}I/\mathrm{d}V$ on V_{dc} shows a sharp increase at $\pm V_{\mathrm{EZ}}$. **(E)** The dependence of $\mathrm{d}I/\mathrm{d}V$ on ν_{TG1} at $V_{\mathrm{dc}} = 0$ shows well quantized quantum Hall plateaus at $\nu_{\mathrm{TG1}} = 0$, 1, and 2.

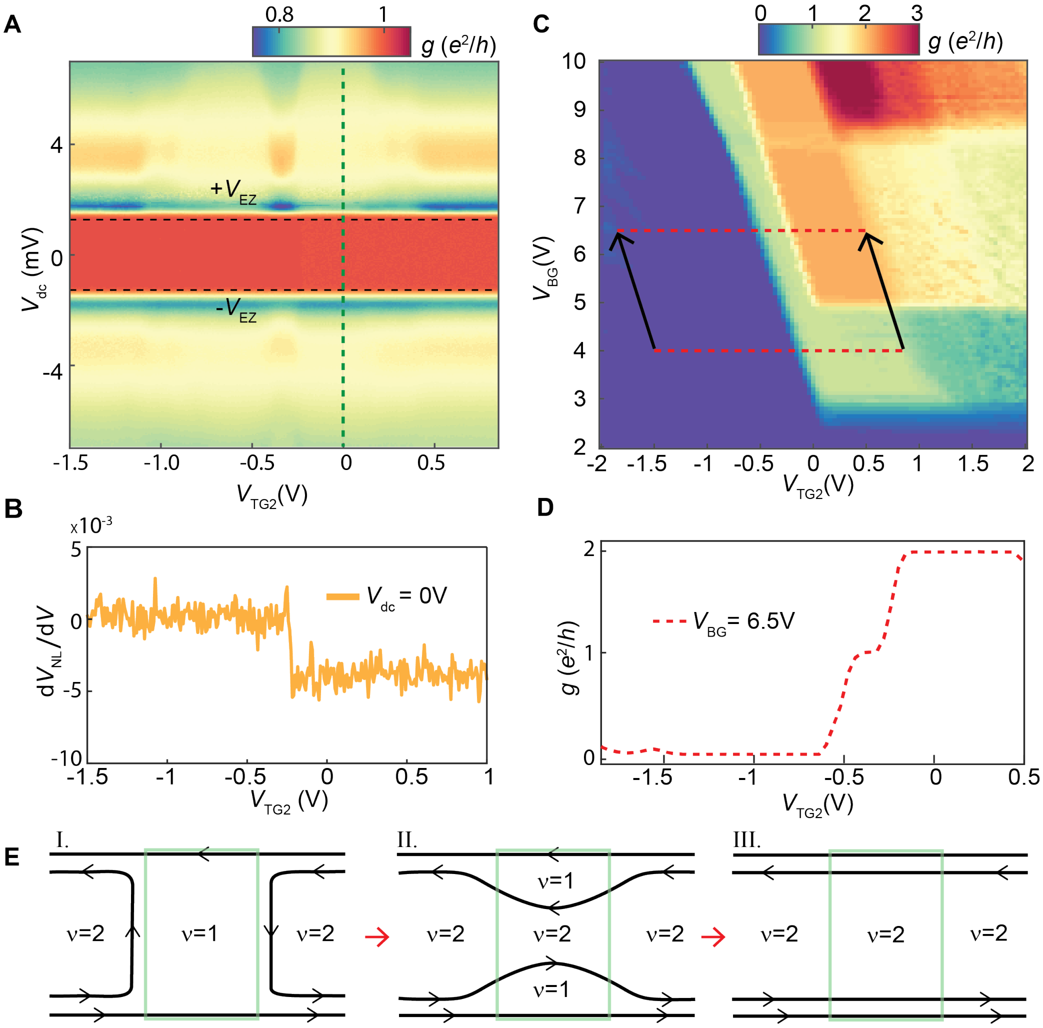

Figure B.7: **The conditions under which non-local voltage (S_{NL}) is measured.** **(A)** The conductance between L_3 and L_2 as a function of V_{dc} and V_{TG2} ($B = 8$ T). Horizontal dashed black lines indicate $\pm V_{\mathrm{EZ}}$. Vertical green dashed line is where the line cut in Fig. 4.5B is taken. We see a sharp drop in conductance when $|V_{\mathrm{dc}}| > V_{\mathrm{EZ}}$ due to magnon generation. This drop is largely unaffected when top gate 2 (TG2) is changed. Features at $|V_{\mathrm{dc}}| > V_{\mathrm{EZ}}$ coinciding with $\nu_{\mathrm{TG2}} = -1$ and $\nu_{\mathrm{TG2}} = 1$ indicate that magnons absorbed at the non-local voltage contacts affect the amount of magnons absorbed at the drain contact.

Figure B.7: (Continued) **(B)** S_{NL} is measured between L_4 and L_5 at $V_{\mathrm{dc}} = 0$, showing a small negative voltage when the top gate is tuned from $\nu = 0$ to $\nu = 1$. This indicates a small number of bulk carriers that give a resistance between the two contacts — a quantity which gives a small background to the S_{NL} signal, which can be subtracted out when calculating the value of S_{NL} when $|V_{\mathrm{dc}}| > V_{\mathrm{EZ}}$.**(C)** Two-terminal conductance measured between L_3 and L_2 as a function of the gate voltage on TG2 (V_{TG2}) and on the back gate (V_{BG}) ($V_{\mathrm{dc}} = 0$). The line cut in Fig. 4.5C (main text) is meant to show the corresponding filling factors under TG2 for the voltage range on the x-axis, with V_{BG} = 4V (bulk at $\nu = 1$). However, a line cut at V_{BG} = 4V does not show the transition between $\nu = 1$ and $\nu = 2$ because there is no equilibration between the $\nu = 1$ and $\nu = 2$ edges due to opposite spin polarization [31, 110]. We therefore use a line cut taken at V_{BG} = 6.5V ($\nu_{\mathrm{BG}} = 2$), where the step between $\nu = 1$ and $\nu = 2$ is clear, in order to estimate the steps in filling factor at V_{BG} = 4V. In order to account for the extra contribution in density due to the additional 2.5V applied by the back gate, we take the voltage interval of V_{TG2} at V_{BG} = 4V and shift it up by the slope of the hall plateaus (indicated by the black arrows pointing from the red-dashed line at 4V to the red-dashed line at 6.5V). **(D)** Conductance over the voltage range of V_{TG2} indicated by the red-dashed line in (C) at fixed V_{BG} = 6.5V.

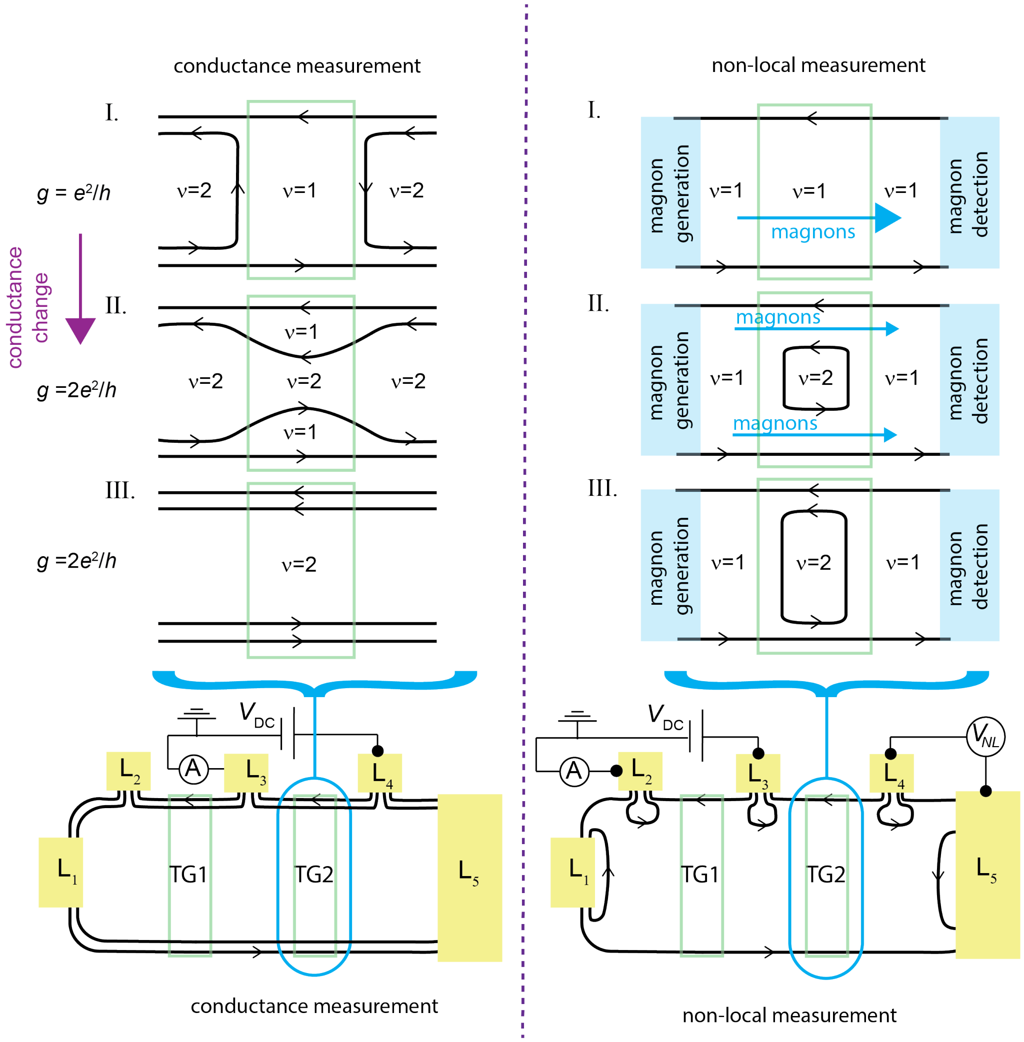

Figure B.7: **(E) Comparison of a two-terminal conductance measurement across a top gate (left) to a non-local magnon-transmission measurement across the same top gate(right), as the density in the top-gated region is tuned from $\nu = 1$ to $\nu = 2$.** Panel I: (left) the two edge states in the outer regions are not yet able to enter the top-gated $nu = 1$ region, resulting in a conductance of e^2/h. In the corresponding non-local measurement (right), magnons are able to propagate, yielding a non-local voltage.

Figure B.7: (Continued) Panel II: (left) As the density is increased further, the developing $\nu = 2$ region under the top gate connects with the outer $\nu = 2$ regions, changing the measured conductance to $2e^2/h$. However, some $\nu = 1$ regions under the top gate remain present. In the corresponding non-local measurement (right), these remaining $\nu = 1$ regions under the top gate still allow magnon transport. In the non-local measurements shown in Fig. 4.5C, we expect these regions to be responsible for the non-local voltage signal seen when the region under the top gate is transitioning from $\nu_{TG2} = 1$ to $\nu_{TG2} = 2$. Panel III: Once the density is increased sufficiently, the top-gated region consists almost entirely of $\nu = 2$, yielding a conductance of $2e^2/h$ and a near complete suppression of magnon transport in the non-local measurement.

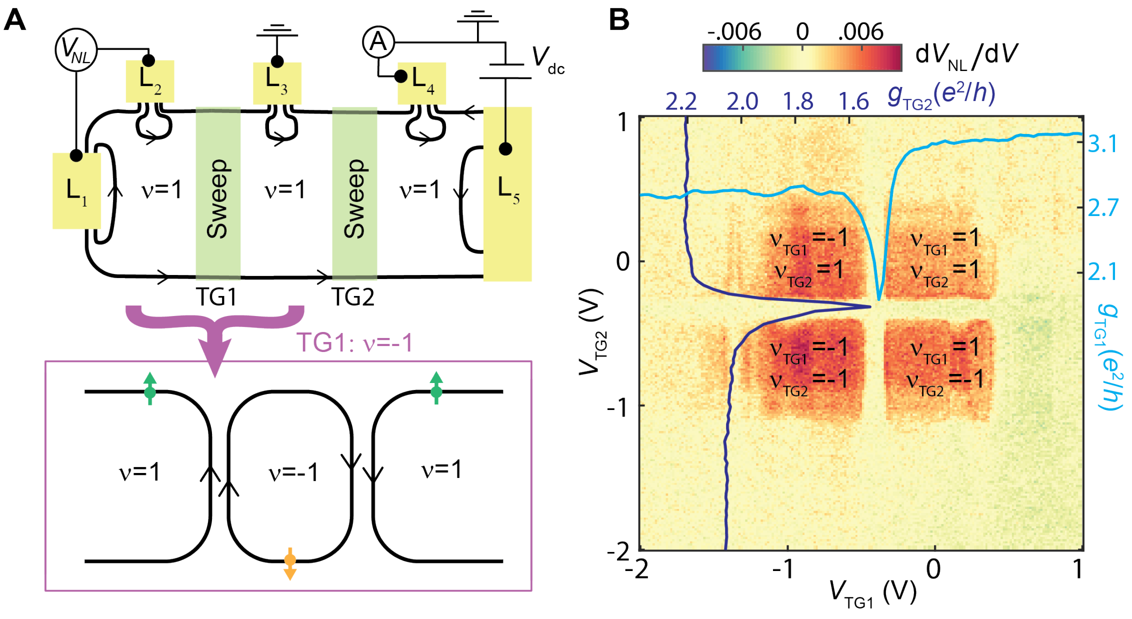

Figure B.8: **Dependence of S_{NL} on filling factors under TG1 and TG2. (A)** A circuit configuration for measuring a non-local voltage in device 2 (schematic). The filling factor under TG1 (ν_{TG1}) and under TG2 (ν_{TG2}) are both swept from -2 to 2, while the outside regions are maintained by a fixed back-gate voltage at ν_{BG} =1 (V_BG = 4V, B = 8 T). The bottom panel highlights the case of ν_{TG1}=-1: Edge states in both regions co-propagate along the boundary, but do not equilibrate because of their opposite spin-polarization [110]. **(B)** Setting $\mu > E_{\mathrm{Z}}$ (V_{DC} = -2.8 mV), and measuring S_{NL} between L_2 and L_1 we find strong non-local signals in four quadrants around $\nu = 0$. Strips where the signal is highly suppressed coincide with where the charge neutrality point occurs in density measurements of TG1 (TG2) at B = 0 T, shown by the superimposed light blue (dark blue) line cuts. We see similar signals in all four quadrants, indicating that magnons are not suppressed by the $\nu = -1$ regions.

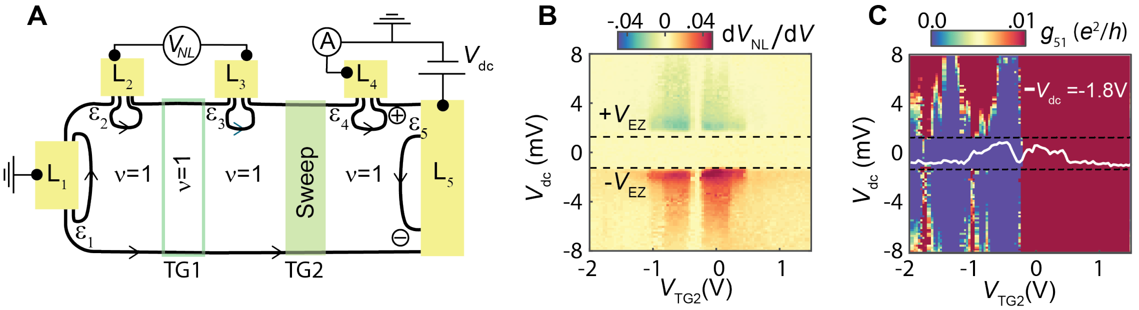

Figure B.9: **Absence of current leakage when spin transport is mediated by the $\nu = -1$ ferromagnet.** **(A)** A circuit used to measure S_{NL} in device 2, as well as a leakage current across TG2 when it is tuned to $\nu_{\mathrm{TG2}} = -1$ (schematic). $\nu_{\mathrm{TG1}} = 1$ for all measurements while ν_{TG2} is swept from -2 to 2. **(B)** Non-local voltage (S_{NL}) measured between L_3 and L_2 as a function of V_{dc} and V_{TG1}. Horizontal dashed black lines indicate $\pm V_{\mathrm{EZ}}$. We note a delay in the onset of the non-local signal for positive bias, which we tentatively attribute to the fact that the absorption of magnon generation for positive bias is far from both the non-local leads and is mostly absorbed at ε_5 and ε_4, with only enough magnons to generate a non-local signal at larger energies. **(C)** Conductance into L_1 with the color scale saturated. This measures the current not drained at L_4 due to the contact resistance R_{C}. Black dashed lines indicate $\pm V_{\mathrm{EZ}}$. White line cut is taken from the plot shown in (B) (over the same span of V_{TG1}) at fixed V_{dc} = -1.8mV, and overlaid onto the conductance map. When we see an increase in S_{NL} there is a negligible amount of leakage current ($g_{51} < 0.01\ e^2/h$) measured at L_1. Additionally, when we see an increase in the leakage current ($g_{51} > 0.01\ e^2/h$), there is no corresponding effect on S_{NL}. This is expected because an edge current should bring L_3 and L_2 to the same chemical potential. From this we conclude that the S_{NL} we measure is not due to leakage current.

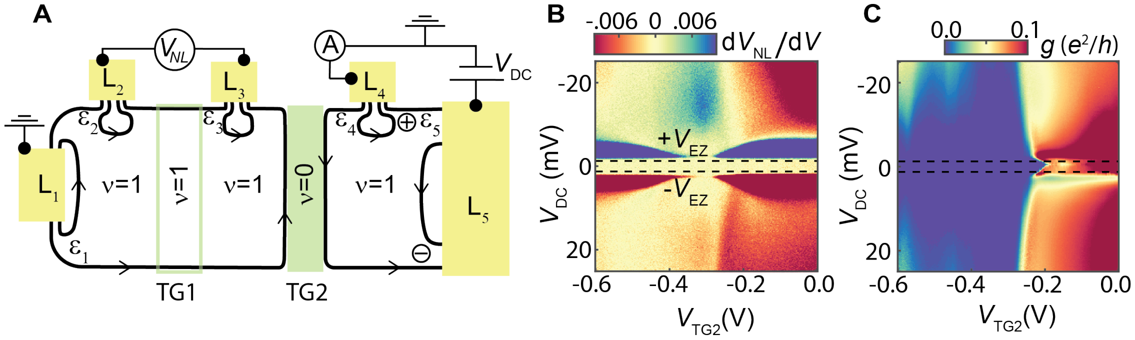

Figure B.10: **Absence of current leakage when spin transport is mediated by the $\nu = 0$ CAF. (A)** The circuit used to measure S_{NL} in device 2 across a $\nu = 0$ region (schematic). L_1 is grounded in order to measure the amount of residual charge that leaks through to the other side of $\nu_{\mathrm{TG2}} = 0$. **(B)** When magnons are generated in the ν_{BG}, $\nu_{\mathrm{TG1}} = 1$ region and $\nu_{\mathrm{TG2}} = 0$, we see an onset of S_{NL} at energies exceeding $\pm V_{\mathrm{EZ}}$. This indicates that higher energy magnons have overcome the interface barriers and have propagated through the $\nu_{\mathrm{TG2}} = 0$ region. At more positive gate voltages, we see the effects of the residual current on S_{NL} (due to the finite contact resistance of L_4) which passes through when $\nu_{\mathrm{TG2}} > 0$. We observe that these effects disappear once $\nu_{\mathrm{TG2}} > 0$ and do not play a role in the S_{NL} signal measured in this region. **(C)** Residual current measured at L_1 indicating that residual leakage does not correlate with the appearance of the $\nu_{\mathrm{TG2}} = 0$ signal.

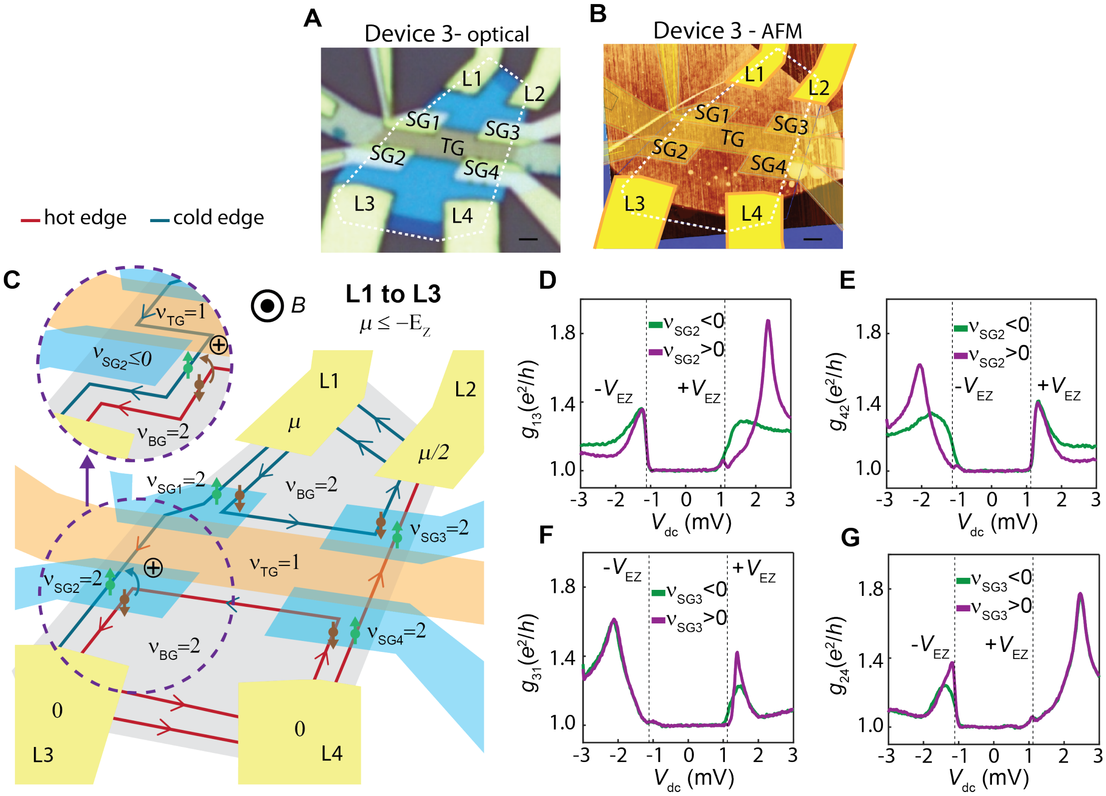

Figure B.11: **Verifying positive and negative bias magnon generation locations (device 3).** **(A)** Optical micrograph of device 3. The outline of the graphene is shown by the dotted white line, and the scale bar is 1 μm. For this device, an extra BN dielectric (10nm) was used between the top gates and side gates to electrically isolate them. There are 4 leads (L_1-L_4), one top gate (TG), and four side gates (SG1 - SG4). **(B)** AFM image of device 3. **(C)** Schematic of device 3 depicting a two-terminal conductance measurement between L_1 (source) and L_3 (drain) with L_2 and L_4 floating. The leads are yellow, the top gate (TG) is orange and the side gates are light blue. The regions outside of the top-gated region (including the side gates) are tuned to $\nu = 2$ and the region under the top gated region is tuned to $\nu = 1$.

Figure B.11: (Continued) Chiral edge states are shown by the lines with arrows and edges with higher (lower) chemical potential are colored red (blue) and labeled hot (cold). The side gates can be used to push the edge states away from the physical edge of the device (as illustrated in the inset, for SG2). **(D)** Two-terminal conductance measurement at $B = 7$ T where a constant d.c. voltage (V_{dc}) and a 50 μV a.c. excitation voltage are applied to L_1 (source) and the differential conductance ($\mathrm{d}I/\mathrm{d}V$) is measured through L_3 (drain). Magnons are generated when a spin-down hot edge meets a spin-up cold edge at E_{Z}. For this configuration, we expect magnons to be generated under SG2 for positive V_{dc} only. When we reach $+V_{\mathrm{EZ}}$ we see a change in the conductance while at $-V_{\mathrm{EZ}}$ we see almost no change, as expected. **(E-G)** Similar analysis for different lead configurations shows magnons are generated in accordance with our model predictions. The effect of SG2 is stronger than SG3 for unknown reasons. The exact change in conductance is difficult to predict because we are changing both the nature of scattering between the two edge states [110] as well as the distance between magnon generation and absorption, so here we note only qualitative changes.

Appendix C

Fabrication of encapsulated graphene devices

C.1 Making encapsulated graphene/hBN stacks

C.1.1 Hexagonal boron nitride

All of the experiments in this thesis use devices made from graphene encapsulated in hexagonal boron nitride (hBN), which is a hexagonal lattice much like graphene but with boron and nitrogen atoms in the place of carbon. Whereas the sublattice symmetry of the graphene lattice leads to a linear Dirac dispersion, the asymmetry of the sublattices in hBN causes a band gap of 6 eV to open, making it an insulator [124]. One of the most significant fabrication breakthroughs in the field came from Dean *et al.* in 2010 when it was discovered that using h-BN as a substrate for graphene led to much higher quality devices [125]. Prior to this, people generally used the SiO_2

substrate that was used to exfoliate the graphene [126, 127], or suspended graphene [128, 129]. Although suspending graphene also leads to quite good device quality, it is also quite fragile and complicated device geometries with more than 2 leads becomes quite difficult.

C.1.2 Exfoliation of layered materials

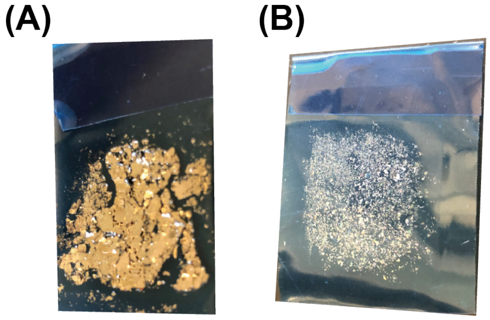

Figure C.1: **Blue exfoliation tip used to cleave layered materials to deposit on substrate**. **(A)** A layer of graphite cleaved off of a bulk piece of graphite. **(B)** Small crystals of boron nitride that have been broken up onto blue tape.

Exfoliation is a simple method of extracting a single monolayer of material from any van der Waals material [130], and was first used to find monolayers of graphene from bulk graphite by Geim and Novoselov [5]. Our version of this is detailed here:

- Prepare a clean SiO_2/Si (about 2 cm x 2 cm) substrate using an O_2 plasma cleaning process (RIE-8) and 350 °C clean in the RTP-2.
- Press a piece of blue tape (1009R from Ultron Systems) down onto a bulk piece of graphite and peel off a thick layer of graphite. For Boron Nitride, use a small

starter crystal and break it up by pressing the tape together multiple times until it covers a dense chip-sized area. Example tapes are shown in Fig. C.1.

- Thin down the graphite or hBN by combining with a fresh piece of tape and then peeling the two pieces apart. Do this 3-4 times.
- Peel off a layer of tape and then press down onto a freshly cleaned SiO_2/Si chip. You should see small pieces of graphite left behind with your naked eye.

After exfoliation, one must locate flakes of the desired size, thickness, and geometry in an optical microscope. Fig. C.2 shows examples of flakes located with 100x magnification in the optical microscope with layers of varying thickness.

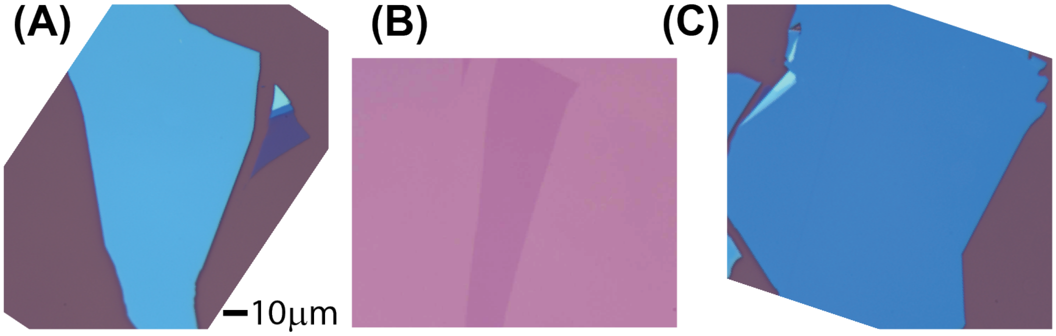

Figure C.2: **Flakes of hBN and graphene used to make a layered heterostructure.** **(A)** Top hBN flake **(B)** Monolayer graphene to be sandwiched between two hBN flakes.**(C)** Bottom hBN flake.

C.1.3 Transferring with PC

We use a dry transfer method that we learned from references [131] and [114], as well as from instruction from Joel Wang and Javier Sanchez-Yamagishi at MIT. This procedure is outlined below, using the transfer setup in the Kim lab at Harvard:

- Prepare transfer slide
  - Dissolve PC Poly(Bisphenol A carbonate) crystals in Chloroform. Use 6% by weight. This can be re-used for future transfer slides.
  - Using a pipette, drop about 5 drops of PC along the legnth of a clean microscope slide. Press a second clean glass slide directly on top of the first slide, pressing the PC into a uniform film between the two slides. Immediately separate by sliding the two slides away from each other.
  - Let the PC film harden in air for 15 minutes
  - Cut out a 1 cm x 1 cm square of PDMS from a pre-made or purchased PDMS block that is about 2mm thick.
  - Assemble the transfer slide by first sticking the PDMS block onto the end of the glass slide. Then cut out a square of PC about the same size as the PDMS block and use a sharp set of tweezers to peel it off the glass and stick it to the PDMS. If you get a lot of wrinkles in the PC, you can heat up the glass slide + PDMS + PC to 80°C for 5 minutes and the wrinkles should smooth out.
- Picking up hBN/graphene with PC

  - Mount the glass slide in the micromanipulator with the PDMS/PC stack facing down.
  - Place chip with exfoliated flakes down onto vacuum chuck and heat up to 30 °C
  - Locate the flake that you would like to pick-up and move and move your PDMS/PC so that the flake is in the middle of the PDMS/PC stack when you look through the microscope. Bring the PC into contact with the Silicon chip. The micromanipulator should already be set at an angle, so that when the PC comes into contact with the Silicon chip it only contacts an edge of the PC square. You should be able to optically see it come into contact with the chip, and see the PC wavefront.
  - Lower the PDMS/PC stack using the top knob on the micromanipulator and come as close to your flake as you can (usually around 20 um away). Turn up the temperature to 120 °C and wait for the wavefront to cover the flake.
  - After your flake is completely covered, cool back down to 30 °C.
  - Slowly bring the PDMS/PC stack up using the micromanipulator and hopefully you should see your flake come up off of the Silicon chip.
  - Pick up the next flake using the already picked-up flake.
- Place stack down on desired substrate and heat up to 180 °C to melt off the PC onto the substrate.
- Dissolve the PC in chloroform for 5 minutes, then dip into IPA. Blow dry the

chip with nitrogen.

After the stack is made, image with an AFM to identify clean areas without too much trapped contamination, in the form of bubbles [132], as shown in Fig. C.3. Unfortunately, some stacks may have too many bubbles to be usable.

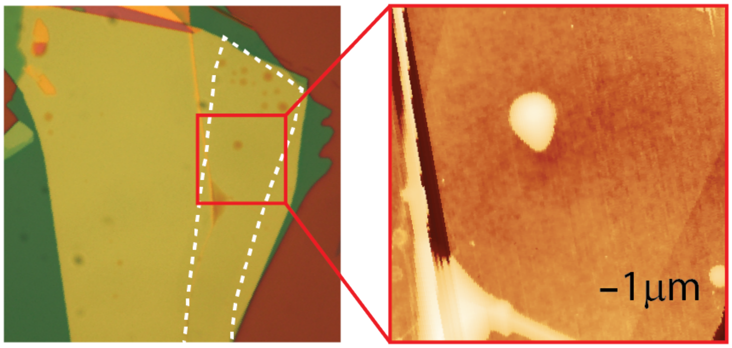

Figure C.3: **Optical and AFM image of a hBN/graphene/hBN heterostructure.** The left image shows an 100x optical image after encapsulating graphene with hBN and dissolving the PC polymer in chloroform. The graphene is outlined in white. Dark spot are where bubbles have formed inside of the heterostructure. The right image in the shows an AFM image over the region shown in the red box in the optical image. The edges of the graphene can clearly be seen in the hBN/graphene/hBN stack. A large wrinkle can be seen on the left side, as well as a large bubble in the middle of the image; we try to avoid these types of imperfections when designing our device.

C.2 Fabrication of gated graphene devices

C.2.1 Fabricating Au top gates

Boron Nitride can also be used as a gate dielectric, allowing for easy gating of encapsulated devices by local top gates. The devices are typically placed on a SiO_2/Si chip, where the Silicon can act as a global gate for the device. Local gates can be made by adding a graphite layer to the stack, or by patterning on Cr/Au gates as described below:

- Spin 950 A2 PMMA at 4000 RPM (Gives about 70 nm of PMMA).
- Ebeam lithography (Elionix-7000): Write top gate using 1nA beam current, and a dose of 3000 μC/cm^2. Develop in an ice-cold solution of H_2O:IPA (1:3 by weight).
- Using a thermal evaporator, evaporate 3 nm of Cr and 20 nm of Au for the gate.

C.2.2 Etching using an HSQ/PMMA etch mask

Typically the device is designed such that only pristine areas are included in the device geometry. This is done by etching the stack with a reactive ion etching process. We use an HSQ/PMMA bilayer because the HSQ is very resistant to the CHF_3 and O_2 etch, and the PMMA layer is easy to wash away:

- Spin 950 PMMA A4 at 4000 RPM (~200 nm of resist). Bake at 180 °C for 10 minutes. Let it cool for 1 minute.

- Warm up bottle of FOX for 30 minutes. Spin HSQ (FOX) at 4000 RPM. Bake at 180 °C for 2 minutes.
- Ebeam lithography (Elionix-7000): Write etch mask using 1nA beam current, and a dose of 1200 μC/cm^2.
- Develop with 25% TMAH for 17 seconds. TMAH is dangerous and can kill you.
- Rinse with DI water and dry with nitrogen.
- Etch in an inductively coupled pfdelasma etching system (RIE-8 in the Harvard cleanroom) with O_2 Oxygen plasma (15sccm), 70W on the Coil, and 10W on the Platen, at 20 °C to get rid of PMMA.
- Etch in an inductively coupled plasma etching system (RIE-8 in the Harvard cleanroom) with a mixture of O_2 (5sccm), CHF_3 (10sccm) and Ar (10sccm), 30W on the Coil, and 10W on the Platen, at 20 °C, until color change indicates that the stack has been etched all the way through. This etch recipe etches BN at about 1nm/sec.

C.2.3 1-D edge contacts

After the geometry of the device has been defined, one needs to then make contact to the device. Because the sample is encapsulated with BN, these contacts need to come in from the sides, and are effectively 1-D edge contacts [114]. Here is the procedure used in the Harvard cleanroom:

- Spin 450 A8 PMMA at 4000 RPM (Gives about 700 nm of PMMA).

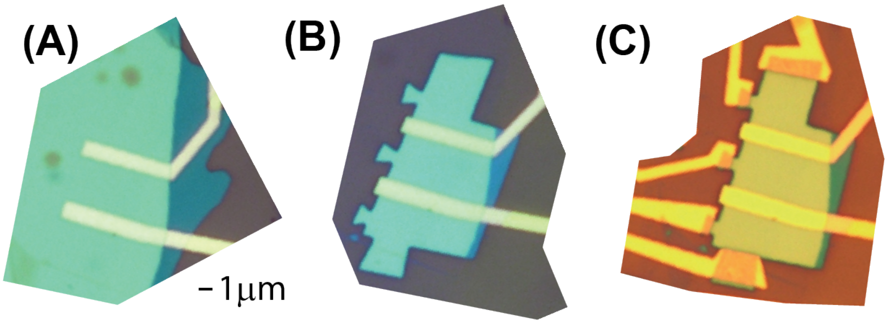

Figure C.4: **Fabrication steps used to making a typical device used for electron transport.** (**A**) Chrome/Gold (Cr/Au) top gates that have been patterned on to locally gate the device. (**B**) After writing an HSQ/PMMA etch mask, the device is etched into the desired geometry using a reactive ion etcher. (**C**) Cr/Au leads are patterned on to make electrical contact to the device.

- Ebeam lithography (Elionix-7000): Write contacts using 1nA beam current, and a dose of 3000 μC/cm^2. Develop in an ice-cooled solution of H_2O:IPA (1:3 by weight).
- Use a thermal evaporator with a tilted rotation stage. Set the tilt to approximately 15° and evaporate 10 nm of Cr and 3x the height of the stack in Au while continuously rotating the device.

Bibliography

[1] E. H. Hall, "On a New Action of the Magnet on Electric Currents," *American Journal of Mathematics*, vol. 2, no. 3, pp. 287–292, 1879. 1, 2.1.1

[2] K. von Klitzing, G. Dorda, and M. Pepper, "New Method for High-Accuracy Determination of the Fine-Structure Constant Based on Quantized Hall Resistance," *Physical Review Letters*, vol. 45, no. 6, pp. 494–497, 1980. 1, 2.1.1, 2.2

[3] S. M. Girvin, "The Quantum Hall Effect : Novel Excitations and Broken Symmetries," in *Les Houches Lecture Notes, in: Topological Aspects of Low Dimensional Systems* (A. Comtet, T. Jolicœur, S. Ouvry, and F. David, eds.), no. vol 69, pp. 53–175, Springer-Verlag, 1999. 1, 2.3, 2.3, 4.1.2, 4.2

[4] H. L. Stormer, "Nobel Lecture: The fractional quantum Hall effect," *Reviews of Modern Physics*, vol. 71, no. 4, pp. 875–889, 2002. 1

[5] K. Novoselov, A. Geim, S. Morozov, D. Jiang, Y. Zhang, S. Dubonos, I. Grigorieva, and A. Firsov, "Electric Field Effect in Atomically Thin Carbon Films," *Science*, vol. 306, pp. 666–669, 2004. 1, C.1.2

[6] K. S. Novoselov, A. K. Geim, S. V. Morozov, D. Jiang, M. I. Katsnelson, I. V. Grigorieva, S. V. Dubonos, and A. A. Firsov, "Two-dimensional gas of massless Dirac fermions in graphene.," *Nature*, vol. 438, no. 7065, pp. 197–200, 2005. 1

[7] Y. Zhang, Y.-W. Tan, H. L. Stormer, and P. Kim, "Experimental observation of the quantum Hall effect and Berry's phase in graphene.," *Nature*, vol. 438, no. November, pp. 201–204, 2005. 1, A.2

[8] A. K. Geim and K. S. Novoselov, "The rise of graphene.," *Nature materials*, vol. 6, no. 3, pp. 183–191, 2007. 2.1.1

[9] H. L. Stormer, R. Dingle, A. Gossard, W. Wiegmann, and M. Sturge, "Two-Dimensional Electron Gas at a Semiconductor - Semiconductor Interface," *Solid State Communications*, vol. 29, pp. 705–709, 1979. 2.1.1

[10] B. I. Halperin, "Quantized hall conductance, current-carrying edge states, and the existence of extended states in a two-dimensional disordered potential," *Phys. Rev. B*, vol. 25, pp. 2185–2190, Feb 1982. 2.1.2

[11] S. Datta, *Electronic Transport in Mesoscopic Systems.* Cambridge Univ. Press, 1995. 2.1.2, 3.1.1

[12] U. Klaβ, W. Dietsche, K. V. Klitzing, and K. Ploog, "Imaging of the dissipation in quantum-Hall-effect experiments," vol. 354, pp. 351–354, 1991. 2.1.2, 2.5

[13] M. Büttiker, "Absence of backscattering in the quantum hall effect in multiprobe conductors," *Phys. Rev. B*, vol. 38, pp. 9375–9389, Nov 1988. 2.1.2

[14] Y. Zhang, Z. Jiang, J. P. Small, M. S. Purewal, Y.-W. Tan, M. Fazlollahi, J. D. Chudow, J. A. Jaszczak, H. L. Stormer, and P. Kim, "Landau-level splitting in graphene in high magnetic fields," *Phys. Rev. Lett.*, vol. 96, p. 136806, Apr 2006. 2.3, 2.3

[15] A. Usher, R. Nicholas, J. Harris, and C. Foxon, "Observation of magnetic excitons and spin waves in activation studies of a two-dimensional electron gas," *Physical Review B*, vol. 41, no. 2, pp. 1129–1134, 1990. 2.3

[16] R. J. Nicholas, R. J. Haug, and K. v. Klitzing, "Exchange enhancement of the spin splitting in a GaAs-Ga(x)A1(l-x)As heterojunction," *Phys. Rev. B*, vol. 37, no. 3, pp. 1294–1302, 1988. 2.3

[17] J. Alicea and M. P. A. Fisher, "Graphene integer quantum Hall effect in the ferromagnetic and paramagnetic regimes," *Physical Review B*, vol. 74, p. 075422, 2006. 2.3

[18] K. Yang, S. Das Sarma, and A. H. MacDonald, "Collective modes and skyrmion excitations in graphene SU (4) quantum Hall ferromagnets," *Physical Review B*, vol. 74, no. 7, p. 075423, 2006. 2.3

[19] K. Nomura and A. H. Macdonald, "Quantum Hall ferromagnetism in graphene," *Phys. Rev. Lett.*, vol. 96, p. 256602, 2008. 2.3

[20] M. Goerbig, "Electronic properties of graphene in a strong magnetic field," *Reviews of Modern Physics*, vol. 83, pp. 1193–1243, 2011. 2.3

[21] J. Jung and A. H. MacDonald, "Theory of the magnetic-field-induced insulator in neutral graphene sheets," *Physical Review B*, vol. 80, no. 23, p. 235417, 2009. 2.3, B.6

[22] M. Kharitonov, "Phase diagram for the $\nu = 0$ quantum hall state in monolayer graphene," *Phys. Rev. B*, vol. 85, p. 155439, Apr 2012. 2.3, 3.3, 4.1.4, 4.2.3, B.6

[23] A. F. Young, C. R. Dean, L. Wang, H. Ren, P. Cadden-Zimansky, K. Watanabe, T. Taniguchi, J. Hone, K. L. Shepard, and P. Kim, “Spin and valley quantum Hall ferromagnetism in graphene,” *Nature Physics*, vol. 8, no. 7, pp. 550–556, 2012. 2.3, 2.11, 2.3, 3.1.3, 4.1.2, 4.1.4, 4.2.1

[24] J. G. Checkelsky, L. Li, and N. P. Ong, “Zero-Energy State in Graphene in a High Magnetic Field,” *Physical Review Letters*, vol. 100, no. 20, p. 206801, 2008. 2.3

[25] A. F. Young, J. D. Sanchez-Yamagishi, B. Hunt, S. H. Choi, K. Watanabe, T. Taniguchi, R. C. Ashoori, and P. Jarillo-Herrero, “Tunable symmetry breaking and helical edge transport in a graphene quantum spin Hall state.,” *Nature*, vol. 505, pp. 528–32, 2014. 2.3, 3.3, 4.1.4, 4.3, B.6

[26] R. J. Haug, “Edge-state transport and its experimental consequences in high magnetic fields,” *Semiconductor Science and Technology*, vol. 8, pp. 131–153, 1993. 2.4

[27] S. Komiyama and H. Nii, “Nonequilibrium electron distribution and nonlocal resistance in a two-dimensional electron gas at high magnetic fields,” *Physica B*, vol. 184, pp. 7–16, 1993. 2.4

[28] B. J. Van Wees, L. P. Kouwenhoven, E. M. M. Willems, C. J. P. M. Harmans, J. E. Mooij, H. Van Houten, C. W. J. Beenakker, J. G. Williamson, and C. T. Foxon, “Quantum ballistic and adiabatic electron transport studied with quantum point contacts,” *Physical Review B*, vol. 43, no. 15, pp. 12431–12453, 1991. 2.4, B.2

[29] B. W. Alphenaar, P. L. McEuen, R. G. Wheeler, and R. N. Sacks, “Selective equilibration among the current-carrying states in the quantum hall regime,” *Physical Review Letters*, vol. 64, no. 6, pp. 677–680, 1990. 2.4, B.2

[30] G. Müller, D. Weiss, A. V. Khaetskii, K. von Klitzing, S. Koch, H. Nickel, W. Schlapp, and R. Lösch, “Equilibration length of electrons in spin-polarized edge channels,” *Phys. Rev. B*, vol. 45, pp. 3932–3935, Feb 1992. 2.4, B.2

[31] F. Amet, J. R. Williams, K. Watanabe, T. Taniguchi, and D. Goldhaber-Gordon, “Selective equilibration of spin-polarized quantum Hall edge states in graphene,” *Phys. Rev. Lett.*, vol. 112, p. 196601, May 2014. 2.4, 3.1.3, 3.2.1, 3.2.5, 3.3, 4.1.4, 4.2.1, A.3.4, B.2, B.7

[32] T. Young, “Experimental demonstration of the general law of the interference of light,” *Phil. Trans. R. Soc. Lond.*, vol. 94, pp. 1–16, 1804. 3.1

[33] A. A. Michelson and E. W. Morley, "On the Relative Motion of the Earth and the Luminiferous Ether," *The American Journal of Science*, vol. 34, pp. 333–345, 1887. 3.1

[34] B. Abbott-et.al., "Observation of gravitational waves from a binary black hole merger," *Physical Review Letters*, vol. 116, p. 061102, 2016. 3.1

[35] G. Haack, H. Förster, and M. Büttiker, "Parity detection and entanglement with a Mach-Zehnder interferometer," *Physical Review B - Condensed Matter and Materials Physics*, vol. 82, p. 155303, 2010. 3.1

[36] E. Hecht, *Optics*. Addison Wesley, 2002. 3.1, 3.1

[37] A. Yacoby, U. Sivan, C. Umbach, and J. Hong, "Interference and Dephasing by Electron-Electron Interaction on Length Scales Shorter than the Elastic Mean Free Path," *Physical Review*, vol. 66, no. 14, pp. 1938–1942, 1991. 3.1.1

[38] C. C. Chamon, D. E. Freed, S. A. Kivelson, S. L. Sondhi, and X. G. Wen, "Two point-contact interferometer for quantum Hall systems," *Phys. Rev. B*, vol. 55, pp. 2331–2343, Jan 1997. 3.2, 3.1.1

[39] Y. Ji, Y. Chung, D. Sprinzak, M. Heiblum, and D. Mahalu, "An electronic Mach-Zehnder interferometer," *Nature*, vol. 422, no. 8, pp. 415–418, 2003. 3.2, 3.1.1, 3.2.3

[40] D. E. Feldman and A. Kitaev, "Detecting non-abelian statistics with an electronic Mach-Zehnder interferometer," *Phys. Rev. Lett.*, vol. 97, p. 186803, Nov 2006. 3.1.1, 3.1.2

[41] I. Neder, M. Heiblum, Y. Levinson, D. Mahalu, and V. Umansky, "Unexpected behavior in a two-path electron interferometer," *Physical Review Letters*, vol. 96, no. 1, pp. 1–4, 2006. 3.1.1, 3.1.3, 3.2.3

[42] P. Roulleau, F. Portier, D. C. Glattli, P. Roche, A. Cavanna, G. Faini, U. Gennser, and D. Mailly, "Finite bias visibility of the electronic Mach-Zehnder interferometer," *Physical Review B*, vol. 76, no. 16, p. 161309, 2007. 3.1.1, 3.1.3, 3.2.3

[43] B. J. Van Wees, H. Van Houten, C. W. J. Beenakker, J. G. Williamson, L. P. Kouwenhoven, D. Van Der Marel, and C. T. Foxon, "Quantized conductance of point contacts in a two-dimensional electron gas," *Physical Review Letters*, vol. 60, no. 9, pp. 848–850, 1988. 3.1.1

[44] Y. Aharonov and D. Bohm, "Significance of electromagnetic potentials in the quantum theory," *Phys. Rev.*, vol. 115, pp. 485–491, Aug 1959. 3.1.2

[45] B. I. Halperin, A. Stern, I. Neder, and B. Rosenow, “Theory of the fabry-pérot quantum hall interferometer,” *Phys. Rev. B*, vol. 83, p. 155440, Apr 2011. 3.1.2

[46] D. McClure, *Interferometer-Based Studies of Quantum Hall Phenomena.* PhD thesis, 2012. 3.1.2, 3.1.2

[47] K. T. Law, D. E. Feldman, and Y. Gefen, “Electronic Mach-Zehnder interferometer as a tool to probe fractional statistics,” *Phys. Rev. B*, vol. 74, p. 045319, Jul 2006. 3.1.2

[48] F. E. Camino, W. Zhou, and V. J. Goldman, “e/3 Laughlin quasiparticle primary-filling ν=1/3 interferometer,” *Physical Review Letters*, vol. 98, p. 076805, 2007. 3.1.2

[49] N. Ofek, A. Bid, M. Heiblum, A. Stern, V. Umansky, and D. Mahalu, “Role of interactions in an electronic Fabry-Perot interferometer operating in the quantum Hall effect regime.,” *Proceedings of the National Academy of Sciences of the United States of America*, vol. 107, p. 5276, 2010. 3.1.2

[50] R. L. Willett, L. N. Pfeiffer, and K. W. West, “Alternation and interchange of e/4 and e/2 period interference oscillations consistent with filling factor 5/2 non-Abelian quasiparticles,” *Physical Review B - Condensed Matter and Materials Physics*, vol. 82, p. 205301, 2010. 3.1.2

[51] D. T. McClure, W. Chang, C. M. Marcus, L. N. Pfeiffer, and K. W. West, “Fabry-Perot interferometry with fractional charges,” *Physical Review Letters*, vol. 108, p. 256804, 2012. 3.1.2

[52] J. Nakamura, S. Fallahi, H. Sahasrabudhe, R. Rahman, S. Liang, G. C. Gardner, and M. J. Manfra, “Aharonov–bohm interference of fractional quantum hall edge modes,” *Nature Physics*, 2019. 3.1.2

[53] S. Nakaharai, J. R. Williams, and C. M. Marcus, “Gate-defined graphene quantum point contact in the quantum hall regime,” *Physical Review Letters*, vol. 107, p. 036602, 2011. 3.1.3

[54] K. Zimmermann, A. Jordan, F. Gay, K. Watanabe, T. Taniguchi, Z. Han, V. Bouchiat, H. Sellier, and B. Sacépé, “Tunable transmission of quantum Hall edge channels with full degeneracy lifting in split-gated graphene devices,” *Nature Communications*, vol. 8, p. 14983, 2017. 3.1.3

[55] I. Neder, N. Ofek, Y. Chung, M. Heiblum, D. Mahalu, and V. Umansky, “Interference between two indistinguishable electrons from independent sources.,” *Nature*, vol. 448, no. 7151, pp. 333–337, 2007. 3.1.3

[56] E. Bieri, M. Weiss, O. Göktas, M. Hauser, C. Schönenberger, and S. Oberholzer, "Finite-bias visibility dependence in an electronic Mach-Zehnder interferometer," *Phys. Rev. B*, vol. 79, p. 245324, Jun 2009. 3.1.3, 3.2.3, A.4

[57] D. A. Abanin and L. S. Levitov, "Quantized transport in graphene p-n junctions in a magnetic field.," *Science*, vol. 317, no. 5838, pp. 641–643, 2007. 3.1.3

[58] J. R. Williams, L. Dicarlo, and C. M. Marcus, "Quantum Hall effect in a gate-controlled p-n junction of graphene," *Science*, vol. 317, no. August, pp. 638–640, 2007. 3.1.3, 3.3, 4.2.1, B.2

[59] A. H. Castro Neto, F. Guinea, N. M. R. Peres, K. S. Novoselov, and A. K. Geim, "The electronic properties of graphene," *Rev. Mod. Phys.*, vol. 81, pp. 109–162, Jan 2009. 3.1.3

[60] A. A. Zibrov, C. Kometter, H. Zhou, E. M. Spanton, T. Taniguchi, K. Watanabe, M. P. Zaletel, and A. F. Young, "Tunable interacting composite fermion phases in a half-filled bilayer-graphene Landau level," *Nature*, vol. 549, pp. 360–364, 2017. 3.1.3

[61] J. Tworzydło, I. Snyman, A. R. Akhmerov, and C. W. J. Beenakker, "Valley-isospin dependence of the quantum Hall effect in a graphene *p-n* junction," *Phys. Rev. B*, vol. 76, p. 035411, Jul 2007. 3.1.3

[62] B. Özyilmaz, P. Jarillo-Herrero, D. Efetov, D. A. Abanin, L. S. Levitov, and P. Kim, "Electronic transport and quantum Hall effect in bipolar graphene p-n-p junctions," *Phys. Rev. Lett.*, vol. 99, no. October, p. 166804, 2007. 3.1.3, 4.2.1, B.2

[63] J. Velasco, G. Liu, W. Bao, and C. Ning Lau, "Electrical transport in high-quality graphene pnp junctions," *New Journal of Physics*, vol. 11, p. 095008, sep 2009. 3.1.3

[64] S. Matsuo, S. Takeshita, T. Tanaka, S. Nakaharai, K. Tsukagoshi, T. Moriyama, T. Ono, and K. Kobayashi, "Edge mixing dynamics in graphene p-n junctions in the quantum Hall regime," *Nature Communications*, vol. 6, p. 8066, 2015. 3.1.3

[65] T. Machida, S. Morikawa, S. Masubuchi, R. Moriya, M. Arai, K. Watanabe, and T. Taniguchi, "Edge-channel transport of Dirac fermions in graphene quantum Hall junctions," *Journal of the Physical Society of Japan*, vol. 84, no. 12, pp. 1–9, 2015. 3.1.3

[66] E. Tovari, P. Makk, M.-H. Liu, P. Rickhaus, Z. Kovacs-Krausz, K. Richter, C. Schonenberger, and S. Csonka, "Gate-controlled conductance enhancement

from quantum Hall channels along graphene p-n junctions," *Nanoscale*, vol. 8, pp. 19910–19916, 2016. 3.1.3

[67] N. N. Klimov, S. T. Le, J. Yan, P. Agnihotri, E. Comfort, J. U. Lee, D. B. Newell, and C. A. Richter, "Edge-state transport in graphene $p-n$ junctions in the quantum hall regime," *Phys. Rev. B*, vol. 92, p. 241301, Dec 2015. 3.2.1

[68] J. R. Williams and C. M. Marcus, "Snake states along graphene *p-n* junctions," *Phys. Rev. Lett.*, vol. 107, p. 046602, Jul 2011. 3.2.1

[69] P. Rickhaus, P. Makk, M.-H. Liu, E. Tóvári, M. Weiss, R. Maurand, K. Richter, and C. Schönenberger, "Snake trajectories in ultraclean graphene pn junctions," *Nature Communications*, vol. 6, p. 6470, 2015. 3.2.1

[70] T. Taychatanapat, J. Y. Tan, Y. Yeo, K. Watanabe, T. Taniguchi, and B. Özyilmaz, "Conductance oscillations induced by ballistic snake states in a graphene heterojunction," *Nature Communications*, vol. 6, p. 6093, 2015. 3.2.1

[71] H. Overweg, H. Eggimann, M. H. Liu, A. Varlet, M. Eich, P. Simonet, Y. Lee, K. Watanabe, T. Taniguchi, K. Richter, V. I. Fal'ko, K. Ensslin, and T. Ihn, "Oscillating Magnetoresistance in Graphene p-n Junctions at Intermediate Magnetic Fields," *Nano Letters*, vol. 17, pp. 2852–2857, 2017. 3.2.1

[72] E. B. Sonin, "Spin superfluidity, coherent spin precession, and magnon BEC," *Journal of Low Temperature Physics*, vol. 171, pp. 757–768, 2013. 4.1.1

[73] K. Nakata, J. Klinovaja, and D. Loss, "Magnonic quantum Hall effect and Wiedemann-Franz law," *Phys. Rev. B*, vol. 95, pp. 1–125429, 2017. 4.1.1

[74] A. V. Chumak, V. I. Vasyuchka, A. A. Serga, and B. Hillebrands, "Magnon spintronics," *Nature Physics*, vol. 11, no. June, pp. 453–461, 2015. 4.1.1, 4.1.1, 4.1.4

[75] F. Bloch, "Zur Theorie des Ferromagnetismus," *Z. Phys. 61, 206 (1930).*, vol. 61, pp. 206–219, 1930. 4.1.1

[76] C. Kittel, *Introduction to solid state physics.* Wiley, 8 ed., 2004. 4.1.1, 4.1

[77] J. Griffiths, "Anomalous High-frequency Resistance of Ferromagnetic Metals," *Nature*, vol. 158, pp. 670–671, 1946. 4.1.1

[78] C. Kittel, "On the theory of ferromagnetic resonance absorption," *Physical Review*, vol. 73, no. 2, pp. 155–161, 1948. 4.1.1, 4.1.2

[79] P. A. Fleury, S. P. S. Porto, L. E. Cheesman, and H. J. Guggenheim, "Light Scattering by Spin Waves in $\mathrm{FeF_2}$," *Physical Review Letters*, vol. 17, no. 2, pp. 84–87, 1966. 4.1.1

[80] S. O. Demokritov, B. Hillebrands, and A. N. Slavin, "Brillouin light scattering studies of confined spin waves: Linear and nonlinear confinement," *Physics Report*, vol. 348, pp. 441–489, 2001. 4.1.1

[81] J. Sinova, S. O. Valenzuela, J. Wunderlich, C. Back, and T. Jungwirth, "Spin Hall effects," *Reviews of Modern Physics*, vol. 87, pp. 1213–1259, 2015. 4.1.1

[82] Y. Kajiwara, K. Harii, S. Takahashi, J. Ohe, K. Uchida, M. Mizuguchi, H. Umezawa, H. Kawai, K. Ando, K. Takanashi, S. Maekawa, and E. Saitoh, "Transmission of electrical signals by spin-wave interconversion in a magnetic insulator.," *Nature*, vol. 464, no. 7286, pp. 262–266, 2010. 4.1.1, 4.1.4

[83] L. J. Cornelissen, J. Liu, R. A. Duine, J. B. Youssef, and B. J. V. Wees, "Long-distance transport of magnon spin information in a magnetic insulator at room temperature," *Nature Physics*, vol. 11, no. December, pp. 1022–1026, 2015. 4.1.1, 4.1.4

[84] D. Wesenberg, T. Liu, D. Balzar, M. Wu, and B. L. Zink, "Long-distance spin transport in a disordered magnetic insulator," *Nature Physics*, vol. 13, no. 10, pp. 987–993, 2017. 4.1.1, 4.1.4

[85] C. Kallin and B. I. Halperin, "Excitations from a filled Landau level in the two-dimensional electron gas," *Physical Review B*, vol. 30, no. 10, pp. 5655–5668, 1984. 4.1.2

[86] S. L. Sondhi, A. Karlhede, S. A. Kivelson, and E. H. Rezayi, "Skyrmions and the crossover from the integer to fractional quantum Hall effect at small Zeeman energies," *Physical Review B*, vol. 47, no. 24, pp. 16419–16426, 1993. 4.1.2, 4.2.1

[87] K. Schmeller, A., Eisenstein, J.P., Pfeiffer, L.N., West, "Evidence for skyrmions and single spin flips in the integer quantized Hall effect," *Physical Review Letters*, vol. 75, no. 23, pp. 4290–4293, 1995. 4.1.2, 4.2.1

[88] D. K. Maude, M. Potemski, J. C. Portal, M. Henini, L. Eaves, G. Hill, and M. A. Pate, "Spin excitations of a two-dimensional electron gas in the limit of vanishing landé g factor," *Physical Review Letters*, vol. 77, no. 22, pp. 4604–4607, 1996. 4.1.2

[89] E. H. Goldberg, B. B. Goldberg, and D. A. Broido, "Evidence of skyrmion excitations about $\nu = 1$ in n-modulation-doped single quantum wells by interband optical transmission," *Physical Review Letters*, vol. 76, no. 4, pp. 680–683, 1996. 4.1.2

[90] Y. Gallais, J. Yan, A. Pinczuk, L. N. Pfeiffer, and K. W. West, "Soft Spin Wave Near $\nu = 1:$ Evidence for a Magnetic Instability in Skyrmion Systems," *Physical Review Letters*, vol. 100, p. 086806, 2008. 4.1.2

[91] S. E. Barrett, G. Dabbagh, L. N. Pfeiffer, K. W. West, and R. Tycko, "Optically pumped NMR evidence for finite-size Skyrmions in GaAs quantum wells near Landau level filling ν=1," *Physical Review Letters*, vol. 74, no. 25, pp. 5112–5115, 1995. 4.1.2

[92] W. Desrat, D. Maude, M. Potemski, J. Portal, Z. R. Wasilewski, and G. Hill, "Resistively Detected Nuclear Magnetic Resonance in the Quantum Hall Regime: Possible Evidence for a Skyrme Crystal," *Physical Review Letters*, vol. 88, no. 25, pp. 1–4, 2002. 4.1.2

[93] G. Gervais, H. L. Stormer, D. C. Tsui, P. L. Kuhns, W. G. Moulton, A. P. Reyes, L. N. Pfeiffer, K. W. Baldwin, and K. W. West, "Evidence for skyrmion crystallization from NMR relaxation experiments," *Physical Review Letters*, vol. 94, p. 196803, 2005. 4.1.2

[94] M. Vuorio, "Condensate spin currents in helium-3," *Journal of Physics C: Solid State Physics*, vol. 7, pp. L5–L8, 1974. 4.1.3

[95] L. Corruccini and D. Osheroff, "Unusual Magnetic Relaxation in Superfluid 3He," *Physical Review Letters*, vol. 34, no. 10, pp. 564–567, 1975. 4.1.3

[96] A. S. Borovik-Romanov, Y. M. Bunkov, V. V. Dmitriev, and Y. M. Mukharskii, "Long-lived induction signal in superfluid 3He-B," *JETP Letters*, vol. 40, p. 1033, 1984. 4.1.3

[97] A. Oosawa, M. Ishii, and H. Tanaka, "Field-induced three-dimensional magnetic ordering in the spin-gap system," *J. Phys: Condens. Matter*, vol. 11, pp. 265–271, 1999. 4.1.3

[98] T. Nikuni, M. Oshikawa, A. Oosawa, and H. Tanaka, "Bose-Einstein condensation of dilute magnons in TlCuCl3," *Physical Review Letters*, vol. 84, pp. 5868–5871, 2000. 4.1.3

[99] C. Ruegg, N. Cavadini, A. Furrer, H. Gudel, K. Kramer, H. Mutka, A. Wildes, K. Habicht, and P. Voderwisch, "Bose-Einstein condensation of the triplet states in the magnetic insulator TlCuCl," *Nature*, vol. 423, pp. 62–65, 2003. 4.1.3

[100] S. O. Demokritov, V. E. Demidov, O. Dzyapko, G. A. Melkov, A. A. Serga, B. Hillebrands, and A. N. Slavin, "Bose-Einstein condensation of quasi-equilibrium magnons at room temperature under pumping," *Nature*, vol. 443, pp. 430–433, 2006. 4.1.3

[101] A. A. Serga, V. S. Tiberkevich, C. W. Sandweg, V. I. Vasyuchka, D. A. Bozhko, A. V. Chumak, T. Neumann, B. Obry, G. A. Melkov, A. N. Slavin, and B. Hillebrands, "Bose-Einstein condensation in an ultra-hot gas of pumped magnons," *Nature Communications*, vol. 5, pp. 1–8, 2014. 4.1.3

[102] E. B. Sonin, “Spin currents and spin superfluidity,” *Advances in Physics*, vol. 59, no. 3, pp. 181–255, 2010. 4.1.3

[103] B. Halperin and P. Hohenberg, “Hydrodynamic Theory of Spin Waves,” *Physical Review*, vol. 188, pp. 898–918, 1969. 4.1.3

[104] S. Takei and Y. Tserkovnyak, “Superfluid Spin Transport Through Easy-Plane Ferromagnetic Insulators,” *Phys. Rev. Lett.*, vol. 112, p. 227201, 2014. 4.1.3

[105] S. Takei, B. I. Halperin, A. Yacoby, and Y. Tserkovnyak, “Superfluid spin transport through antiferromagnetic insulators,” *Phys. Rev. B*, vol. 90, p. 094408, Sep 2014. 4.1.3

[106] J. König, M. C. Bønsager, and A. H. MacDonald, “Dissipationless Spin Transport in Thin Film Ferromagnets,” p. 4, 2000. 4.1.3

[107] R. Duine, A. Brataas, S. A. Bender, and Y. Tserkovnyak, “Spintronics and Magnon Bose-Einstein Condensation,” in *Universal Themes of Bose-Einstein Condensation* (N. Proukakis, D. Snoke, and P. Littlewood, eds.), pp. 505–524, Cambridge: Cambridge University Press, 2017. 4.1.3

[108] H. Chen and A. H. Macdonald, “Spin-superfluidity and spin-current mediated nonlocal transport,” *Universal Themes of Bose-Einstein Condensation*, pp. 525–548, 2017. 4.1.3

[109] S. Takei, A. Yacoby, B. I. Halperin, and Y. Tserkovnyak, “Spin Superfluidity in the ν=0 Quantum Hall State of Graphene,” *Physical Review Letters*, vol. 116, no. 21, p. 216801, 2016. 4.1.3, 4.2.3, 4.3

[110] D. S. Wei, T. V. D. Sar, J. D. Sanchez-yamagishi, K. Watanabe, T. Taniguchi, P. Jarillo-herrero, B. I. Halperin, and A. Yacoby, “Mach-Zehnder interferometry using spin- and valley-polarized quantum Hall edge states in graphene,” *Science Advances*, vol. 3, no. August, pp. 1–8, 2017. 4.1.4, B.6, B.7, B.8, B.11

[111] G. Giovannetti, P. A. Khomyakov, G. Brocks, V. M. Karpan, J. V. D. Brink, and P. J. Kelly, “Doping graphene with metal contacts,” *Physical Review Letters*, vol. 101, no. July, p. 026803, 2008. 4.2.1, B.2

[112] G. Nachtwei, “Breakdown of the quantum Hall effect,” *Physica E*, vol. 4, pp. 79–101, 1999. 4.2.1

[113] A. H. Macdonald and J. J. Palacios, “Magnons and skyrmions in fractional Hall ferromagnets,” *Physical Review B*, vol. 58, no. 16, pp. 171–174, 1998. 4.3

[114] L. Wang, I. Meric, P. Y. Huang, Q. Gao, Y. Gao, H. Tran, T. Taniguchi, K. Watanabe, L. M. Campos, D. a. Muller, J. Guo, P. Kim, J. Hone, K. L. Shepard, and C. R. Dean, "One-dimensional electrical contact to a two-dimensional material.," *Science*, vol. 342, pp. 614–7, 2013. A.1.1, B.1.1, C.1.3, C.2.3

[115] D. T. McClure, Y. Zhang, B. Rosenow, E. M. Levenson-Falk, C. M. Marcus, L. N. Pfeiffer, and K. W. West, "Edge-state velocity and coherence in a quantum Hall Fabry-Pérot interferometer," *Phys. Rev. Lett.*, vol. 103, p. 206806, Nov 2009. A.4

[116] S. Komiyama, H. Hirai, S. Sasa, and S. Hiyamizu, "Violation of the integral quantum Hall effect: Influence of backscattering and the role of voltage contacts," *Physical Review B*, vol. 40, no. 18, pp. 12566–12569, 1989. B.2

[117] D. Chklovskii, B. Shklovskii, and L. Glazman, "Electrostatics of edge channels," *Physical Review B*, vol. 46, no. 7, pp. 4026–4034, 1992. B.2

[118] E. Ahlswede, J. Weis, K. Van Klitzing, and K. Eberl, "Hall potential distribution in the quantum Hall regime in the vicinity of a potential probe contact," *Physica E: Low-Dimensional Systems and Nanostructures*, vol. 12, no. 1-4, pp. 165–168, 2002. B.2

[119] G. Li, A. Luican-Mayer, D. Abanin, L. Levitov, and E. Y. Andrei, "Evolution of Landau levels into edge states in graphene.," *Nature communications*, vol. 4, p. 1744, 2013. B.2

[120] G. Burkard, D. Loss, and D. P. DiVincenzo, "Coupled quantum dots as quantum gates," *Physical Review B*, vol. 59, no. 3, pp. 2070–2078, 1999. B.2

[121] D. A. Abanin, B. E. Feldman, A. Yacoby, and B. I. Halperin, "Fractional and integer quantum Hall effects in the zeroth Landau level in graphene," *Physical Review B*, vol. 88, no. 11, p. 115407, 2013. B.6

[122] F. Pientka, J. Waissman, P. Kim, and B. I. Halperin, "Thermal Transport Signatures of Broken-Symmetry Phases in Graphene," *Physical Review Letters*, vol. 119, p. 027601, 2017. B.6

[123] B. E. Feldman, A. J. Levin, B. Krauss, D. A. Abanin, B. I. Halperin, J. H. Smet, and A. Yacoby, "Fractional quantum hall phase transitions and four-flux states in graphene," *Physical Review Letters*, vol. 111, no. 7, p. 076802, 2013. B.6

[124] K. Watanabe, T. Taniguchi, and H. Kanda, "Direct-bandgap properties and evidence for ultraviolet lasing of hexagonal boron nitride single crystal," *Nature Materials*, vol. 3, pp. 404–409, 2004. C.1.1

[125] C. R. Dean, A. F. Young, I. Meric, C. Lee, L. Wang, S. Sorgenfrei, T. Watanabe, K. Taniguchi, P. Kim, K. L. Shepard, and J. Hone, "Boron nitride substrates for high-quality graphene electronics.," *Nature nanotechnology*, vol. 5, no. October, pp. 722–726, 2010. C.1.1

[126] J. H. Chen, C. Jang, S. Xiao, M. Ishigami, and M. S. Fuhrer, "Intrinsic and extrinsic performance limits of graphene devices on SiO_2," *Nature Nanotechnology*, vol. 3, pp. 206–209, 2008. C.1.1

[127] J. Martin, N. Akerman, G. Ulbricht, T. Lohmann, J. H. Smet, K. Von Klitzing, and A. Yacoby, "Observation of electron-hole puddles in graphene using a scanning single-electron transistor," *Nature Physics*, vol. 4, pp. 144–148, 2008. C.1.1

[128] K. I. Bolotin, K. J. Sikes, J. Hone, H. L. Stormer, and P. Kim, "Temperature-dependent transport in suspended graphene," *Physical Review Letters*, vol. 101, p. 096802, 2008. C.1.1

[129] X. Du, I. Skachko, A. Barker, and E. Y. Andrei, "Approaching ballistic transport in suspended graphene.," *Nature nanotechnology*, vol. 3, pp. 491–495, 2008. C.1.1

[130] K. S. Novoselov, A. Mishchenko, A. Carvalho, and A. H. Castro Neto, "2D materials and van der Waals heterostructures," *Science*, vol. 353, no. 6298, 2016. C.1.2

[131] P. J. Zomer, M. H. D. Guimares, J. C. Brant, N. Tombros, and B. J. Van Wees, "Fast pick up technique for high quality heterostructures of bilayer graphene and hexagonal boron nitride," *Applied Physics Letters*, vol. 105, no. 1, pp. 0–4, 2014. C.1.3

[132] S. J. Haigh, A. Gholinia, R. Jalil, S. Romani, L. Britnell, D. C. Elias, K. S. Novoselov, L. A. Ponomarenko, A. K. Geim, and R. Gorbachev, "Cross-sectional imaging of individual layers and buried interfaces of graphene-based heterostructures and superlattices," *Nature Materials*, vol. 11, pp. 764–767, 2012. C.1.3